# N-type substitutional doping of halide perovskite using metastable ions

Zuzanna Molenda

université de BORDEAUX

THÈSE PRÉSENTÉE

POUR OBTENIR LE GRADE DE

# DOCTEUR DE

# L'UNIVERSITÉ DE BORDEAUX

ÉCOLE DOCTORALE DES SCIENCES PHYSIQUES ET DE L'INGENIEUR

SPÉCIALITÉ : ELECTRONIQUE

Par Zuzanna MOLENDA

# N-type substitutional doping of halide perovskite using metastable ions

Sous la direction de : Dr. Lionel HIRSCH
(co-directeur : Dr. Dario BASSANI, co-encadrant : Dr. Sylvain CHAMBON)

Soutenue le : 16 décembre 2022

Membres du jury :

| | | |
|---|---|---|
| M. SALIBA, Michael | Professeur, University of Stuttgart | Rapporteur |
| Mme CHEN, Zhuoying | Chargée de recherche ESPCI Paris/Sorbonne Université/Université PSL | Rapporteure |
| M. KAHN, Antoine | Professeur, University of Princeton | Président du Jury |
| M. BOUCLé, Johann | Maître de conférences, Université de Limoges | Examinateur |
| M. HIRSCH, Lionel | Directeur de recherche CNRS/Université de Bordeaux | Directeur de thèse |
| M. BASSANI, Dario | Directeur de recherche CNRS/Université de Bordeaux | Co-directeur de thèse |
| M. CHAMBON, Sylvain | Chargé de recherche CNRS/Université de Bordeaux | Co-encadrant |

# Dopage par substitution de type N de pérovskite halogénée par l'utilisation d'ions métastables


## Résumé

Le caractère ionique du cristal de la pérovskite rend particulièrement difficile son dopage. Cette thèse présente une nouvelle approche de dopage, tant au niveau de la méthode, proposant le post-recuit, dopage en couches minces en deux étapes, qu'au niveau du concept, c'est-à-dire le dopage avec des ions 2+ et leur oxydation dans le réseau cristallin à 3+. A titre d'exemple, le samarium est choisi comme dopant de la pérovskite halogénée hybride d'iodure de plomb de méthylammonium (MAPI). Nous avons également montré que cette approche peut être appliquée à d'autres dopants ou pérovskites avec des résultats préliminaires sur l'iodure de plomb de formamidinium (FAPI) et la pérovskite à cation mixte $MA_{0.7}FA_{0.93}PbI_3$. L'étude XPS confirme l'oxydation de $Sm^{2+}$ à $Sm^{3+}$ à l'intérieur de la couche de pérovskite, ainsi que le profil en profondeur ToF-SIMS montre la pénétration du dopant dans toute la couche. La mesure de la sonde Kelvin et l'UPS démontrent le décalage du niveau de Fermi de la pérovskite dopée vers l'énergie de conduction, indiquant un dopage de type n. Ce dopage a permis d'augmenter la conductivité de MAPI de 3 ordres de grandeur.



Mots-clés : pérovskites halogénées, dopage, samarium, cellules solaires à pérovskite

# N-type substitutional doping of halide perovskite using metastable ions


## Abstract

The ionic character of the perovskite crystal renders it particularly challenging to dope. This work presents a novel n-type doping approach, both in terms of the method, proposing the post-annealing, two-steps thin film doping, and in terms of the concept, i.e. doping with 2+ ions and their oxidation in the crystal lattice to 3+. As an exemplary dopant, samarium is chosen and the doped perovskite is methylammonium lead iodide (MAPI), while one is convinced that this scheme can be applied to other dopants or perovskites, with the preliminary results on formamidinium lead iodide (FAPI) and mixed cation $MA_{0.7}FA_{0.93}PbI_3$ verifying the latter. The XPS study confirms the $Sm^{2+}$ to $Sm^{3+}$ oxidation inside the perovskite film and the ToF-SIMS depth profile shows the dopant penetration throughout the layer. The Kelvin probe measurement and the UPS demonstrate the n-type doped perovskite with the shift towards the CBM of the Fermi level, resulting in an increase up to 3 orders of magnitude of the conductivity.



Keywords: halide perovskites, doping, samarium, perovskite solar cells


La thèse a été préparée dans le Laboratoire de l'Intégration du Matériau au Système.

16 Avenue Pey Berland

33600 Pessac

# Acknowledgements

This endeavor would not have been possible without my three supervisors: Dr. Lionel Hirsch, Dr. Dario Bassani and Dr. Sylvain Chambon. Words cannot express my gratitude, however, I will try to use a few. Dr. Lionel Hirsch always managed to find the time for exciting discussions and I am extremely thankful for them. His thorough problem analysis helped me arrive to the point I am in today and his brilliant ideas greatly contributed to the current shape of this work. Dr. Dario Bassani's fearless attitude towards my ideas contributed greatly to the joy that accomplishing this project gave me and I would like to express my deepest gratitude for that. Also, his "chemistry point of view" has had a great impact on this work and on my way of thinking as a young scientist. Dr. Sylvain Chambon, especially at the beginning, helped me a lot with the adaptation to the new laboratory and always served with a practical help. I would also like to thank for the scientific passion atmosphere he brings to the group and to our meetings, together with original ideas.

I would like to express my deepest gratitude to my reviewers: Prof. Michael Saliba and Dr. Zhuoying Chen, as well as to the jury members: Dr. Antoine Kahn and Dr. Johann Bouclé. Thank you for having accepted to contribute in such a special way to my academic journey.

I'm extremely grateful to the Funders of my research: Agence National de Recherche, Region d'Aquitaine and University of Bordeaux.

Special thanks to Dr. Thierry Toupance for making the X-ray difractogram available for my measurements. Big thanks to Christine Labrugère for performing and analyzing the XPS spectra. Her experience and insightful comments are much appreciated. Many thanks to Dr. Roland Lefèvre for performing the UPS spectra and to Philippe Legros for the SEM images. I am also thankful to Dr. Nith Cam for performing the ToF SIMS spectra and to Dr. Jean-Paul Salvetat for the help in their analysis.

I would like to extend my sincere thanks to Prof. Costas Stoumpos, who hosted me in his laboratory at the University of Crete for 3 weeks. His amazing hospitability and passion for science will not be forgotten. I am grateful for having learnt so much about the chemistry of perovskites and I hope our collaboration will continue in the future.

I'd like to acknowledge the work of Dr. Yan-Fang Chen, whose PhD thesis results were a starting point to my work.

Thanks should also go to Dr. Julie Euvrard for her precious advice on the Hall measurement technique. I'd like to recognize the collaboration with Dr. Raphael Clerc and Dr. Bastien Politi in the analysis of the capacitance measurements. I am also grateful to Dr. Mamatimin Abbas for having worked with him on the UPS analysis and to Dr. Cédric Ayela and Dr. Damien Thau for their guidance in utilizing the 3D printer. I had also a pleasure to work with Prof. Guillaume Wantz, Dr. Laurence Vignau, Dr. Marie Gueunier-Farret, Dr. Isabelle Dufour, Martial Leyney, Dr. Gilles Roche, Cindy Mauriac, Dr. Jérémy Barbé, Dr. Rafael Sanchez, Dr. Bruno Flament, Dr. Chloé Dindault, Nhung Pham, Francis Feaugas, Hugo Laval, Dr. Simon Sandrez, Dr. Alexandre Bachelet, Reem El-Attar, Natalia Menezes, Quan Sun, Dr. Abdulezis Ablat, Jonghyun Choi and Dr. Marco Pereira.

Lastly, I'd like to mention my family and friends. Their daily support is indispensable and I wouldn't have reached this point without them.

# Table of Contents

1. Introduction ..... 1

1.1 Brief history of perovskites ..... 1

1.2 Perovskite solar cells (PSC) ..... 2

2. Perovskite doping ..... 8

2.1 Surface doping ..... 10

2.2 Doping at grain boundaries ..... 11

2.3 Doping by substitution ..... 15

3. Optimization of the solar cells fabrication parameters ..... 25

3.1 Solar cell architecture and reproducibility ..... 25

3.2 Ambient temperature impact on the PSC performance ..... 35

4. Thin film doping with Cd, Pd, Ru, Sm and Sn ..... 48

4.1 One step doping ..... 50

4.2 Two-step doping ..... 53

4.3 Investigation of the doping mechanism ..... 61

4.3.1 Valence of samarium ions and their incorporation in the perovskite film ..... 61

4.3.2 Surface morphology ..... 69

4.3.3 Structural properties ..... 70

4.3.4 Optical properties ..... 72

4.3.5 Semiconductor type ..... 73

4.3.6 Mott-Schottky analysis ..... 81

4.3.7 Hall effect ..... 85

5. Conclusions and perspectives ..... 91

6. Methods ..... 96
6.1 Fabrication ..... 96
6.1.1 Perovskite solar cells ..... 96
6.2 Microscopy ..... 96
6.2.1 Atomic force microscopy (AFM) ..... 99
6.2.2 Scanning electron microscopy (SEM) ..... 99
6.3 Crystal structure – X-ray diffraction (XRD) ..... 100
6.4 Spectroscopy ..... 101
6.4.1 UV-Vis absorption spectroscopy ..... 101
6.4.2 Photoluminescence (PL) ..... 103
6.4.3 Time of flight secondary ion mass spectroscopy (ToF-SIMS) ..... 105
6.4.4 X-ray photoemission spectroscopy (XPS) ..... 105
6.4.5 Ultraviolet photoemission spectroscopy (UPS) ..... 106
6.5 Electronic characterization ..... 106
6.5.1 Solar cell current-voltage characterization ..... 106
6.5.2 External quantum efficiency (EQE) ..... 108
6.5.3 Electroluminescence (EL) ..... 108
6.5.4 Conductivity ..... 109
6.5.5 Kelvin probe (KP) ..... 110
6.5.6 Mott-Schottky ..... 111
6.5.7 Hall effect ..... 112

# 1. Introduction

## 1.1 Brief history of perovskites

In 1829, a group of German naturalists took part in a scientific expedition to the Altai and Ural Mountains and the Caspian Sea region in Imperial Russia. Among many samples that August Alexander Kämmerer sent back to Germany from the Ural Mountains, there was a black mineral that was identified as $CaTiO_3$. Gustav Rose, another participant of the expedition, examined and described its extraordinary crystal structure, and later wrote an article about his discovery[1]. On Kämmerer's suggestion, he named the mineral after the Russian mineralogist and nobleman who at the time served as a Minister of Internal Affairs, Lev Aleksevich Perovski. The sample still exists today and it can be admired in the Museum für Naturkunde in Berlin. Along with the discoveries of other minerals sharing the same crystal structure and first successful attempts of their synthesis in the 19th century[2], the term *perovskite* started being used to describe the crystal structure characterized by the stoichiometry $ABX_3$[3] (Figure 1.1).

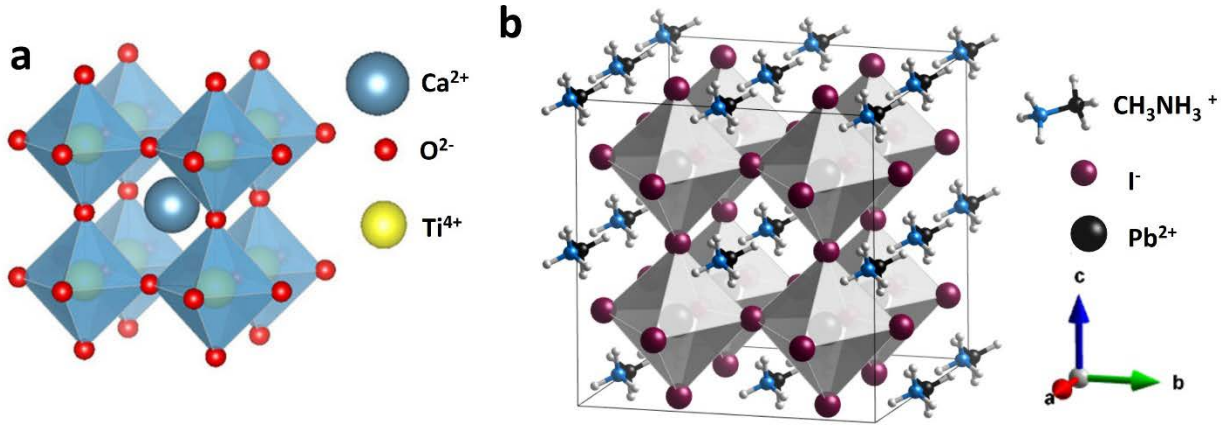


*Figure 1.1. Crystal structure of $CaTiO_3$ [4] (a) and $CH_3NH_3PbI_3$ [5] (b).*

In recent years, we have observed an increasing number of publications on halide perovskites, where A = $CH_3NH_3^+$ (methylammonium or MA), $NH_2CHNH_2^+$ (formamidinium or FA) or $Cs^+$, B = $Pb^{2+}$ or $Sn^{2+}$ and X = $Cl^-$, $I^-$ or $Br^-$ [6–8]. This interest stems from these perovskites' narrow and tunable band gap[9], high charge carrier mobility[10], wide range of light absorption[11] and long carrier recombination lifetime[12]. All these remarkable properties allow them to find application in a number of optoelectronic devices, such as solar cells[13], LEDs[14], lasers[15] and photodetectors.[16]. Most of the recent knowledge on halide perovskites was found very recently, over little more than a decade, which lets us believe there is still a lot to discover about this unique class of material.

## 1.2 Perovskite Solar Cells (PSC)

The first report of a perovskite-based solar cell was published by Kojima et al. in 2009[17]. The work was inspired by research in dye sensitized solar cells (DSSC) and used the perovskite as a "dye" and absorber, blended into the porous $TiO_2$ layer. The measurements were performed using a liquid electrolyte with a platinum counter electrode and achieved 3.81% and 3.13% photo conversion efficiency (*PCE*) for $CH_3NH_3PbI_3$ and $CH_3NH_3PbBr_3$, respectively. This research was the starting point in a field that immediately flourished and the latest record efficiency of 25.7% for a single junction perovskite solar cell was achieved in 2021 by H. Min with a $MAPbI_3$ and $FASnCl_3$ double layer polycrystalline film[18]. Figure 1.2 shows the increase of the *PSC* record efficiency with respect to other technologies. Such a fast development of the PSC technology owes partially to the already existing knowledge in the field of DSSC and organic photovoltaics (OPV). Indeed, the most common method of fabricating perovskite thin films is spin coating and many of the charge transporting materials used for perovskite solar cells are used in OPV or DSSC. Also, the device architecture is OPV- or DSSC-inspired and, naturally, understanding of the charge transport mechanism was much facilitated due to the pre-existing knowledge in these fields.

Apart from spin coating, extensively described in Chapter 2 as it is used in this work, perovskite thin films can be also achieved by dip-coating[19], drop casting[20], doctor blade[21,22] and evaporation[23]. Dip coating is done by immersing the nanoporous $TiO_2$ into a $PbI_2$ solution and subsequently immersing the layer in a $CH_3NH_3I$ solution, forming a layer of $CH_3NH_3PbI_3$. Drop casting consists of depositing a solution of perovskite precursors onto the substrate and evaporating the solvent. With the doctor blade method, the solution is evened out onto a substrate using a blade, ensuring the homogenous thickness of the layer. Perovskite evaporation consists of a sequential or simultaneous thermal evaporation of the perovskite precursors onto the substrate, where the precursors then react to form the perovskite layer.

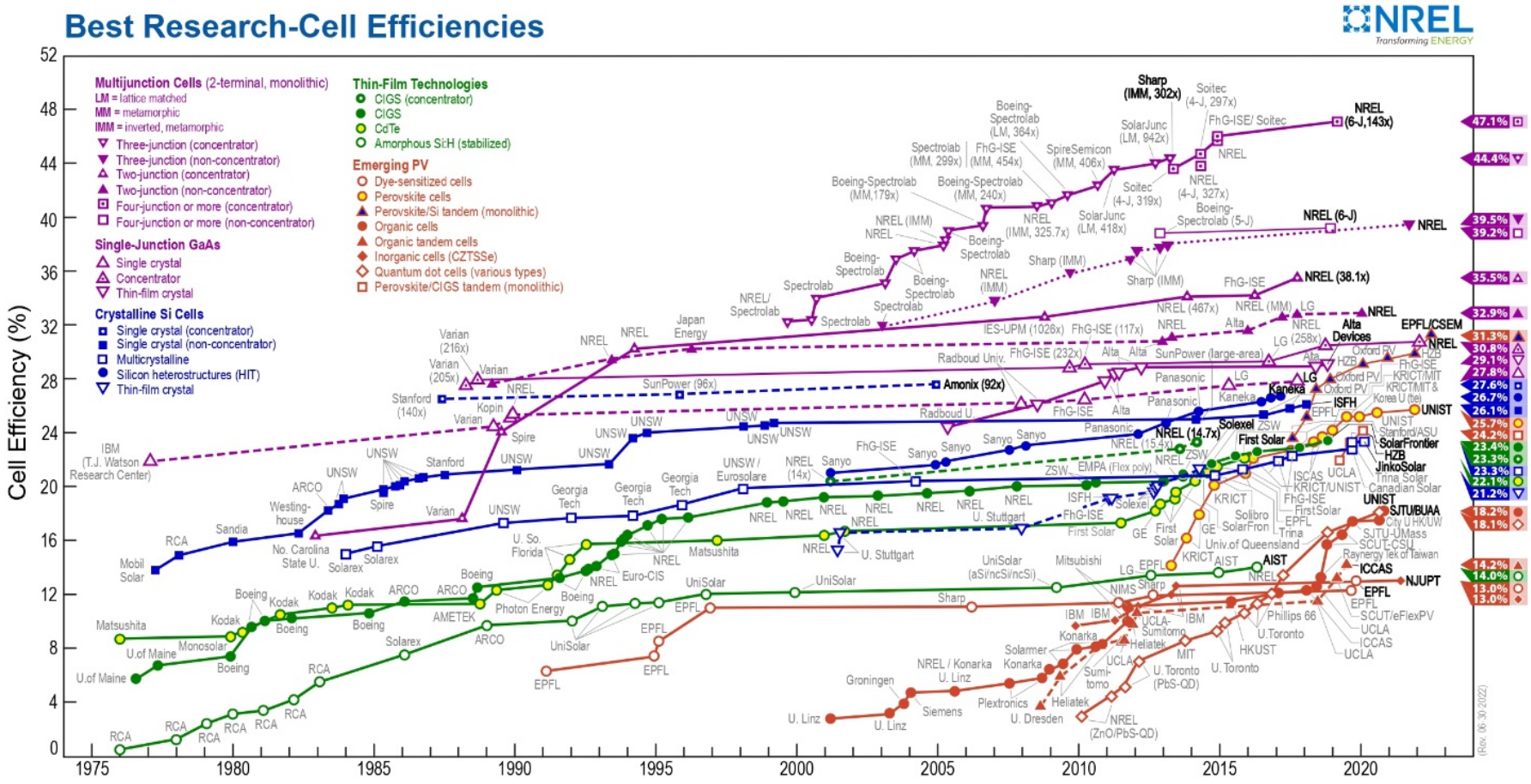


*Figure 1.2. Best solar cell efficiencies*[24].

The first step in light-to-electric power conversion is light absorption. Then, the internal electric field separates electrons and holes, which migrate to opposite electrodes. That causes a splitting of the electron and hole quasi-Fermi levels. The difference between these levels determines the open circuit voltage ($V_{oc}$) and defines the available free energy after the charges have been separated. For the efficient charge extraction, charge selective transport materials should be in contact with both sides of the light absorbing film. Their specific energy levels, valence band maximum (VBM) for hole transporting layer (HTL) and conduction band minimum (CBM) for the electron transporting layer (ETL), must lie close to the respective VBM and CBM of the active layer. They play an important role also for the short circuit current ($J_{sc}$), as non-optimal charge collection will reduce it. Another important issue is the interface between the charge selective layers and the perovskite. These should be engineered as to avoid interfacial charge recombination and subsequent decrease of the fill factor (*FF*). The power conversion efficiency (*PCE*) is defined as the product of the open circuit voltage, short circuit current density and fill factor, generated at the sunlight irradiance (AM 1.5G) of $P_{sun}$ = 100 W/cm$^2$, as described by Equation 1.1.

$$PCE = \frac{V_{oc} \cdot J_{sc} \cdot FF}{P_{sun}} \tag{1.1}$$

Perovskite-based solar cells are fabricated by stacking the perovskite layer between the charge transporting layers, connected respectively to the metal electrode on one side and a transparent electrode on the other. The transparent electrode is typically made of tin-doped indium oxide (ITO) or fluorine-doped tin oxide (FTO). In the literature, one can find 3 different perovskite solar cells architectures, depending on which contact these layers are connected to (Figure 1.3):

- mesoporous, deriving from the pioneer work of Kojima[17], in which the perovskite is blended into meso or nanoporous $TiO_2$, working as the electron transporting layer (ETL).
- planar, where the perovskite has a planar connection with the ETL,
- planar inverted, where the hole transporting layer (HTL) is deposited onto the bottom electrode and the ETL below the top electrode.

Charge transporting materials are selected based on their VBM and CBM levels. Ideally, the HTL should have its ionization energy between the ionization energy of the perovskite and the work function (*WF*) of the electrode, while its electron affinity should be high enough to prevent (or block) the electrons from being transported in this direction. On the contrary, the electron affinity of the ETL should lay between the perovskite's and electrode's electron affinities with the ionization energy low enough to block the

holes and prevent charge recombination. Figure 1.4 presents the energy levels of the most commonly used perovskites and charge transporting materials in the PSC-covered literature.

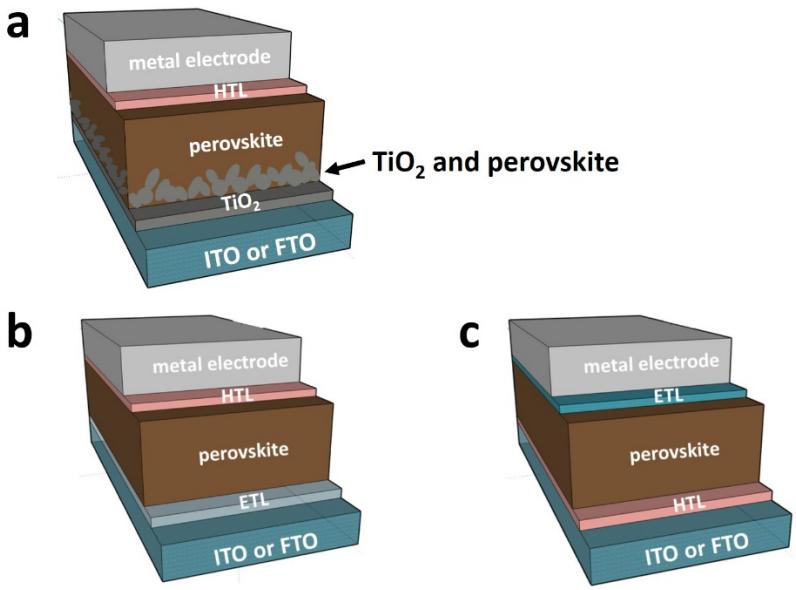


*Figure 1.3. Three different architectures of perovskite solar cells: a) mesoporous, b) planar, c) planar inverted.*

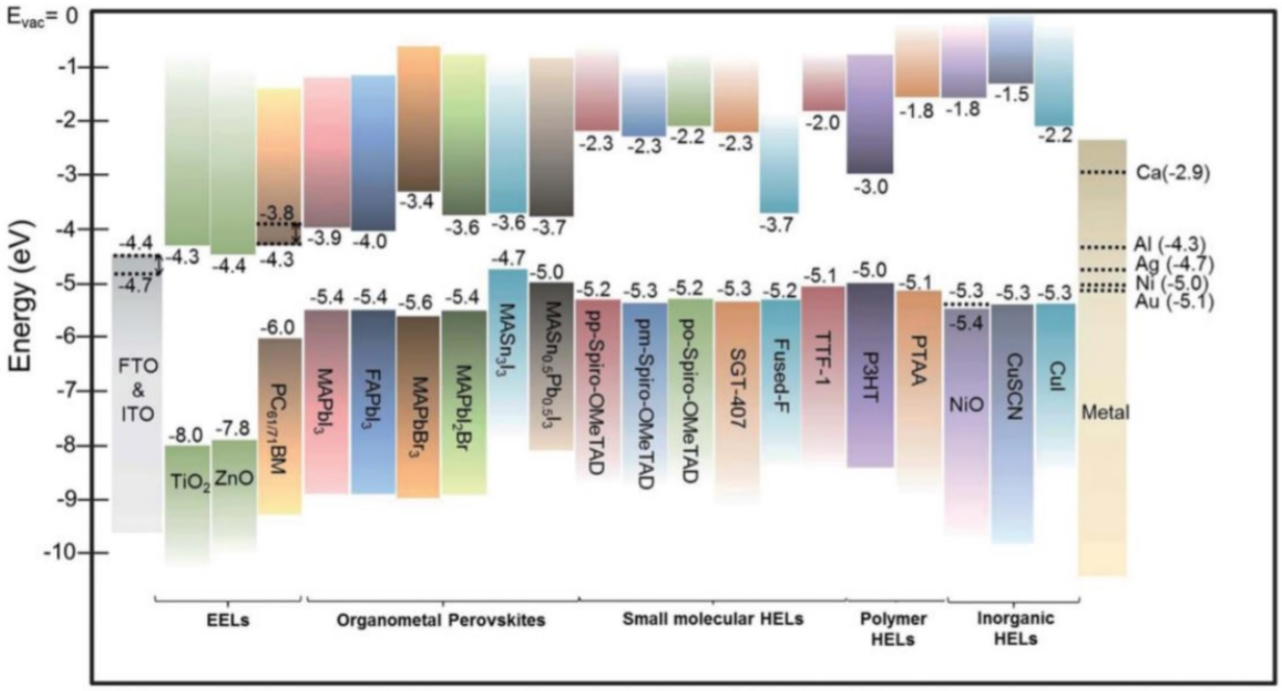


*Figure 1.4. VBM and CBM of some perovskites and the most popular ETLs and HTLs*[25].

## Conclusions

In this chapter, the short story of the perovskite discovery was presented, which, after a century, is now experiencing immense popularity due to their versatility in semiconductor applications. As this work focuses on solar cells, the perovskite solar cell principle of operation was discussed, together with different device architectures and different materials that allow their realization.

## References


[1] G. Rose, *Ann. Phys.* **1839**, *124*, 551.

[2] H. L. Wells, *Am. J. Sci.* **1893**, *45*, 121.

[3] M. A. Peña, J. L. G. Fierro, *Chem. Rev.* **2001**, *101*, 1981.

[4] T. Yamanaka, N. Hirai, Y. Komatsu, *Am. Mineral.* **2002**, *87*, 1183.

[5] Y. Dang, Y. Liu, Y. Sun, D. Yuan, X. Liu, W. Lu, G. Liu, H. Xia, X. Tao, *CrystEngComm* **2015**, *17*, 665.

[6] I. Gelmetti, L. Cabau, N. F. Montcada, E. Palomares, *ACS Appl. Mater. Interfaces* **2017**, *9*, 21599.

[7] J. Zhang, J. Su, Z. Lin, M. Liu, J. Chang, Y. Hao, *Appl. Phys. Lett.* **2019**, *114*, 1.

[8] Y. L. Tong, Y. W. Zhang, K. Ma, R. Cheng, F. Wang, S. Chen, *ACS Appl. Mater. Interfaces* **2018**, *10*, 31603.

[9] B. Yang, F. Zhang, J. Chen, S. Yang, X. Xia, T. Pullerits, W. Deng, K. Han, *Adv. Mater.* **2017**, *29*, 1.

[10] D. Shi, V. Adinolfi, R. Comin, M. Yuan, E. Alarousu, A. Buin, Y. Chen, S. Hoogland, A. Rothenberger, K. Katsiev, Y. Losovyj, X. Zhang, P. A. Dowben, O. F. Mohammed, E. H. Sargent, O. M. Bakr, *Science (80-. ).* **2015**, *347*, 519.

[11] Q. Shen, Y. Ogomi, J. Chang, T. Toyoda, K. Fujiwara, K. Yoshino, K. Sato, K. Yamazaki, M. Akimoto, Y. Kuga, K. Katayama, S. Hayase, *J. Mater. Chem. A* **2015**, *3*, 9308.

[12] M. B. Johnston, L. M. Herz, *Acc. Chem. Res.* **2016**, *49*, 146.

[13] N. G. Park, *Mater. Today* **2015**, *18*, 65.

[14] X. Zhang, W. Wang, B. Xu, S. Liu, H. Dai, D. Bian, S. Chen, K. Wang, X. W. Sun, *Nano Energy* **2017**, *37*, 40.

[15] S. Chen, K. Roh, J. Lee, W. K. Chong, Y. Lu, N. Mathews, T. C. Sum, A. Nurmikko, *ACS Nano* **2016**, *10*, 3959.

[16] S. F. Leung, K. T. Ho, P. K. Kung, V. K. S. Hsiao, H. N. Alshareef, Z. L. Wang, J. H. He, *Adv. Mater.* **2018**, *30*, 1.

[17] M. T, K. A, T. K, S. Y, *J. Am. Chem. Soc.* **2009**, *131*, 6050.

[18] H. Min, D. Y. Lee, J. Kim, G. Kim, K. S. Lee, J. Kim, M. J. Paik, Y. K. Kim, K. S. Kim, M. G. Kim, T. J. Shin, S. Il Seok, *Nature* **2021**, *598*, 444.

[19] J. Burschka, N. Pellet, S. J. Moon, R. Humphry-Baker, P. Gao, M. K. Nazeeruddin, M. Grätzel, *Nature* **2013**, *499*, 316.

[20] J. H. Im, I. H. Jang, N. Pellet, M. Grätzel, N. G. Park, *Nat. Nanotechnol.* **2014**, *9*, 927.

[21] Y. Deng, Q. Wang, Y. Yuan, J. Huang, *Mater. Horizons* **2015**, *2*, 578.

[22] H. Ying, Y. Liu, Y. Dou, J. Zhang, Z. Wu, Q. Zhang, Y. B. Cheng, J. Zhong, *Front. Optoelectron.* **2020**, *13*, 272.

[23] M. Liu, M. B. Johnston, H. J. Snaith, *Nature* **2013**, *501*, 395.

[24] NREL, "Best Research-Cell Efficiency Chart," can be found under https://www.nrel.gov/pv/cell-efficiency.html, **n.d.**

[25] N. K. Elumalai, M. A. Mahmud, D. Wang, A. Uddin, *Energies* **2016**, *9*, DOI 10.3390/en9110861.

# 2. Perovskite doping

Hybrid organic–inorganic perovskite (HOIP) solar cells combine the advantages of solution-phase processing technologies with high power conversion efficiency (PCE) that are in constant improvement. This class of materials has benefited from pre-existing knowledge gained from both inorganic semiconductors (band structure, photon absorption, charge transport…) and organic semiconductors (wet process, low-temperature processes, flexible substrates, etc.). Nevertheless, the spread of PCEs reported in the literature remains very large, suggesting that material properties and interfaces are very dependent on the quality of the fabrication process, including environmental factors[1]. As pointed out in the reviews by Brenner *et al*.[2] and by Fakharuddin *et al*.[3], a consensus has emerged in the literature on the critical role of surfaces / interfaces in the operation of perovskite-based devices and their stability. Interfaces and contacts are therefore key points to achieve reliable and efficient solar cells. This is generally true for all types of solar cells. However, in most inorganic solar cells (and in silicon solar cells in particular), this difficulty is partially solved by using well-controlled doping layers. Indeed, doping allows contacting metal electrodes with highly doped semiconductor layers, making the cell performance insensitive to the value of the metal's work function, giving more flexibility in selecting metals. From a more fundamental point of view, it is a challenge to control the doping of metal halide perovskites due to their "defect tolerance" and ionic character of the crystal. Therefore, perovskite doping has been so far achieved by molecular charge transfer or through defect formation to provide extra electrons or holes to the lattice[4].

Perovskite doping would open new possibilities for electronic applications. Yet, only few reports of such doping can be found in the literature to date. In what follows, the doping is considered quite broadly, i.e. not only substitution and interstitial doping, but also doping on the surface and at grain boundaries. The latest attempts in doping halide perovskites will be presented with a special emphasis on its impact on the electronic properties, such as conductivity, charge carrier mobility, charge carrier density and carriers' type. Although the results are very promising, the proposed explanation of the doping mechanism and influence are still a subject of debate. Although essential for the reasonable design of material adapted to their applications, the complete understanding of the doping mechanism remains a challenge.

To date, devices based on halide perovskites are made with unintentionally doped perovskite whereas for traditional semiconductors and crystalline solids, the influence of doping has been studied extensively and can either induce electronic positive (p) or negative (n) type doping. To date, the only example of a p-n homojunction perovskite solar cell was reported in 2019[5]. In that work, excess $PbI_2$ was

used on one side of the MAPI layer and excess MAI on the other for the *n* and *p* doping, respectively. A significant increase of the photovoltaic efficiency by using a p-n homojunction rather than intrinsic perovskite was demonstrated. However, a comment published by Thomas Kirchartz and David Cahen[6], ruled out that the observed enhancement was due to the *p* and *n* doping because their doping level is basically too low to induce such enhancement. Nevertheless, this debate is a demonstration of both the interest and the difficulty in controlling doping of perovskite semiconductors.

Nanocrystal doping seems to be technically less complicated due to high surface-to-volume ratio. For this reason, much more has been achieved in doping of the perovskite nano structures rather than bulk[7–13]. However, a great part of the knowledge gained from investigating nanomaterials can be useful in designing bulk doped perovskite in the future. Therefore, in this chapter both nano crystals and films doping will be reviewed.

The increased interest in perovskites in recent years resulted in the publication of a significant number of excellent reviews. For instance, Li *et al*.[14] summarized the chemical and structural variability of hybrid organic-inorganic halide perovskites, paying special attention to their optoelectronic and magnetic properties. Mitzi and Saparov[15] discussed the versatility of the perovskite composition in the bulk material as well as in case of 2D structure. Zhang *et al*.[16] provided an excellent systematic review of doping each side of the perovskite, demonstrating the structural dependence on its electronic and optoelectronic properties. Most of these reviews focused on the crystallographic aspect of the doping and, following that, changes within the bandgap. In this case, reviewing the conductivity influence upon doping of the perovskite is a natural consequence. To that extend, Euvrard *et al*.[4] presents a comprehensive study proposing the requirements for the electrical doping of halide perovskites. The methods of doping characterization are explained, with special attention to their applicability and understanding.

The carrier resolved photo-Hall (CRPH) technique[17] is particularly interesting for the elucidation of the minority carrier properties that are impossible to obtain using the standard Hall effect method. Briefly, the technique is based on the measurement of the Hall coefficient *H* and conductivity $\sigma$ upon light illumination that changes its generation rate *G* (which corresponds to the light intensity) by up to eight orders of magnitude. These three quantities are linked by the following equations:

$$\sigma = e(\mu_p p + \mu_n n) \tag{2.1}$$

$$H = \frac{r(p-\beta^2 n)}{e(p+\beta n)^2} \tag{2.2}$$

$$\Delta\mu_H = \frac{d(\sigma^2 H)}{d\sigma} = \left(2 + \frac{dlnH}{dln\sigma}\right) H\sigma \quad (2.3)$$

$$\Delta\mu = \mu_p - \mu_n = \Delta\mu_H / r \quad (2.4)$$

Where *e* is the elementary charge, $\mu_p$ and $\mu_n$ are the hole and electron (drift) mobilities, *p* and *n* are the hole and electron densities, $\beta = \mu_n/\mu_p$ is the mobility ratio, and *r* is the Hall scattering factor, which is commonly considered as equal to unity[18]. CRPH measurements allow the determination of the semiconductor type and ambipolar diffusion length, as well as the investigation of the minority and majority carrier properties, such as charge carrier density, mobility and lifetime.

## 2.1. Surface doping

Surface doping of the perovskite is used to reduce the contact resistance and improve the efficiency of charge collection at the electrodes in perovskite solar cells. Surface modifications commonly include treating with Lewis bases (pyridine, thiophene) or alkylammonium halides (methylammonium chloride, choline chloride)[19–22]. Recently, Sadhu *et al.*[23] used surface interactions between fluorocarbons and hybrid organic inorganic perovskites to tune the surface potential of perovskites. Even though it cannot be considered to be doping, the use of various fluorinated porphyrins allowed a fine tuning of over 150 mV of the surface potential, measured by Kelvin probe, to be achieved.

Noel *et al.*[24] synthesized via spin-coating the double-cation double-halide $FA_{0.85}MA_{0.15}Pb(I_{0.85}Br_{0.15})_3$ perovskite and subsequently treated the layers with molybdenum tris(1-(trifluoroacetyl)-2-(trifluoromethyl)ethane-1,2-dithiolene) [$Mo(tfd\text{-}COCF_3)_3$], diluted in chlorobenzene, which can be a dopant of 2,2',7,7'-tetrakis[*N*,*N*-di(4-methoxyphenyl)amino]-9,9'-spirobifluorene (Spiro-OMeTAD), in substitution of the hygroscopic lithium bis((trifluoro-methyl)sulfonyl) imide (Li-TFSI)[25]. The Kelvin probe measurements under $N_2$ (Figure 2.1a) showed that the absolute value of the work function increases along with increasing concentration of the dopant, which is a result of additional positive charges being introduced in the perovskite surface with increasing dopant concentration. According to the authors, it suggests a direct interaction between perovskite and dopant molecules. The dark microwave conductivity measurement (Figure 2.1b) shows a modest change of conductivity, which implies that the dopant molecules remain on the perovskite surface, making it more p-type. Relative conductivity (normalized to that of the control sample) increases by a factor 2.2 with doping concentration up to 0.1%, which is associated with the increase of mobile charge carrier density in the films. According to the authors, the decrease of the relative conductivity for the highest concentration may occur due to the

formation of dopant clusters on the surface. These act as trapping sites and thus increase recombination. It is also pointed out that the perovskite becomes too strongly p-type, causing the reduction of the carrier lifetime and subsequently their diffusion lengths[26].

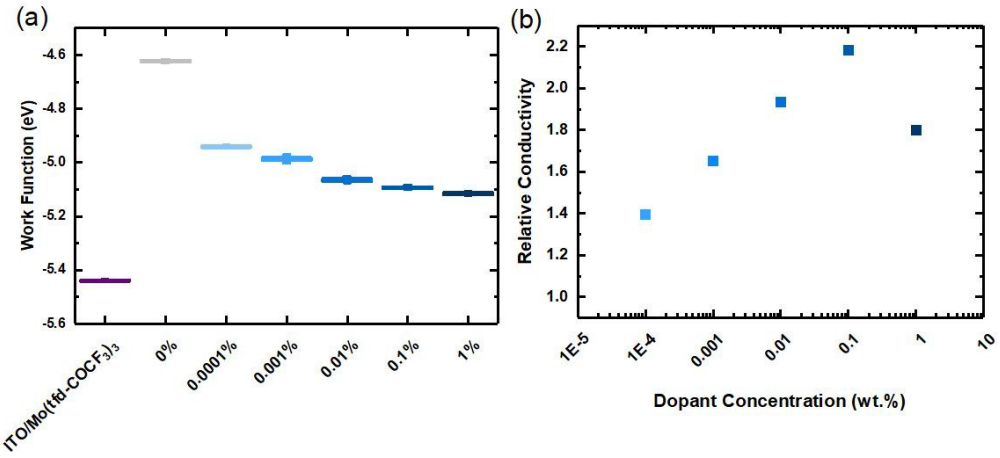


*Figure 2.1. Kelvin probe and microwave conductivity measurements. (a) Work functions of Mo(tfd-COCF3)$_3$ dopant, $FA_{0.85}MA_{0.15}Pb(I_{0.85}Br_{0.15})_3$ perovskite, and perovskite films doped by Mo(tfd-COCF3)$_3$, with different concentrations, measured by Kelvin probe. (b) Dark conductivities of undoped perovskite films and doped with various concentrations of Mo(tfd-$COCF_3)_3$, obtained by microwave conductivity measurements. Reprinted with permission from Noel et al., Energy Environ. Sci., 2019, 12, 3063-3073*[24]

Surface treatment on polycrystalline films is mostly limited to grain boundary treatments, as growing crystals "push" the impurities and defects to the grain boundaries. This natural phenomenon was used to control the doping as shown in the next section.

## 2.2 Doping at grain boundaries

Euvrard *et al.*[27] propose the passivation of grain boundaries of $MAPbI_3$ using $PbI_2$. The $PbI_2$ phase is on the grain boundaries throughout the layer, therefore it can be considered that this modification impacts the whole of the material. The 5% excess $PbI_2$ added to the perovskite solution precipitated on the grain boundaries after annealing (Figure 2.2). The light-colored phase was confirmed to be $PbI_2$ by X-ray diffraction (XRD) and energy dispersive X-ray spectroscopy (EDX) measurements. This effect was observed repeatedly by different groups[28–30]. The minority and majority carrier properties of the layers under the influence of the extra $PbI_2$ phase were analyzed using carrier resolved photo-Hall measurements[31]. The majority carrier type was concluded to be *n* for both doped and undoped MAPI from the negative slope of the *ln(H)* versus *ln(σ)* plot. Electron mobility $\mu_e$ with and without $PbI_2$ in excess was found to be 20 ± 4 $cm^2V^{-1}s^{-1}$ and 21 ± 9 $cm^2V^{-1}s^{-1}$, respectively, while hole mobility $\mu_h$ were found to

be 12 ± 4 $cm^2V^{-1}s^{-1}$ and 14 ± 5 $cm^2V^{-1}s^{-1}$, respectively. The authors suggest that no significant change of carrier mobility between the perovskite with and without $PbI_2$ means that the presence of extra $PbI_2$ phase did not impact shallow traps at the grain boundaries or in the bulk. It clearly shows that an excess of 5% $PbI_2$ induces an increase of one order of magnitude of the charge carrier density. The Fermi level shift was determined to be of 90 meV, from 430 meV below the conduction band for undoped $MAPbI_3$ to 340 meV below the conduction band with the addition of $PbI_2$.

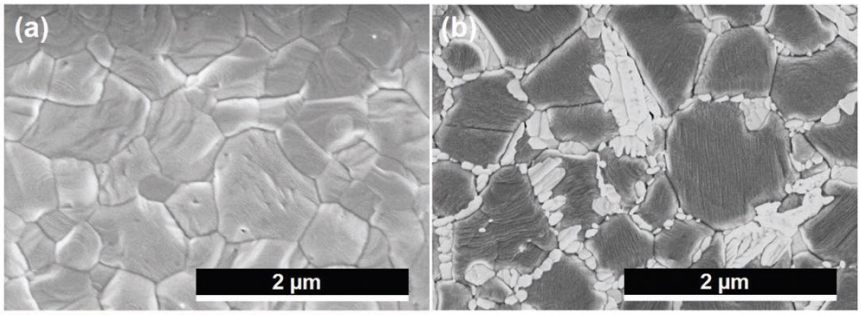


*Figure 2.2. SEM images of undoped (a) and $PbI_2$-modified (b) $MAPbI_3$. Reprinted with permission from J. Euvrard et al., Adv. Energy Mater. 2019, 1902706*[27].

Gaulding *et al*.[7] investigated the $CsPbI_3$ perovskite doping with organic molecules as a method to passivate the nanocrystals in the solid film. They incorporated the compounds commonly used to dope organic semiconductors: electron-accepting component, 2,3,5,6-tetrafluoro-7,7,8,8-tetracyanoquinodimethane (F4TCNQ) for p-type doping, or electron-donating benzyl viologen (BV) for n-type doping. The conductivity measured for both n or p type doping was obtained using flash-photolysis time-resolved microwave conductivity (fp-TRMC), as presented in Figure 2.3. This technique is based on exciting the charge carriers using a 4 ns light pulse. The photoconductance of these carriers ($\Delta G$), determined by the yield mobility product ($\Delta G = \varphi\Sigma\mu = \varphi(\mu_n + \mu_p)$), where $\varphi$ is the quantum yield of the photo carrier generation and $\mu_n$ and $\mu_p$ are electron and hole mobilities, respectively) is then measured by the microwave probe as a function of time[32]. Even though the decay time is shorter for both the n- and p-type doped materials compared to the undoped material, for p-doping the signal is significantly enhanced, both in early and in late times while for n-doping a decrease of the yield-mobility product is observed. The authors suggest that this long-lasting high hole mobility in the F4TCNQ-doped perovskite can be useful in application for phototransistors and photodetectors.

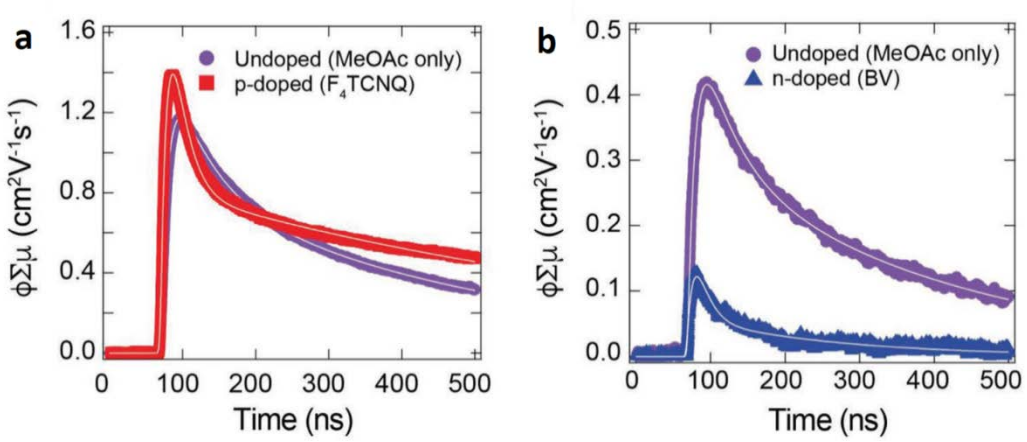


*Figure 2.3. a) fp-TRMC for undoped $CsPbI_3$ nanocrystals as well as doped with a) 0.125 mg $mL^{-1}$ $F_4TCNQ$ and b) 0.35 mg $mL^{-1}$ BV. The observed changes are reproducible even though the mobility yield can vary from one sample to another. Reprinted with permission from Gaulding et al. Adv. Mater. 2019, 31, 1902250*[7].

To determine conductivity as a function of the doping concentration, field-effect transistors (FET) devices were fabricated and the slope of the I-V curve was determined from four-point probe measurements (Figure 2.4a). For the F4TCNQ-doped perovskite, the relative (comparing to undoped) increase of the conductivity was up to 250%, while for the BV-doped $CsPbI_3$ only a decrease of the conductivity was observed. The authors highlight that such a behavior implies that the improved hole conductivity of the F4TCNQ-doped perovskite nanocrystals is most probably solely a result of the p-type doping, and it is not an effect of changes of band bending at the contacts. The extracted FET hole mobilities for different concentrations are presented in Figure 2.4b. The highest hole mobility was $5.9 \times 10^{-5}$ $cm^2$ $V^{-1}s^{-1}$ at a dopant concentration of 125 mg $mL^{-1}$. To compare, the hole mobility of the undoped material was $1.7 \times 10^{-5}$ $cm^2$ $V^{-1}$ $s^{-1}$. In contrast, for the BV doping, the n-type conduction channel was never observed.

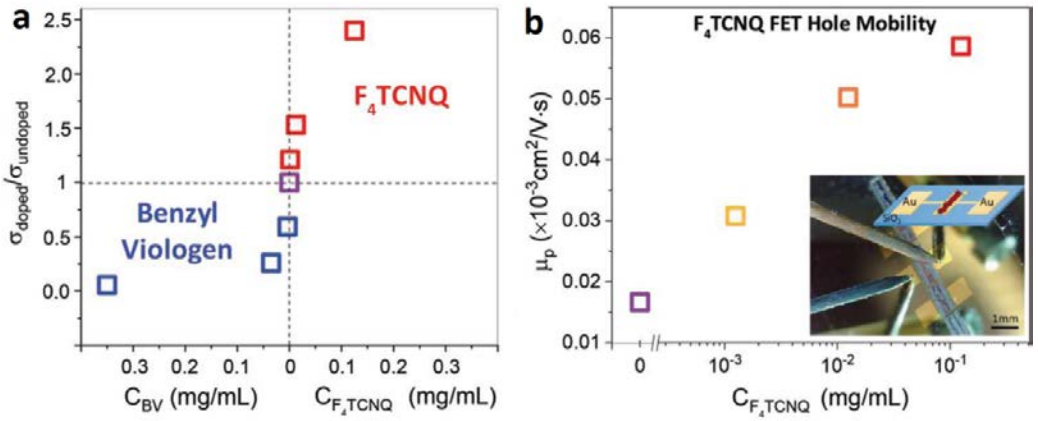


*Figure 2.4. a) The ratio of conductivity between the doped/undoped films as a function of the doping concentration. b) FET hole mobility as a function of $F_4TCNQ$ concentrations. Reprinted from Gaulding et al. Adv. Mater. 2019, 31, 1902250*[7].

Following the same approach, Euvrard *et al.*[33] adapted the ionization potential of the perovskite to the F4TCNQ dopant by adjusting the perovskite composition. The use of $CH_3NH_3Pb_{0.5}Sn_{0.5}I_3$ for the efficient p-doping was an excellent choice, as the LUMO level of the dopant is now lower than the VBM level of the perovskite. The conductivity increased by up to five orders of magnitude (Figure 2.5). The contribution of the dopant to the conductivity increase was confirmed by the AC Hall measurement and ultraviolet photoemission spectroscopy (UPS). Using the CRPH measurements, an increase of the majority carrier lifetime by over one order of magnitude was reported. Likely, it was caused by the passivation of deep traps in the host perovskite. To date, this is the highest mobility increase resulting from perovskite doping reported in literature.

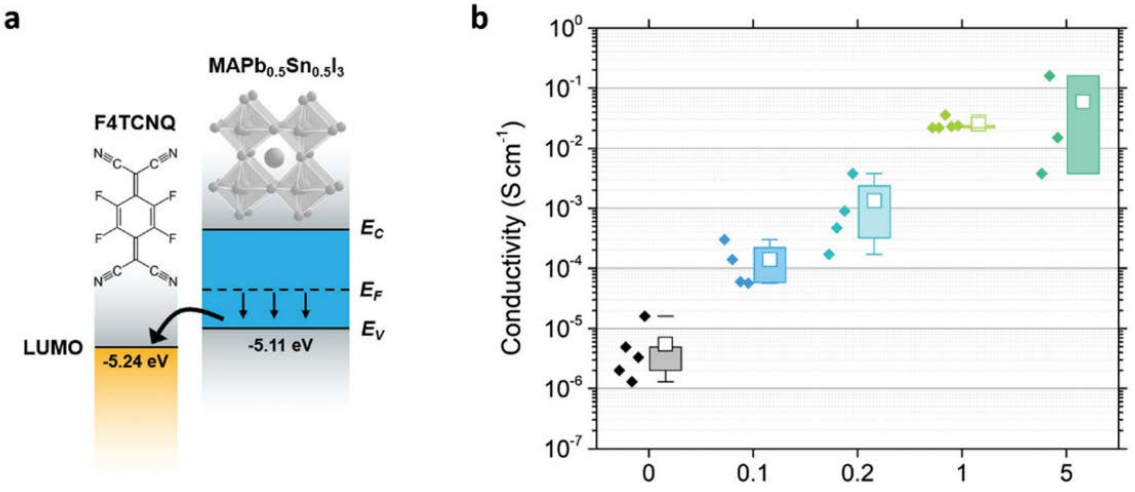


*Figure 2.5. a) LUMO level of the F4TCNQ and VBM ($E_V$) level of $CH_3NH_3Pb_{0.5}Sn_{0.5}I_3$, b) conductivity increase upon doping.*

## 2.3 Doping by substitution

Substitutional doping can be executed using homo- or heterovalent dopants. Inspired by silicon, a heterovalent dopant could potentially carry an extra charge in the conduction band (electron) or valence band (hole) that could shift the Fermi level, resulting in a more n- or p-type semiconductor, respectively. The homovalent doping however will be energetically favorable and therefore technically easier to accomplish. As it will be shown in the next paragraphs, some attempts have been done with moderate impact on the electronic properties.

The crystal lattice conservation is a crucial starting point for efficient doping. Hao *et al.*[34] highlight the importance of the crystal lattice conservation in perovskites, such as the solid solution $MASn_{1-x}Pb_xI_3$ (x = 0.25, 0.50 or 0.75), and this can be extended also to doping. This group demonstrated that the more distorted the crystal lattice, the less conductive the crystal. The authors claim that this trend can be extended to the carrier mobility by assuming identical carrier concentrations for all the samples. The measurement of the Seebeck coefficient of $MASn_{1-x}Pb_xI_3$ revealed that all the solid solutions behave like n-type semiconductors, with the Seebeck coefficient and charge carrier concentration increasing with the increase of Sn content. Carrier concentration was found to be $\sim 1.1 \times 10^{14}$ $cm^{-3}$ for $CH_3NH_3SnI_3$ and $\sim 4.8 \times 10^{11}$ $cm^{-3}$ for $CH_3NH_3PbI_3$, with the values for solid solutions lying in between. This renders $CH_3NH_3SnI_3$ more n-type than $CH_3NH_3PbI_3$, perhaps due to partial $Sn^{2+}$ oxidation to $Sn^{4+}$, resulting in the increase of electron density in the conduction band.

The complete the understanding of the impact of doping perovskites on their electronic properties such as conductivity and charge carrier mobility is a starting point for doping engineering. Yet, molecular simulations give a relatively fast and inexpensive insight into electrical properties. Phung *et al.*[18] proposed the comparison of $MAPbI_3$ doped with $Mg^{2+}$ and $Sr^{2+}$, as these two elements share similar chemical properties but their ionic radii differ significantly (72 and 118 pm, respectively). The results of density functional theory (DFT) simulations, presented in Figure 2.6, show that the incorporation of $Mg^{2+}$ and $Sr^{2+}$ may occur as $Pb^{2+}$ substitution ($Sr_{Pb}$ or $Mg_{Pb}$), $MA^+$ substitution ($Sr_{MA}^+$ or $Mg_{MA}^+$) or it can be interstitial ($Sr_i^{2+}$ or $Mg_i^{2+}$). As a result of the calculations, the group concludes that at small doping concentrations (<0.5% for $Sr^{2+}$ and < 2% for $Mg^{2+}$), the dopants will substitute $Pb^{2+}$ and $MA^+$ ions. When the doping concentration increases, dopant ions start occupying interstitial positions. They hypothesize that the majority of the dopant is not incorporated in the perovskite structure, as the maximum concentration of Schottky defects calculated for the perovskite lattice is 1%. Therefore, if the role of dopants is to heal the harmful behavior of the defects, their concentration should not be more than 1%

of the $Pb^{2+}$ ions. However, in most reports on using doped perovskite to increase performance of solar cells, only higher doping concentrations can be found[35–37]. Using hard X-ray photoelectron spectroscopy (HAXPES), it was confirmed that nominal doping concentrations of over 0.5% are no longer consistent with the concentrations measured in the sample and that significant $Sr^{2+}$ surface segregation occurs above this value. Surprisingly, for $Mg^{2+}$ this effect was noted above 2%.

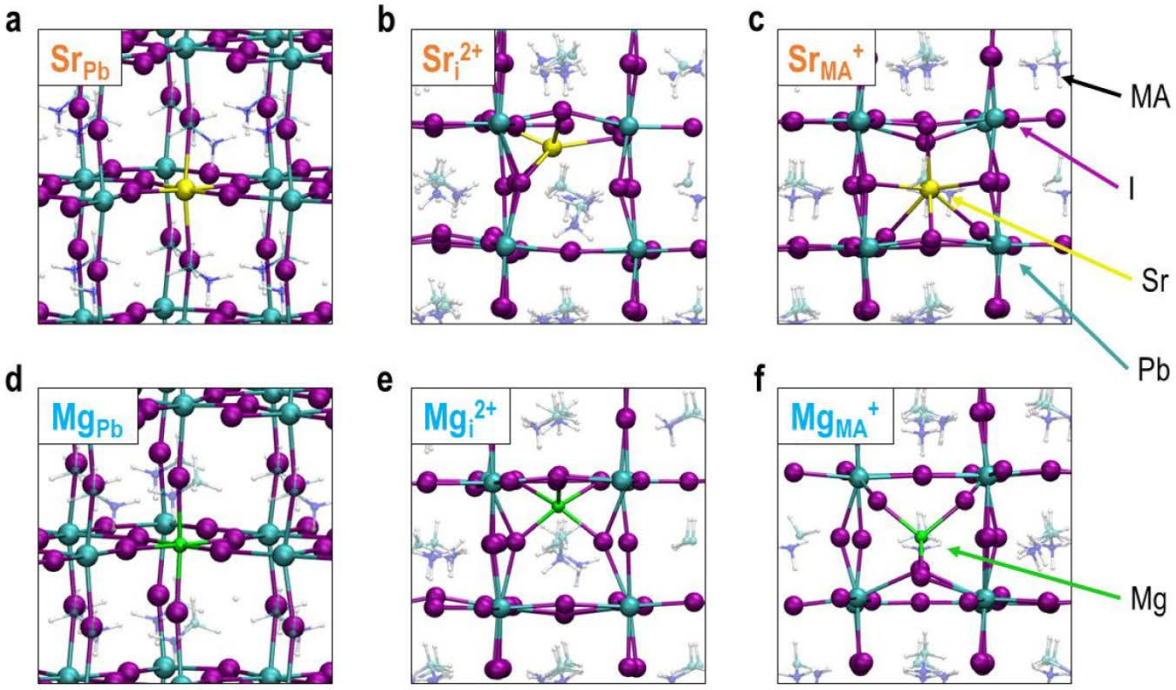


*Figure 2.6. Doping mechanism calculated using DFT. Visualization of Sr doping (depicted in yellow) a) $Pb^{2+}$ substitution by $Sr^{2+}$ ($Sr_{Pb}$), b) interstitial $Sr^{2+}$ ($Sr_i^{2+}$), and c) methylammonium (MA) substitution by $Sr^{2+}$ ($Sr_{MA}^{+}$). Mg doping (depicted in green) as a) $Pb^{2+}$ substitution by $Mg^{2+}$ ($Mg_{Pb}$), b) interstitial $Mg^{2+}$ ($Mg_i^{2+}$), and c) MA substitution by $Mg^{2+}$ ($Mg_{MA}^{+}$). Reprinted with permission from N. Phung et al., J. Am. Chem. Soc. 2020, 142, 5, 2364-2374*[18].

The position of the valence band maximum (VBM) relative to the Fermi level ($E_F$) measured by HAXPES for the Sr-doped $MAPbI_3$ increases slightly when increasing the doping concentration, imposing slightly more n-type doping below 0.5% and slightly less n-type character above this value. For Mg-doped perovskites the tendency is similar, while the threshold value is 2% of the doping concentration, which was illustrated in Figure 2.7 (dashed line is the $E_F$ for the undoped film). As one can see, even small doping concentration can impact $E_F$. However, these changes cannot be considered significant. Therefore, as expected, homovalent substitution doping is not suitable to significantly enhance the conductivity.

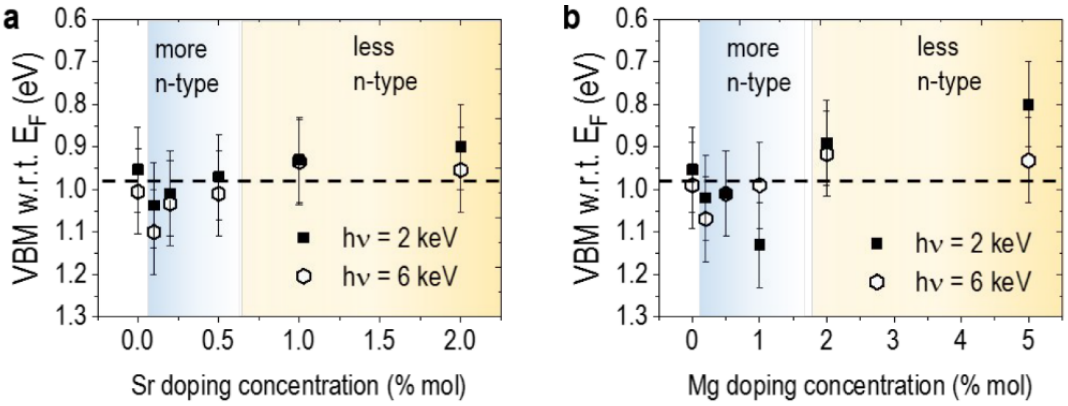


*Figure 2.7. The valence band maximum (VBM) position of undoped and $MAPbI_3$ and doped with various concentrations of Sr (a) and Mg (b), derived from 2 and 6 keV HAXPES data. The Fermi level of the undoped samples is marked by dashed lines. Reprinted with permission from N. Phung et al., J. Am. Chem. Soc. 2020, 142, 5, 2364-2374*[18].

As mentioned previously, heterovalent doping implies the introduction of additional electrons or holes to the perovskite crystal structure. Therefore, it can be considered a good strategy for enhancing the conductivity. However, in ionic crystals such as perovskites, the direct introduction of a heterovalent ion can create a Schottky defect, induced by the presence of the counter ion. This phenomenon may cancel the doping effect, leaving behind only a distorted lattice and decreased mobility.

As $Pb^{2+}$ substitution has a great influence on the electronic structure of perovskites, its heterovalent doping is being actively investigated[38,39]. Doping $CsPbBr_3$ nanocrystals with $Ce^{3+}$ was done by Yao *et al*. for the application in light emitting diodes[40]. $Ce^{3+}$ was selected due to its similar radius to $Pb^{2+}$, that mitigated the lattice distortion. Moreover, the additional energy states introduced with $Ce^{3+}$ are above the CBM of $CsPbBr_3$. Even though the explanation was not provided by the authors, it is presumed that this can be due to partial $Sn^{2+}$ oxidation to $Sn^{4+}$, resulting in the increase of electron density in the conduction band. As a result of such doping, the photoluminescence quantum yield (PLQY) improved by a factor of two. It is proposed that the additional energy levels act as lower excitonic states, resulting in higher luminescence intensity.

As reported by Abdelhady *et al*.[38], the incorporation of trivalent $Bi^{3+}$, $Au^{3+}$ or $In^{3+}$ into $MAPbX_3$ can be used to grow doped single crystals from liquid phase, by adding salts to the precursor solution. Thanks to the retrograde solubility of perovskites, only one solvent and moderated temperature were required. It was demonstrated that the introduction of $Bi^{3+}$ does not impact the crystal structure (within the XRD accuracy) and that it strongly enhances the conductivity of the crystal from nearly $10^{-8}$ $\Omega^{-1}$ $cm^{-1}$ for the undoped crystal to around $10^{-4}$ $\Omega^{-1}$ $cm^{-1}$ for 5% and 10% of Bi/Pb. The Hall effect measurements were

consistent with an n-type doping with an electron density of about $10^{11}$ to $10^{12}$ $cm^{-3}$ for the doping concentration of $Bi^{3+}$ of $10^{19}$ $cm^{-3}$ (measured by inductively coupled plasma optical emission spectrometry). This discrepancy is probably due to the presence of counter ions (possibly lead vacancies $V_{Pb}^{2-}$). Through the Hall effect study, it was possible to show that the type of majority carriers in $MAPbBr_3$, which is known to be a p-type semiconductor[41], changes from holes to electrons, becoming an n-type semiconductor. The charge carrier density remains low in spite of a very high doping level. This implies that only a small fraction of the dopants releases an electron, probably due to a high activation energy. This assumption is supported by the presence of a band tail measured by UV-Vis absorption. Moreover, the doping causes a narrowing of the band gap[38] changing the color of the crystals. This result is however disputed by Nayak *et al*.[42], that claim that the change in the absorption spectra is due to increased density of defect induced states within the bandgap which, combined with using a thick sample for the measurement, gives an illusion of the color change and narrowing of the bandgap. Clearly, the Bi/Pb substitution leads to an increase of the charge carrier density but it is mostly due to defect formation and probably still too low to have an impact on the thin film based devices.

Band gap structure simulations calculated by DFT were performed by Tang *et al*.[43] on $MAPbI_3$ and $FAPbI_3$ doped with Bi, Sn and Tl ions on the Pb-site. Although the oxidation state is not mentioned in this report, it is assumed that the most common ions were used, i.e $Bi^{3+}$, $Sn^{4+}$ and $Tl^{1+}$. Due to the donor defect in the Bi-doped $MAPbI_3$/$FAPbI_3$ the Fermi level occurs in the conduction band, while the Sn-doped perovskite is a direct bandgap semiconductor at the *G* point. Compared to the undoped material, the bandgap narrows (from1.50 eV to 1.30 eV for $MAPbI_3$ and from 1.57 eV to 1.40 for $FAPbI_3$). Tl-doping introduces shallow acceptor defects in the $MAPbI_3$/$FAPbI_3$ structure, therefore the Fermi level is slightly below the valence band maximum. This should indicate a metallic character of the doped perovskite, resulting probably from the very high concentration of Tl used for the simulation. This and a great impact on the bandgap suggests that the doping concertation was relatively high, although it was not mentioned by the authors. Total and partial density of states (DOS) plots (Figure 2.8) show the major contribution of doping atoms to the electronic structure of $MAPbI_3$/$FAPbI_3$. Electronic states near the Fermi level of Bi- and Tl- doped $MAPbI_3$/$FAPbI_3$ are mainly due to the dopant contribution (Figure 2.8a, d, c, f). For the Sn-doped $MAPI_3$/$FAPbI_3$, one can see the overlap of Pb and Sn partial DOS, as a result of the same outer electron configuration of these atoms.

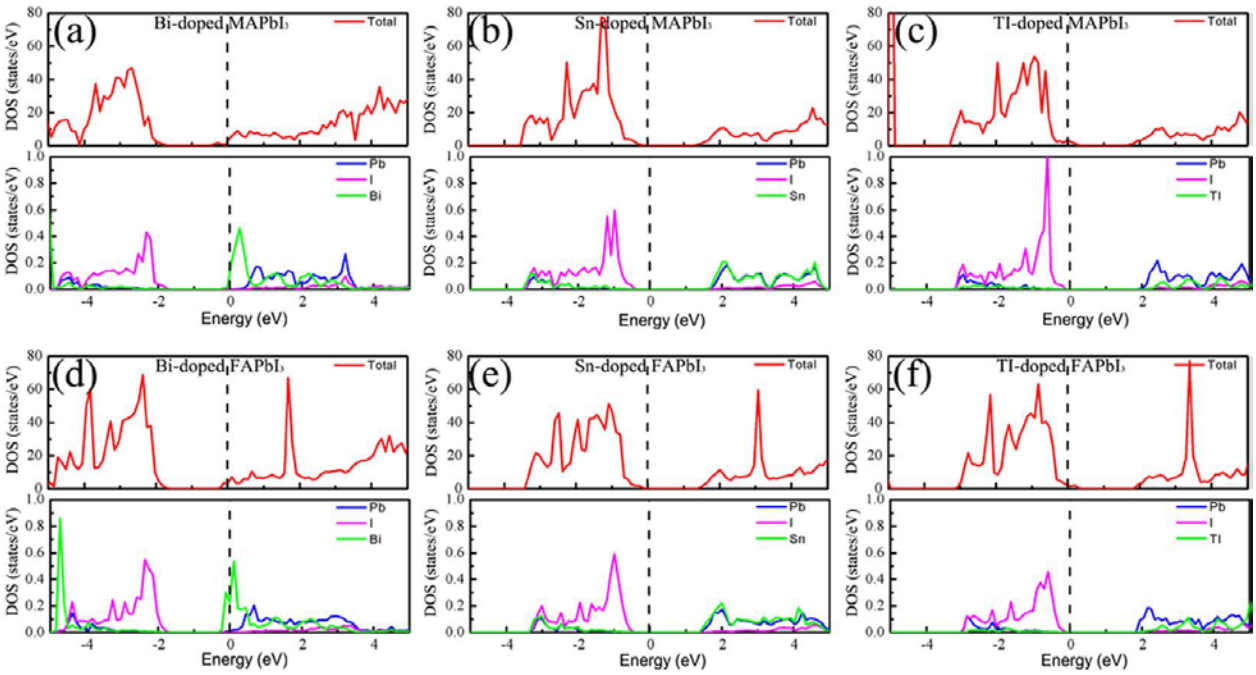


*Figure 2.8. The total DOS and partial DOS of Pb, I, and defect in the Bi- (a) Sn- (b) and Tl-doped (c) $MAPbI_3$, as well as Bi- (d), Sn- (e) and Tl-doped (f) $FAPbI_3$. Reprinted from Z.-K. Tang et al., Sci. Rep 7, 7843 (2017)*[43].

As suggested in the previous paragraph, the doping concentration can greatly impact the resulting properties of the semiconductor. It determines the position of the guest atoms and its role in the host material. If the function of doping is to fit in the defects and thus to improve the periodicity of the crystal, eliminating carrier trap centers and increasing the conductivity, then the doping concentration should be relatively low. In most of the experimental reports, however, we find that the doping concentration is around 10 mol% and the improvements in electrical conductivity is still evidenced. The main reason for this observation may be the reduction of the band gap. It suggests that either the material is rather an alloy than a doped perovskite, or that the energy states of the dopants are close to the valence band maximum or conduction band minimum of the doped material. Moreover, as shown in the research of Phung *et al.*[18], small concentrations of $Mg^{2+}$ and $Sr^{2+}$ resulted in more n-type character of the semiconductor while the increase of the doping concentration caused shifting of the Fermi level towards the valence band as more holes are introduced to the structure. This causes the change of the material's character to less n-type. Also, heterovalent doping was proved to increase the conductivity, mobility of charge, free charge carriers' concentrations and causes change from p-type to n-type semiconductor upon doping[38,39]. In this case, careful selection of the dopant element is necessary.

**Conclusions**

Perovskite doping is a promising, yet not fully explored, way of modifying the properties of this interesting family of compounds. Firstly, changes in the optical properties can be observed, as a result of reduced bandgap. Stability enhancement can be achieved when the doping concentration is tuned in order to heal the negative effect of defects in the crystal lattice. However, in this chapter, stress was put on the influence of doping on the perovskite's electronic properties, semiconductor type modulation, increase of the conductivity and charge carrier concentration and mobility.

Even though the field of perovskites is now booming, there are still relatively few studies about doping impact on electrical properties and complete understanding of the doping mechanism remains a challenge. The lack of a systematic approach in previous studies leads to apparently contradictory conclusions. It seems that even the role of basic parameters such as the doping concentration is still not understood. While most reports show the doping level around 10 mol%, the actual incorporation of the dopant atoms into the crystal structure occurs mainly in place of Schottky defects, whose concentration is usually around 1%. The excess atoms will then likely aggregate on the surface of the grain boundaries. In some cases, the excess of dopant can distort the lattice order, thus impeding charge transport, which may eventually lead to a drop in the conductivity. However, many researchers report an improvement of the electronic properties at such high doping levels. High concentration of guest atoms, residing mainly in the interstitial positions, can introduce additional energy states within the bandgap, which may give an illusion of a bandgap reduction. Correctly adjusted doping concentration of a carefully selected dopant element may finally lead to a significant improvement of conductivity, mobility of charge carrier, free charge carrier concentrations and change the type of semiconductor from p-type (typical for perovskite) to n-type.

On the other hand, $PbI_2$ aggregation on the grain boundaries can increase charge carrier density and recombination lifetime, electron carrier density and ambipolar diffusion length, while decreasing trap density, thereby reducing the occurrence of trap-assisted recombination. This sort of perovskite grain passivation is indeed widely used in perovskite solar cells fabrication and is known to improve the efficiency of the devices[30,44–47].

To date, the greatest influence of the doping on the perovskite conductivity was achieved by Euvrard *et al*. for p doping using organic dopant and by Abdelhady *et al*., for n doping using $Bi^{3+}$ substitution at the $Pb^{2+}$ site. The improvement of the electrical properties, especially conductivity and

charge carrier density, was predicted by simulations, as well as demonstrated experimentally. Doping has then been proved to be a promising tool in tuning electronic properties of perovskites applied in devices. Still, a lot needs to be done to establish a quantitative impact of the doping on these properties. Witnessing huge and still growing interest in the field of perovskite, as well as an extremely fast development of perovskite-based devices, it is tempting to say that interest in perovskite doping will continue to grow in the near future.

**References**


[1] Z. Molenda, S. Chambon, D. M. Bassani, L. Hirsch, *Eur. J. Inorg. Chem.* **2021**, *2021*, 2533.

[2] T. M. Brenner, D. A. Egger, L. Kronik, G. Hodes, D. Cahen, *Nat. Rev. Mater.* **2016**, *1*, DOI 10.1038/natrevmats.2015.7.

[3] A. Fakharuddin, L. Schmidt-Mende, G. Garcia-Belmonte, R. Jose, I. Mora-Sero, *Adv. Energy Mater.* **2017**, *7*, DOI 10.1002/aenm.201700623.

[4] J. Euvrard, Y. Yan, D. B. Mitzi, *Nat. Rev. Mater.* **2021**, *6*, 531.

[5] P. Cui, D. Wei, J. Ji, H. Huang, E. Jia, S. Dou, T. Wang, W. Wang, M. Li, *Nat. Energy* **2019**, *4*, 150.

[6] T. Kirchartz, D. Cahen, *Nat. Energy* **2020**, 1.

[7] E. A. Gaulding, J. Hao, H. S. Kang, E. M. Miller, S. N. Habisreutinger, Q. Zhao, A. Hazarika, P. C. Sercel, J. M. Luther, J. L. Blackburn, *Adv. Mater.* **2019**, *31*, 1.

[8] T. Qiao, D. Parobek, Y. Dong, E. Ha, D. H. Son, *Nanoscale* **2019**, *11*, 5247.

[9] D. Parobek, B. J. Roman, Y. Dong, H. Jin, E. Lee, M. Sheldon, D. H. Son, *Nano Lett.* **2016**, *16*, 7376.

[10] T. A. Cohen, T. J. Milstein, D. M. Kroupa, J. D. Mackenzie, C. K. Luscombe, D. R. Gamelin, *J. Mater. Chem. A* **2019**, *7*, 9279.

[11] M. Righetto, D. Meggiolaro, A. Rizzo, R. Sorrentino, Z. He, G. Meneghesso, T. C. Sum, T. Gatti, F. Lamberti, *Prog. Mater. Sci.* **2020**, *110*, 100639.

[12] S. Wang, Y. Zhu, C. Wang, R. Ma, *Org. Electron.* **2020**, *78*, 105627.

[13] J. Yin, G. H. Ahmed, O. M. Bakr, J. L. Brédas, O. F. Mohammed, *ACS Energy Lett.* **2019**, *4*, 789.

[14] W. Li, Z. Wang, F. Deschler, S. Gao, R. H. Friend, A. K. Cheetham, *Nat. Rev. Mater.* **2017**, *2*, DOI 10.1038/natrevmats.2016.99.

[15] B. Saparov, D. B. Mitzi, *Chem. Rev.* **2016**, *116*, 4558.

[16] X. Zhang, L. Li, Z. Sun, J. Luo, *Chem. Soc. Rev.* **2019**, *48*, 517.

[17] O. Gunawan, S. R. Pae, D. M. Bishop, Y. Virgus, J. H. Noh, N. J. Jeon, Y. S. Lee, X. Shao, T. Todorov, D. B. Mitzi, **2019**, *575*.

[18] N. Phung, R. Félix, D. Meggiolaro, A. Al-Ashouri, G. Sousa E Silva, C. Hartmann, J. Hidalgo, H. Köbler, E. Mosconi, B. Lai, R. Gunder, M. Li, K. L. Wang, Z. K. Wang, K. Nie, E. Handick, R. G. Wilks, J. A. Marquez, B. Rech, T. Unold, J. P. Correa-Baena, S. Albrecht, F. De Angelis, M. Bär, A. Abate, *J. Am. Chem. Soc.* **2020**, *142*, 2364.

[19] N. K. Noel, A. Abate, S. D. Stranks, E. S. Parrott, V. M. Burlakov, A. Goriely, H. J. Snaith, *ACS Nano* **2014**, *8*, 9815.

[20] D. W. DeQuilettes, S. M. Vorpahl, S. D. Stranks, H. Nagaoka, G. E. Eperon, M. E. Ziffer, H. J. Snaith, D. S. Ginger, *Science (80-. ).* **2015**, *348*, 683.

[21] R. Naphade, B. Zhao, J. M. Richter, E. Booker, S. Krishnamurthy, R. H. Friend, A. Sadhanala, S. Ogale, *Adv. Mater. Interfaces* **2017**, *4*, 1.

[22] X. Zheng, B. Chen, J. Dai, Y. Fang, Y. Bai, Y. Lin, H. Wei, X. C. Zeng, J. Huang, *Nat. Energy* **2017**, *2*, 1.

[23] S. Sadhu, K. Aqueche, T. Buffeteau, J. M. Vincent, L. Hirsch, D. M. Bassani, *Mater. Horizons* **2019**, *6*, 192.

[24] N. K. Noel, S. N. Habisreutinger, A. Pellaroque, F. Pulvirenti, B. Wenger, F. Zhang, Y. H. Lin, O. G. Reid, J. Leisen, Y. Zhang, S. Barlow, S. R. Marder, A. Kahn, H. J. Snaith, C. B. Arnold, B. P. Rand, *Energy Environ. Sci.* **2019**, *12*, 3063.

[25] A. Pellaroque, N. K. Noel, S. N. Habisreutinger, Y. Zhang, S. Barlow, S. R. Marder, H. J. Snaith, *ACS Energy Lett.* **2017**, *2*, 2044.

[26] D. Ramirez, K. Schutt, J. F. Montoya, S. Mesa, J. Lim, H. J. Snaith, F. Jaramillo, *J. Phys. Chem. C* **2018**, *122*, 21239.

[27] J. Euvrard, O. Gunawan, D. B. Mitzi, *Adv. Energy Mater.* **2019**, *9*, DOI 10.1002/aenm.201902706.

[28] Q. Chen, H. Zhou, T. Bin Song, S. Luo, Z. Hong, H. S. Duan, L. Dou, Y. Liu, Y. Yang, *Nano Lett.* **2014**, *14*, 4158.

[29] L. Wang, C. McCleese, A. Kovalsky, Y. Zhao, C. Burda, *J. Am. Chem. Soc.* **2014**, *136*, 12205.

[30] T. Zhang, N. Guo, G. Li, X. Qian, Y. Zhao, *Nano Energy* **2016**, *26*, 50.

[31] O. Gunawan, S. R. Pae, D. M. Bishop, Y. Virgus, J. H. Noh, N. J. Jeon, Y. S. Lee, X. Shao, T. Todorov, D. B. Mitzi, B. Shin, *Nature* **2019**, *575*, 151.

[32] O. G. Reid, D. T. Moore, Z. Li, D. Zhao, Y. Yan, K. Zhu, G. Rumbles, *J. Phys. D. Appl. Phys.* **2017**, *50*, DOI 10.1088/1361-6463/aa9559.

[33] J. Euvrard, O. Gunawan, X. Zhong, S. P. Harvey, A. Kahn, D. B. Mitzi, *Mater. Adv.* **2021**, *2*, 2956.

[34] F. Hao, C. C. Stoumpos, R. P. H. Chang, M. G. Kanatzidis, *J. Am. Chem. Soc.* **2014**, *136*, 8094.

[35] W. Zhao, Z. Yao, F. Yu, D. Yang, S. F. Liu, *Adv. Sci.* **2018**, *5*, 1.

[36] H. Choi, J. Jeong, H. B. Kim, S. Kim, B. Walker, G. H. Kim, J. Y. Kim, *Nano Energy* **2014**, *7*, 80.

[37] S. Colella, E. Mosconi, P. Fedeli, A. Listorti, A. Rizzo, F. Gazza, F. Orlandi, P. Ferro, T. Besagni, G. Calestani, F. De Angelis, R. Mosca, G. Gigli, *Mater. Res. Soc. Symp. Proc.* **2014**, *1667*, DOI 10.1557/opl.2014.898.

[38] A. L. Abdelhady, M. I. Saidaminov, B. Murali, V. Adinolfi, O. Voznyy, K. Katsiev, E. Alarousu, R. Comin, I. Dursun, L. Sinatra, E. H. Sargent, O. F. Mohammed, O. M. Bakr, *J. Phys. Chem. Lett.* **2016**, *7*, 295.

[39] X. Miao, T. Qiu, S. Zhang, H. Ma, Y. Hu, F. Bai, Z. Wu, *J. Mater. Chem. C* **2017**, *5*, 4931.

[40] J. S. Yao, J. Ge, B. N. Han, K. H. Wang, H. Bin Yao, H. L. Yu, J. H. Li, B. S. Zhu, J. Z. Song, C. Chen, Q. Zhang, H. B. Zeng, Y. Luo, S. H. Yu, *J. Am. Chem. Soc.* **2018**, *140*, 3626.

[41] D. Shi, V. Adinolfi, R. Comin, M. Yuan, E. Alarousu, A. Buin, Y. Chen, S. Hoogland, A. Rothenberger, K. Katsiev, Y. Losovyj, X. Zhang, P. A. Dowben, O. F. Mohammed, E. H. Sargent, O. M. Bakr, *Science (80-. ).* **2015**, *347*, 519.

[42] P. K. Nayak, M. Sendner, B. Wenger, Z. Wang, K. Sharma, A. J. Ramadan, R. Lovrinčić, A. Pucci, P. K. Madhu, H. J. Snaith, *J. Am. Chem. Soc.* **2018**, *140*, 574.

[43] Z. K. Tang, Z. F. Xu, D. Y. Zhang, S. X. Hu, W. M. Lau, L. M. Liu, *Sci. Rep.* **2017**, *7*, 1.

[44] Y. Chen, Q. Meng, Y. Xiao, X. Zhang, J. Sun, C. B. Han, H. Gao, Y. Zhang, Y. Lu, H. Yan, *ACS Appl. Mater. Interfaces* **2019**, *11*, 44101.

[45] B. Shi, X. Yao, F. Hou, S. Guo, Y. Li, C. Wei, Y. Ding, Y. Li, Y. Zhao, X. Zhang, *J. Phys. Chem. C* **2018**, *122*, 21269.

[46] M. C. Shih, S. S. Li, C. H. Hsieh, Y. C. Wang, H. D. Yang, Y. P. Chiu, C. S. Chang, C. W. Chen, *Nano Lett.* **2017**, *17*, 1154.

[47] J. an Yang, A. Xiao, L. Xie, K. Liao, X. Deng, C. Li, A. Wang, Y. Xiang, T. Li, F. Hao, *Electrochim. Acta* **2020**, *338*, 135697.

# 3. Optimization of solar cell fabrication parameters

## 3.1 Solar cell architecture and reproducibility

In the literature, one can find a variety of ideas on how to design an efficient perovskite solar cell[1]. In principle, there are three different architectures, as described in Chapter 1. Additionally, different perovskite compositions can be used as well as different materials for the charge transporting layers and electrodes. As a starting point of this work, the procedure developed by Chen *et al*.[2] was employed. The device architecture is presented in Figure 3.1 and it relies on the use of poly(3,4-ethylenedioxythiophene) polystyrene sulfonate (PEDOT:PSS) as a hole transporting layer and [6,6]-phenyl-C61-butyric acid methyl ester (PCBM) as an electron transporting layer. For the absorber, the well-known methylammonium lead triiodide ($CH_3NH_3PbI_3$ or MAPI) was used. While MAPI is a common perovskite for solar cells, there are many methods of its synthesis. Most publications report MAPI synthesis from dissolving methylammonium iodide ($CH_3NH_3I$ or MAI) and lead iodide ($PbI_2$) in *N*,*N*-dimethylformamide (DMF) with or without the addition of dimethylsulfoxide (DMSO). The solution is spin coated on a substrate, resulting in a compact and crystallized MAPI layer after annealing on a hot plate. When employing this method for the device fabrication, it is necessary to add a drop of an antisolvent during the spin coating process to locally increase the solution concentration, thus leading to a rapid crystallization and a smoother film[3]. Alternatively, a two-step process can be employed: first the $PbI_2$ is spin coated onto the substrate, followed by MAI dissolved in an orthogonal solvent (e.g. isopropanol). The two compounds react during annealing and result in a crystallized layer. Both approaches follow the reaction below.

$$PbI_2 + CH_3NH_3I \rightarrow CH_3NH_3PbI_3 \tag{3.1}$$

An alternative procedure uses lead acetate trihydrate ($Pb(C_2H_3O_2)_2 \cdot 3H_2O$) as a lead source and MAI with the molar ratio 1:3. Interestingly, an alternative name for lead acetate is lead sugar, due to its historical use as a diet wine and food sweetener[4–6]. This procedure was surprising at the time it emerged, as water was thought to be detrimental to perovskite formation. Later it was also found that this method can induce the incorporation of dimethylammonium into the crystal structure[7]. Yet it gained popularity in 2015 mainly due to its simple one-step procedure and smooth layers without the need of the antisolvent[8]. In this work, the lead acetate based method will be employed.

In order to prove that the material synthesized using this method is indeed MAPI, the XRD pattern is shown in the Figure 3.2. Four peaks characteristic of the MAPI tetragonal phase are present at 14.1°, 28.4°, 43.2° and 58.9°. These correspond to the 110, 220, 330 and 440 Miller planes, respectively[9].

Additionally, the peak at 31.8°, corresponding to the 213 plane, can be noticed. A small peak at 12.4° corresponds to residual presence of PbI2, which occurs commonly[10–12]. Since the diffraction experiment was performed on the thin film, and not on a powder, one can observe the diffraction peaks that correspond only to one crystallographic orientation.

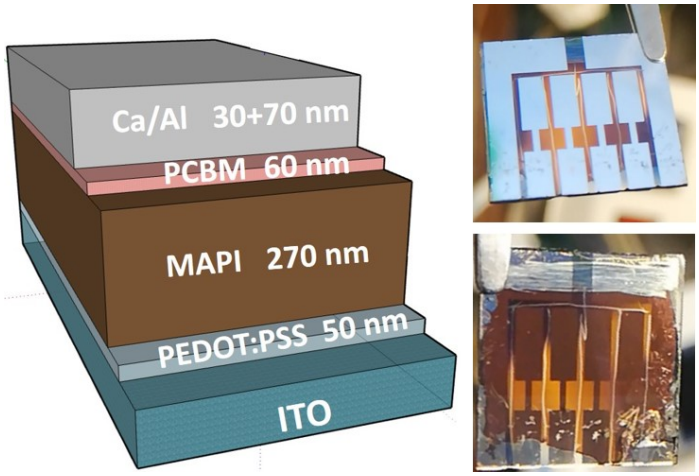


*Figure 3.1. Left: perovskite solar cell device structure, right: photograph of the device from the metal electrode side on the top and ITO side on the bottom.*

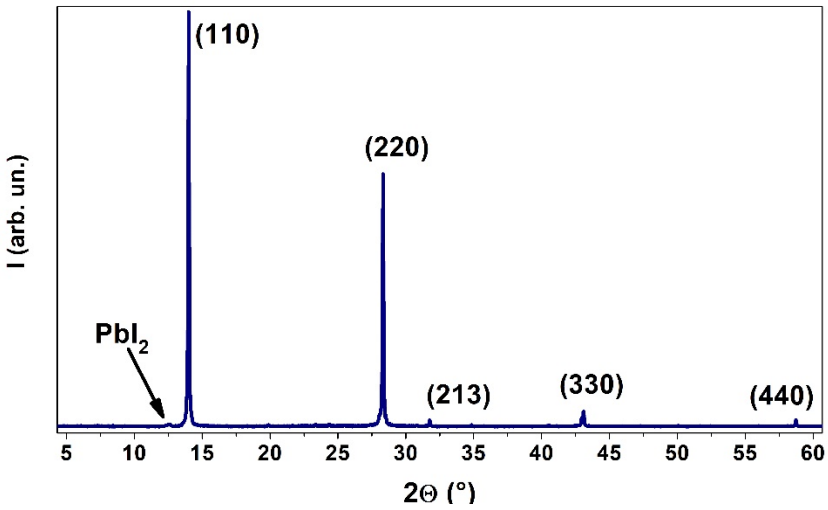


*Figure 3.2. XRD pattern of the MAPI layer, used for solar cells.*

The absorption spectrum of the thin film presented in the Figure 3.3 shows the typical absorption spectrum of MAPI, with an absorption edge at 780 nm, which is consistent with a bandgap of 1.63 eV, as shown in the Tauc plot in the inset. The photoluminescence peak falls near the absorption edge. The absorption over the whole visible spectrum and the direct narrow bandgap make MAPI an attractive candidate for solar cells.

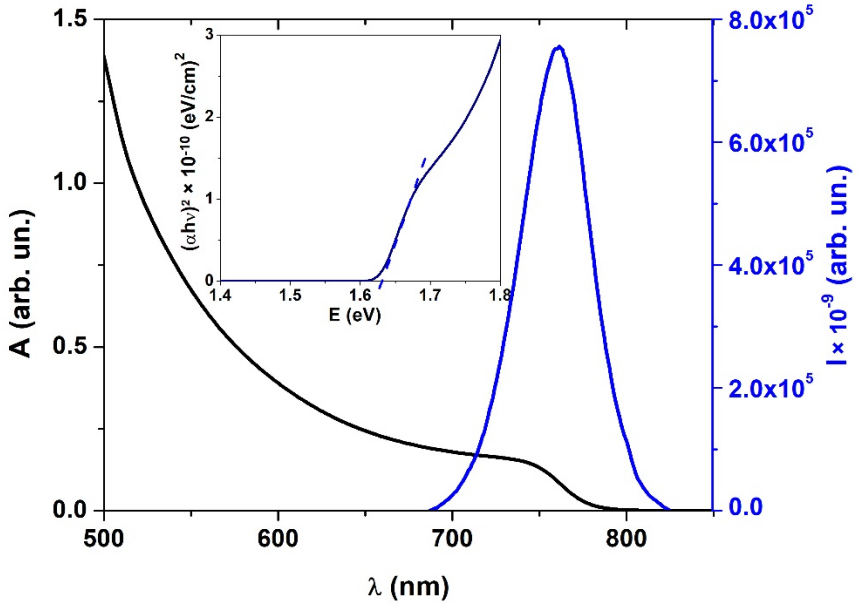


*Figure 3.3. Absorption and photoluminescence spectra of MAPI un the visible region and Tauc plot in the inset.*

Figure 3.4 shows the atomic force microscopy (AFM) image of the MAPI polycrystalline film. The grain size ranges from 50 to 200 nm and it should allow for effective charge separation. Grain boundaries can act as charge recombination sites. Therefore, larger grains are favorable for efficient solar cells. The average roughness calculated from the AFM profile is around 6 nm, which suggests that the layer is sufficiently smooth to avoid detrimental pin holes.

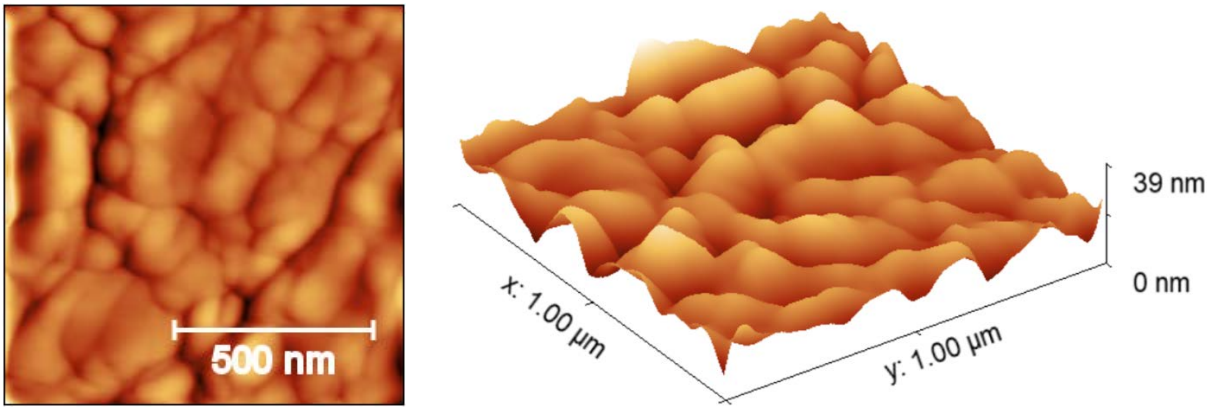


*Figure 3.4. AFM image of a MAPI thin film. Left: top view, right: profile*.

Phenyl-C61-butyric acid methyl ester (PCBM) is a material widely used in organic photovoltaics as an acceptor[13–15] and it is also a popular choice for an electron transporting material in perovskite solar

cells[16–18]. In particular, it has a good solubility in organic solvents, such as chlorobenzene or toluene, which do not dissolve perovskites, hence they can be used in PSCs. Since it was first synthesized in 1990s[19], the cost of its product has not decreased, making it a rather poor candidate for the large scale production of solar cells.

Poly(3,4-ethylenedioxythiophene) (PEDOT) doped with polystyrene sulfonate (PSS) is a common choice for the hole transporting material in organic photovoltaics (OPV) due to its VBM alignment with the HOMO level of the most common absorbers, such as poly(3-hexylthiophene) (P3HT)[20] or poly[*N*-9'-heptadecanyl-2,7-carbazole-alt-5,5-(4,7-di-2-thienyl-2',1',3'-benzothiadiazole] (PCDTBT)[21] and high conductivity (4000 - 5000 S/cm[22,23]). It has been also widely used in organic light emitting diodes (OLED)[24–26], organic electrochemical transistors[27], sensors[28] and potentially even as a flexible and transparent electrode[29,30]. It owes its high conductivity to the delocalized π-electrons within its chemical structure and doping with polystyrene sulfonate[31]. PEDOT:PSS with different acidity, viscosity and conductivity are commercially available.

The VBM of PEDOT:PSS is also compatible with the VBM of many perovskites suitable for an active layer in optoelectronic devices, such as MAPI or FAPI. Together with the fact that common perovskite solvents (DMF and DMSO) do not dissolve PEDOT:PSS, it makes the latter a suitable candidate for the HTL for the perovskite based devices such as solar cells, as well as a hole injection material in perovskite light-emitting diodes (PeLED)[32,33].

On the other hand, due to its acidity (hence hydrophilicity), PEDOT:PSS is a site of the moisture uptake, which causes the perovskite decomposition[34,35], resulting in a fast device degradation. Another important drawback is that PEDOT:PSS is a subject of doping by halides present in the perovskite[36], causing an increase of the conductivity by two orders or magnitude and creating halide defects in the perovskite.

Perovskite solar cells with PEDOT:PSS as an HTL were fabricated using different conditions, as indicated in Table 3.1.1. The maximum *PCE* value for this batch reached 6.84% (JV curve in Figure 3.5), which is still below the value reported in the literature for this device architecture[37,38]. The $V_{OC}$ values are between 482 and 611 mV, also much lower than expected. The reason for the low $V_{OC}$ and consequently low *PCE* can be due to pin holes and/or high density of defects in the perovskite layer. Additionally, pin holes can result in high leakage current, leading to a low shunt resistance, since charges find an alternative path to reach the electrodes. Low *FF* can indicate again high charge recombination rate, probably due to

poor crystal quality with numerous recombination sites, such as crystal defect or maybe even harmful impurities. The $J_{SC}$ values spread from 11.13 to 18.79 mA/cm$^2$. Low $J_{SC}$ indicates ineffective charge collection by the charge transporting layers or the recombination of the charge before it reaches the charge transporting layers. The concentration of 40% wt. and moderate spinning rates, from 2500 to 4500 rpm, result in the best solar cells performance, finding a balance between the layer too thin to absorb enough light and susceptible to pin holes (low concentration, low spinning rate) and too thick to obtain a fairly good quality crystals and low surface roughness (high concentration, high spinning rate).

*Table 3.1.1. PCE, $V_{OC}$ and $J_{SC}$ dependence on the perovskite solution concentration and spin coating rate.*

| PCE (%) | | concentration | | |
|---|---|---|---|---|
| | | 40% | 44% | 48% |
| f (rpm) | 1500 | 3.07 | 4.49 | 4.86 |
| | 2500 | 6.12 | 4.59 | 4.30 |
| | 3500 | 6.84 | 5.36 | 3.59 |
| | 4500 | 6.51 | 5.60 | 4.32 |

| $V_{OC}$(mV) | | concentration | | |
|---|---|---|---|---|
| | | 40% | 44% | 48% |
| f (rpm) | 1500 | 495 | 548 | 592 |
| | 2500 | 591 | 554 | 565 |
| | 3500 | 611 | 566 | 482 |
| | 4500 | 608 | 577 | 540 |

| $J_{SC}$ (mA/cm$^2$) | | concentration | | |
|---|---|---|---|---|
| | | 40% | 44% | 48% |
| f (rpm) | 1500 | 11.13 | 14.36 | 14.38 |
| | 2500 | 18.66 | 14.95 | 14.16 |
| | 3500 | 18.51 | 17.30 | 13.39 |
| | 4500 | 18.79 | 16.57 | 14.22 |

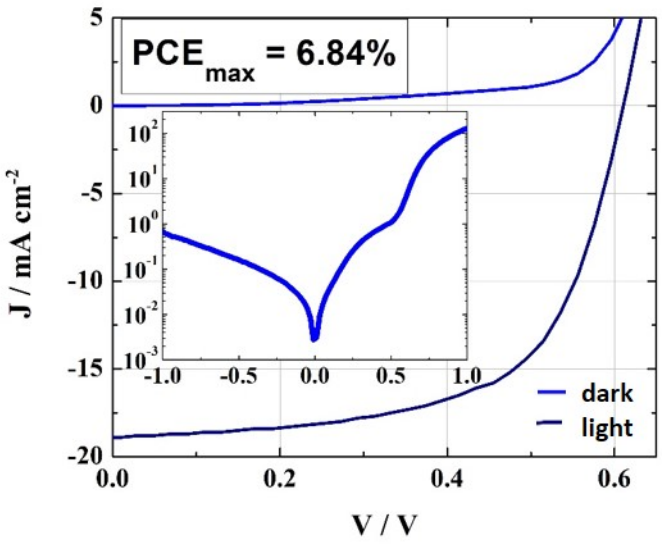


*Figure 3.5. JV characteristics for the device with the highest PCE. Inset: dark current in the semi logarithmic scale.*

To make sure that the materials used as the charge transporting layers are the optimal choice, four different electron transporting layers and three hole transporting layers were tested. First, the following ETLs were screened, whereas the HTL (PEDOT:PSS) remained unchanged:

- PCBM, 20 mg dissolved in 1 mL of chlorobenzene and spin coated at 2500 rpm, resulting in a 60 nm thick layer;
- $C_{60}$, one of the fullerenes, known also as buckminsterfullerene or buckyball. Contrarily to its derivative, PCBM, it is not soluble in most solvents, therefore the 30 nm film was thermally evaporated;
- ZnO nanoparticles, a well-known transparent ETL in organic electronics, mainly due to its transparency, annealing-free and solution-processable features and high mobility[39,40]; spin coated from a dispersion in ethanol, resulting in an ultrathin film < 10 nm;
- PDINO, which is a common name of 2,9-Bis[3-(dimethyloxidoamino)propyl]anthra[2,1,9-def:6,5,10-d'e'f']diisoquinoline-1,3,8,10(2H,9H)-tetrone, which is typically used as an interlayer between the active layer and the high work function metal electrode in organic electronic devices[41–43]; spin coated from a solution in methanol (1mg/mL, spin coated at 1000 rpm).

All the ETLs used were applied either on top of PCBM or as stand-alone, resulting in 7 different combinations, listed in Figure 3.6. Additionally, two different electrodes were used: either a Ca/Al (30 and 70 nm thick, respectively) or Ag electrode (100 nm thick), marked with an asterisk in the Figure 3.6. The error is the standard deviation from 2 to 22 devices used for the study.

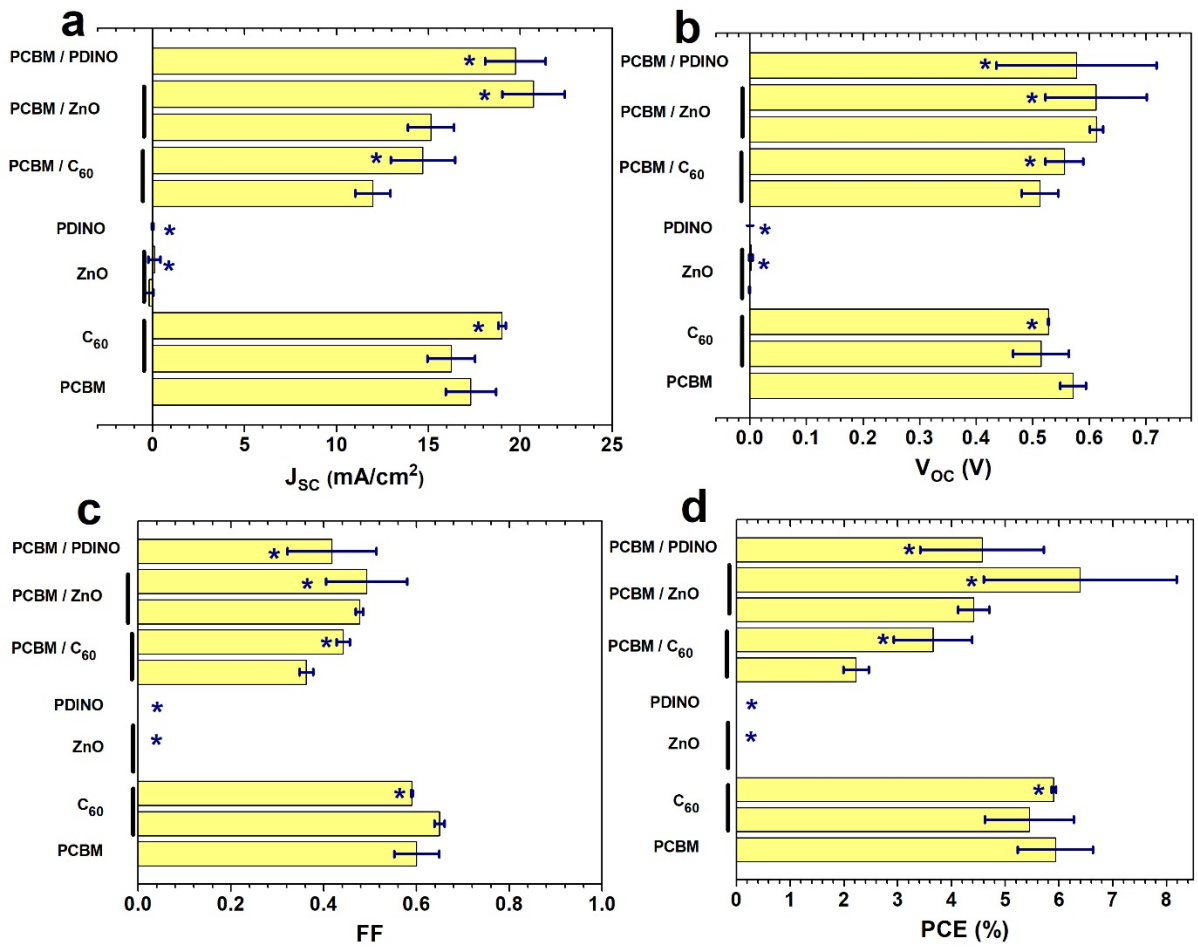


*Figure 3.6. $J_{SC}$ (a), $V_{OC}$ (b), FF(c) and PCE (d) of the solar cells with various ETLs. For the devices marked with an asterisk, an Ag electrode was used, instead of Ca/Al.*

As a first observation, one can notice that the devices with only PDINO and ZnO are inefficient. In case of PDINO, it can be due to a difference between its LUMO level and the CBM level of the perovskite[42]. These levels match well for ZnO, nevertheless, the devices are not functional. This can be due to incomplete film coverage, leading to direct contact between the perovskite layer and the electrode and it can take place both for ZnO- and PDINO-based devices. However, these same materials, when employed on top of a PCBM layer, increased the $V_{OC}$ and $J_{SC}$ in some samples, suggesting that in some cases they facilitated the electron transport. The standard deviation is however much higher than for the set with PCBM only, indicating the possibility of inhomogeneous coverage with these materials. Moreover, the *FF* is decreased for all these sets of devices. This can result from an increased series resistance or decreased shunt resistance. The solar cells parameters from the devices with $C_{60}$ were comparable to the PCBM references, which could result from the similarity of the two materials. It Is interesting to note that the change of the electrode from Ca/Al to silver increased the $J_{sc}$ for all the examined ETLs, however, the

improvement was within the error of the reference PCBM sample. Furthermore, a stack of PCBM and $C_{60}$ resulted in a decrease of the $J_{SC}$, $V_{OC}$ and *FF*, resulting in an obvious decrease of the *PCE*. The problem likely lies in the ETL thickness, considering that each of these materials alone lead to the devices with similar efficiency.

As a result, considering that the set of devices with double ETL composed of PCBM and ZnO resulted in only a minor improvement in the PCE, but high standard deviation, it was decided to proceed with the unchanged reference sample architecture, employing only PCBM as an ETL. However, taking into account that 6% ± 1% efficiency is far below the state-of-the-art, alternative HTLs to PEDOT:PSS were explored. In view of the well-known drawbacks of PEDOT:PSS, such as hydrophilicity, this approach is justified. The HTLs employed in this study, other than PEDOT:PSS are the following:

- NiOx, synthesized by the sol-gel method[44], from 0.1 M solution of nickel acetate tetrahydrate in ethanol with 0.6% etanolamine. The solution was stirred at 50°C for 24h and spin coated at 3000 rpm, followed by annealing at 275°C for 45 min and resulting in the thickness of 30nm,
- PTAA or poly(triaryl amine) with a molecular weight 17 kDa and concentration of 4.5 mg in toluene, spin coated at 6000 rpm and annealed at 100°C for 10 min, resulting in the layer thickness of 15 nm.

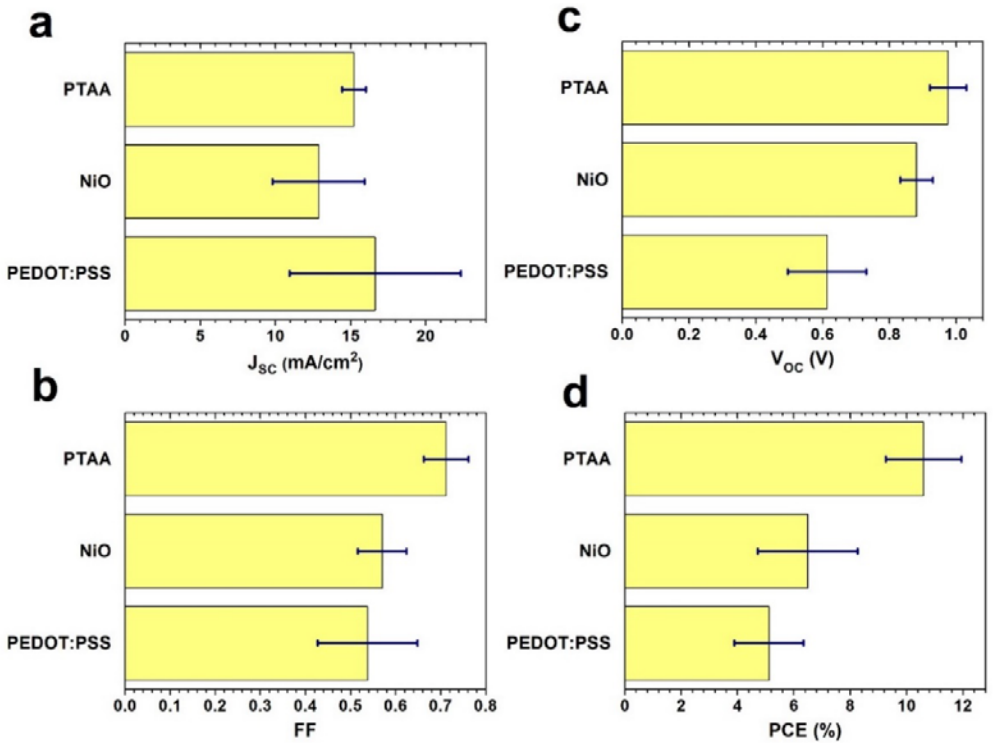


*Figure 3.7. $J_{SC}$, $V_{OC}$, FF and PCE of the solar cells with various HTLs.*

The results are presented in the Figure 3.7. While the $J_{SC}$, including the standard deviation error, remained comparable for all three HTLs employed, the $V_{OC}$ drastically increased both for NiOx, by almost 50%, and for PTAA, by up to 67%. This suggests improved charge extraction and mobility, probably due to a more neutral interface than in case of PEDOT:PSS, which is known for its high acidity[45]. This is the reason behind PEDOT:PSS's high hydrophilicity, making this layer a site of moisture intake in the device. It has been also shown that the halides of the perovskites tend to migrate into the PEDOT:PSS layer, which increases the conductivity of PEDOT:PSS and creates halide vacancies in the perovskite[36]. All these reasons may stand behind the lowest performance of the devices with PEDOT:PSS as an HTL. While inorganic NiOx should not face similar problems, it clearly results in the devices with lower PCE than the devices with PTAA. In fact, its ionization energy is the lowest, comparing to the one of PTAA and PEDOT:PSS[46,47] (Figure 3.8). The valence energy of the PTAA is between those of MAPI and the top electrode, which could stand behind a better performance of the solar cells with PTAA. Another reason behind a poorer performance of the solar cells with NiOx can be a substrandard film morphology or probable low purity of the synthesized NiOx.

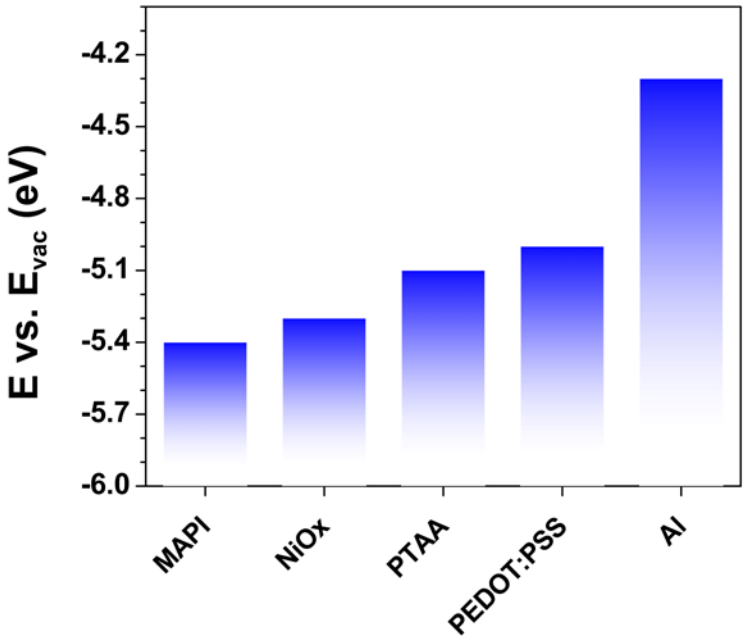


*Figure 3.8. Ionization energies of the investigated HTLs, in comparison with the ionization energy of MAPI and the work function of the top electrode[46,47].*

The most remarkable increase of *FF* was observed for the devices with PTAA (0.71 ± 0.05), with respect to the devices with PEDOT:PSS (0.54 ± 0.11) and NiOx (0.57 ± 0.05), leading to an increase of the PCE from (5.1 ± 1.2) for PEDOT:PSS and (6.5 ± 1.8) % for NiOx to (10.6 ± 1.3) % for PTAA, thus passing the psychological limit of the 2-digit efficiency number, with the champion device of PCE = 13.4%. Its JV characteristics are shown in Figure 3.9. The low leakage current indicates a significant improvement of the active layer's quality, comparing to the first experiments, with less recombination sites probably resulting from a reduction of the interfacial defect density.

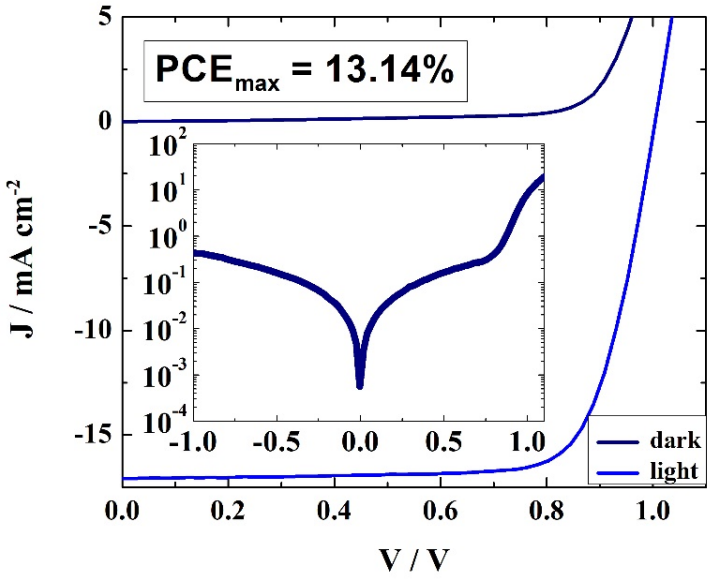


*Figure 3.9. JV characteristic of the champion device with the architecture of ITO / PTAA / MAPI / PCBM / Ca / Al.*

**Conclusions**

In this section, the synthesis of MAPI thin films from lead acetate trihydrate and methylammonium iodide was reported and the obtained films were then characterized using AFM, XRD, UV-Vis absorption spectroscopy and photoluminescence. Four different ETLs and three different HTLs were tested using a planar inverted device structure. The solar cell architecture resulting in the best PCE was the one with PTAA as an HTL and PCBM as an ETL, with an average *PCE* = (10. 6 ± 1.3) %, and a champion cell efficiency of 13.14%. Obtaining good reproducibility and a reasonable efficiency is a starting point for further studies, in which the effect of ambient fabrication temperature will be explored.

## 3.2. Ambient Temperature Impact on the PSC Performance

In the process of the parameter optimization for the solar cells fabrication, one parameter was found to play a very important role in the overall performance of MAPI-based solar cells. This parameter is the ambient temperature inside the glove box, where the active layer is fabricated. The results presented in this section were published in 2021[48].

The temperature inside a glove box can vary throughout the day and across seasons by around 10°C. This is valid for Bordeaux, where all the experiments took place, but it is believed that the situation is similar in most laboratories around the world. In 2020, Han et al.[49] demonstrated that the performance of perovskite-based light emitting diodes (PeLEDs) depended on the ambient temperature over the range of 21-31°C, as the 2D perovskite with the formula of $PEA_2MA_{n-1}Pb_nBr_{3n-1}$ changes its crystallographic orientation. At around 21°C, the cubic crystals lay horizontally on the substrate, while higher temperatures favor vertical orientation. These structural changes influence the electrical and optical properties, impacting the device performance. Moreover, the standard deviation in the observed devices efficiencies increases from 9.9% for 21°C to 71.4% for 31°C.

In this section it will be shown that perovskite solar cell fabrication can also be impacted by the ambient temperature and that it has a profound effect on the efficiency and standard deviation of the device parameters. It will be shown that variations in the deteriorated crystal quality in the polycrystalline film are responsible for the solar cells' decreased performance when prepared at higher ambient temperatures. In particular, increased defect density of the perovskite layer fabricated at 30°C reduces the average efficiency by a factor of over 2.5.

To study the impact of ambient temperature on the photovoltaic performances of MAPI based solar cells, a total of 85 perovskite solar cell devices were prepared at 3 different temperatures inside the glovebox: 20°C, 25°C and 30°C. In the glove box where these samples were prepared, the temperature deviation for this study was ±1°C. The PSCs of devices with the inverted architecture were investigated using MAPI as an active layer sandwiched between poly(triaryl amine) (PTAA) as a hole transporting layer (HTL) and phenyl-$C_{61}$-butyric acid methyl ester (PCBM) as an electron transporting layer (ETL). The device architecture is shown in Figure 3.10.

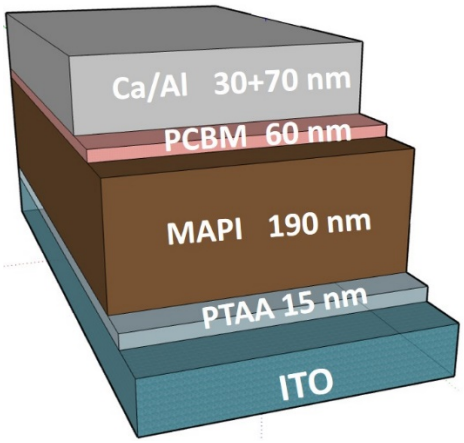


*Figure 3.10. Schematic representation of the device architecture, used in the ambient temperature study.*

The key solar cell parameters were analyzed in order to assess the impact of the ambient temperature. The power conversion efficiency (*PCE*), open circuit voltage ($V_{oc}$) and short circuit current density ($J_{sc}$) of solar cell devices prepared at different ambient temperatures inside of the glovebox are shown in Figure 3.11. While the *PCE* is the highest for the devices prepared at 20°C and 25°C (on average 11.0 ± 1.7 % and 9.2 ± 2.2 % respectively), the cells prepared at the temperature of 30°C show that the efficiencies decrease to 4.3 ± 2.1 % on average. Moreover, it is worth noting that the standard deviation increases drastically with the increase of a temperature in the glovebox. Also, $J_{sc}$ has the highest average value and the lowest standard deviation for the fabrication at 20°C (14.8 ± 0.5 mA $cm^{-2}$), whereas devices processed at 25°C and 30°C present lower $J_{sc}$ and increasingly higher standard deviation, 14.0 ± 1.4 mA $cm^{-2}$ and 10.4 ± 3.0 mA $cm^{-2}$, respectively. The $V_{oc}$ does not change significantly between 20°C and 25°C (0.99 ± 0.02 V and 0.99 ± 0.01 V, respectively), while a significant decrease is observed at 30°C (0.79 ± 0.17 V).

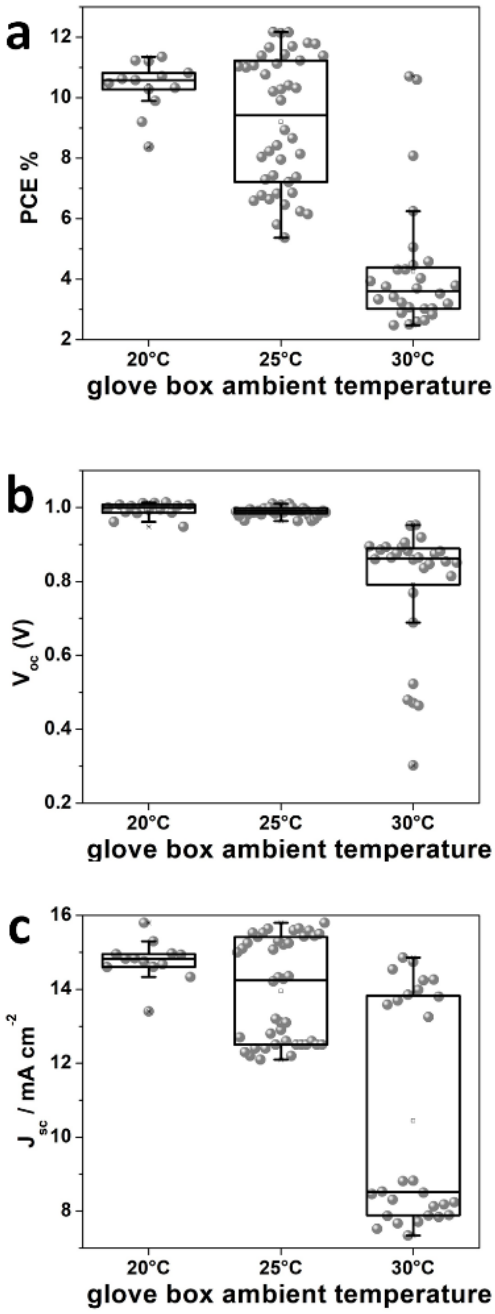


*Figure 3.11. Power conversion efficiency (a), open circuit voltage (b) and short circuit current (c) of the perovskite solar cells prepared at different ambient temperatures.*

To understand the reason for such a spread of the solar cells parameters and notably, the efficiency, the morphology of the active layers prepared at three different ambient temperatures was probed using atomic force microscopy (AFM). AFM images for the different samples are presented in Figure 3.12. At first glance, the crystalline grain shape appears sharper, with better defined edges for the

lowest temperature probed (Figure 3.12a), while for samples prepared at 25°C and 30°C (Figure 3.12b, c) the grains more rounded. Moreover, low temperature favors the fabrication of slightly smoother surfaces, as the root mean square roughness (*RMS*) is the lowest for the lowest fabrication temperature (1.0 nm), a little higher for 25°C (1.3 nm) and the highest for 20°C (2.2 nm). In spite of the fact that the grain size distribution (Figure 3.12d-f) indicates that the smallest grains were fabricated at 20°C (~100 nm), they seem to be better defined than the larger grains obtained at 25°C and 30°C (~150 nm and ~250 nm respectively).

The X-ray diffraction pattern (XRD) for active layers prepared at the three different ambient temperatures is presented in Figure 3.13a. All exhibit four peaks typical for MAPI at 14.1°, 28.4°, 43.2° and 58.9° that correspond, respectively, to the (110), (220), (330) and (440) crystallographic planes of the tetragonal structure[9]. A small peak at 12.7° reveals the presence of a trace amount of $PbI_2$ and it is found in all three samples. The patterns are almost the same, with the difference of the intensity of the main peaks, with the highest corresponding to the sample prepared in the lowest ambient temperature, which suggests improved crystalinity for these conditions, compared to higher ambient temperatures. Using the Scherrer equation below, it is possible to quantify the differences in the crystal quality $\tau$ [50,51].

$$\tau = \frac{K\lambda}{\beta cos\theta} \tag{3.2}$$

Where *K* is a shape factor, assumed to be 0.9 for most perovskites; $\lambda$ is the X-ray wavelength; $\beta$ is the peak broadening at half maximum value (FWHM) and $\theta$ is the Bragg angle. Finally, $\tau$ is he mean size of the ordered crystalline domain. It may, but does not have to be, equal to the grain size and more generally it can serve as a parameter of the crystalline quality of the material. The domain size for the samples fabricated at 20°C is the highest and equal to 53 nm, while for those samples fabricated at 25°C and 30°C it is 36.0 nm and 35.1 nm, respectively. The τ variations with the ambient temperature are pictured in Figure 3.13b.

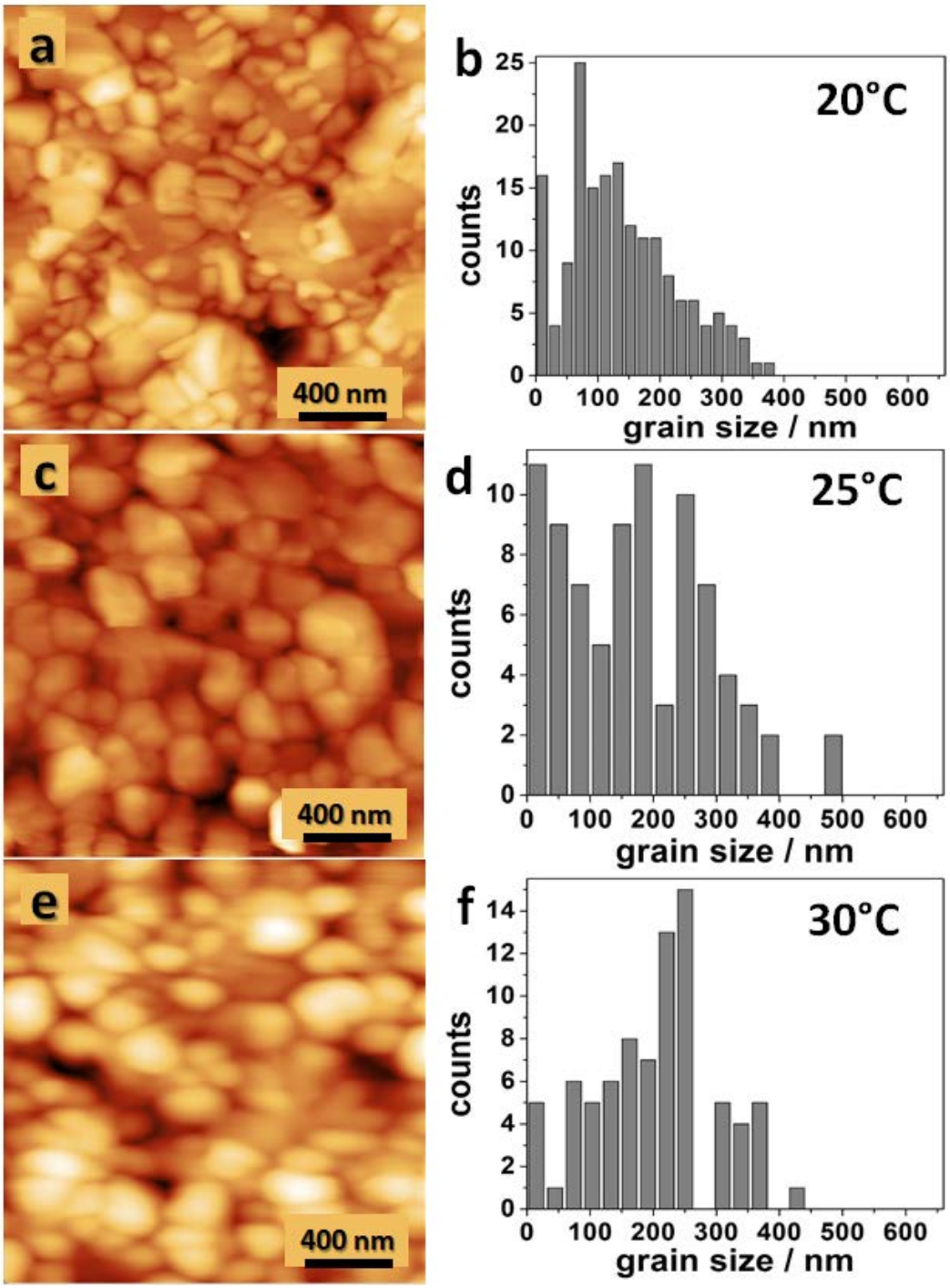


*Figure 3.12. Atomic Force Microscopy images of the 190 nm thick perovskite layer spin coated onto a glass/PTAA substrate, prepared at 20°C (a), 25°C (c) and 30°C (e) and corresponding distributions of the grain size, defined as the distance between the two most distanced points on the AFM images for samples prepared at 20°C (b), 25°C (d) and 30°C (f).*

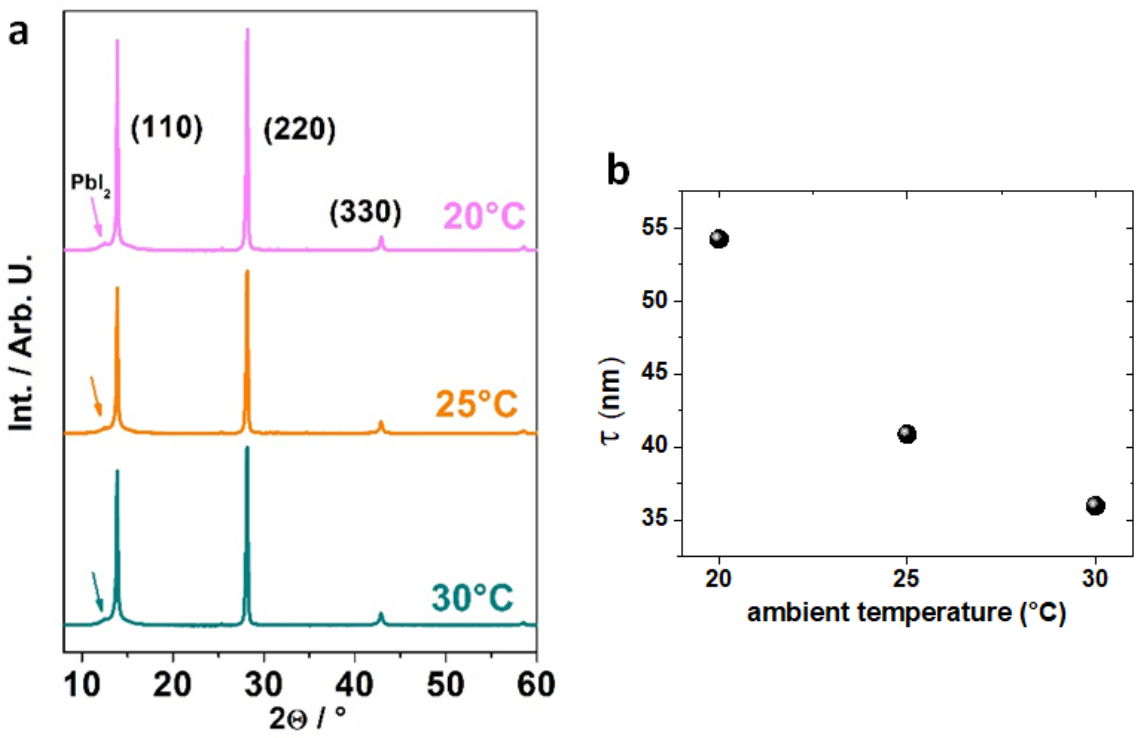


*Figure 3.13. (a) X-ray diffraction pattern of the 190 nm thick perovskite layer spin coated onto a PTAA layer deposited on a glass slide at different ambient temperatures; (b) mean crystalline domain size at different temperatures.*

The absorption spectra of the MAPI films fabricated at 3 different temperatures on a PTAA-coated glass substrate are shown in Figure 3.14 and demonstrate an absorption edge at 752 nm, that corresponds to a band gap of 1.65 eV, that is typical for MAPI[52–54]. These features are the same for all three temperatures. Nevertheless, small differences can be noticed near the absorption edge (Figure 3.14a, inset), with a significant Urbach tail for the sample prepared at 30°C.

Typically, an Urbach tail is associated to the presence of impurities, disorder, or defects in a thin film of a semiconductor[55]. These properties can be quantified by analyzing the Urbach energy $E_U$, as a function of the incident light energy. It was demonstrated that high $E_U$ values correspond to higher charge recombination rates, which contribute to the decrease of the perovskite solar cell's efficiency[56].

The $E_U$ was extracted by plotting the natural logarithm of the absorption coefficient $\alpha$, according to the equations below:

$$\alpha = \alpha_0 exp\left(h\nu {E_U}^{-1}\right) \tag{3.2}$$

$$ln\alpha = \ln(\alpha_0) + \left(h\nu {E_U}^{-1}\right) \tag{3.3}$$

where *h* is Planck's constant, *v* is the frequency of light and $\alpha_0$ is a fitting parameter with the dimension of inverse length. The values of $E_U$ for the samples prepared at 20°C, 25°C and 30°C, extracted from the plots presented in Figure 3.14b are 26 meV, 28 meV and 83 meV, respectively. The $E_U$ reported for MAPI lies between 15 meV[57] and 41 eV[58]. Thus, the $E_U$ values obtained for the samples prepared at 20°C and 25°C are close to the lower limit of this range. In contrast, high $E_U$ for the sample prepared at 30°C suggests much larger charge recombination rates, presumably due to the increased defect density.

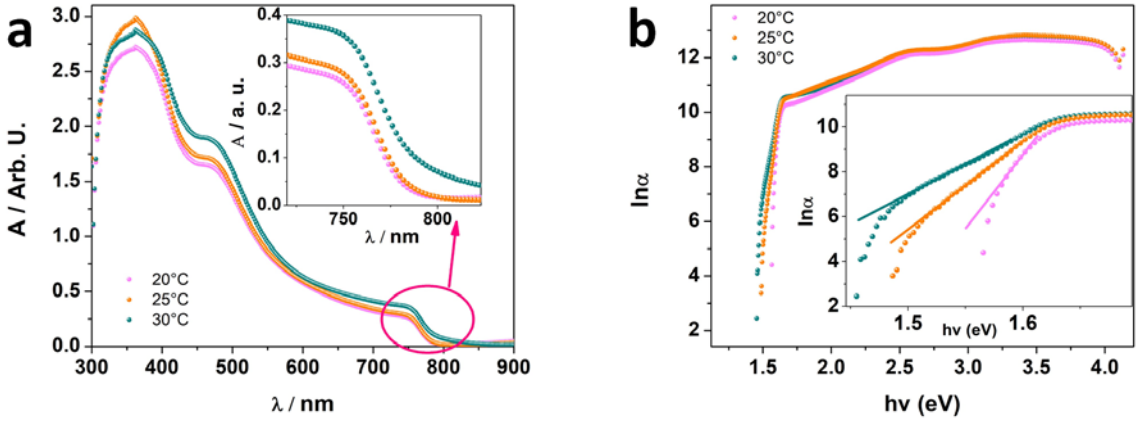


*Figure 3.14. Absorption spectra in the visible light of the 190 nm thick perovskite layer spin coated onto a PTAA layer deposited on a glass slide at different ambient temperatures. The curves are the average of 3 samples per each ambient temperature.*

The EQE spectra of all the samples investigated (Figure 3.15) exhibit a broad contribution of the photons from the visible range to the photocurrent, consistent with the absorption spectra in Figure 3.14. The $J_{sc}$ calculated from the EQE measurement are in agreement with those obtained from the *J-V* curves. The efficiency is significantly different between the three sets for the wavelength ca. 700 nm. It reaches similar values for the samples prepared at 20°C (63 ± 1.6 %) and 25°C (62 ± 1.7 %), but shows a drop in efficiency for those samples prepared at 30°C, reaching only 51 ± 2.4 %. Inefficient photon to electron conversion of red light can be linked to non-radiative losses that might occur due to more numerous defects in the samples produced at 30°C. Their presence was already suggested by the XRD and absorption spectra.

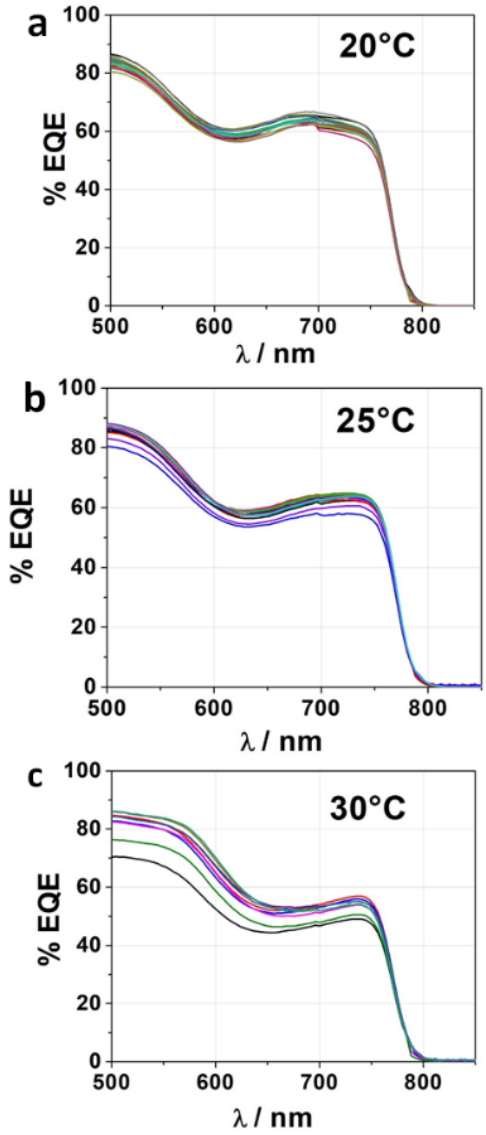


*Figure 3.15. External quantum efficiency spectra for MAPI solar cells fabricated at different temperatures.*

The electroluminescence of perovskite devices typically provides information on the non-radiative recombination processes responsible for the shunt losses[59,60]. They can occur due to a number of processes, such as Auger recombination, band-tail recombination, electron-phonon coupling and defect-assisted recombination[61]. Their impact on the open circuit voltage ($V_{oc}$), short circuit current ($J_{sc}$) and fill factor (*FF*) eventually leads to a decrease of the overall solar cell performance. A high rate of non-radiative recombination may finally cause a significant deterioration of the solar cell's stability, thus impeding their industrialization[62,63]. The electroluminescence of the solar cells prepared at different ambient temperatures is shown in Figure 3.16. Radiative emission was observed between the red and

near infrared range at 770 nm (Figure 3.16a). The highest luminosity $E_v$, observed for the samples prepared at 20°C (0.12 ± 0.03 cd $m^{-2}$) drops to less than a half for those samples prepared at 25°C (0.05 ± 0.02 cd $m^{-2}$). The luminescence of the most samples prepared at 30°C is below the detection limits of the instrumentation (Figure 3.16b). The decrease of the luminosity points at the increase of the losses associated with non-radiative charge recombination processes. Comparing these results with the findings from AFM, XRD and analysis of the absorption spectra, it can be concluded that samples prepared at higher ambient temperatures show higher rates of charge recombination that probably takes place at defect sites within the crystal structure and/or on the grain boundaries. The decrease of the $V_{oc}$ distribution presented in Figure 3.11b for solar cells prepared at 30°C is therefore in agreement with this conclusion. $V_{oc}$ can be thereby rationalized by the splitting the quasi-Fermi levels of the electrons and holes during illumination. The difference between these levels defines the maximum theoretical $V_{oc}$ [64,65] and non-radiative losses effectively limit the split of the quasi-Fermi levels, thus reducing the achievable $V_{oc}$.

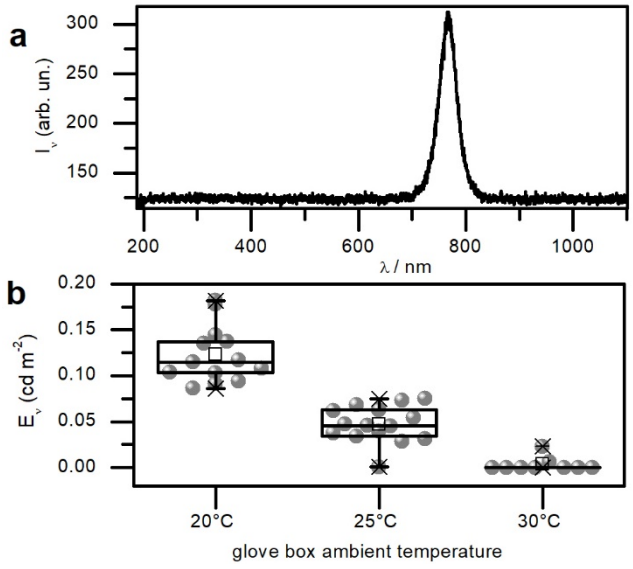


*Figure 3.16. a) EL spectrum from the sample emitting the highest intesity light; b) electroluminescence at +2.5 V of the devices produced in different ambient temperatures.*

**Conclusions**

In this chapter, the impact of the ambient temperature inside the glovebox during the preparation of MAPI films was investigated. The decrease in *PCE* observed for the samples prepared at higher ambient temperatures is related to changes in morphology, as evidenced from the comparison of the AFM images,

XRD and presence of Urbach tail. These results confirm the significant impact of the ambient temperature on the density of structural defects in MAPI. Electroluminescence analysis points out that these defects act as non-radiative recombination centers that are likely the cause of the decrease in $V_{oc}$, $J_{sc}$, *FF*, and hence to a decrease of the *PCE*. Within all the devices investigated, those prepared at 20°C demonstrate the best photo conversion efficiency, which drops dramatically when the temperature is incremented by only 10°C. Such a small increase in ambient temperature can easily occur in glove boxes located in most laboratory environments due to seasonal or daily fluctuations as a result of thermal treatments (e.g. annealing). The crystallization process, being one of the factors that determine the overall performance, is related not only to the crystallization temperature, but also to the partial vapor pressure of the solvents used. The latter typically increases with increasing temperature[66], thereby affecting the evaporation rate during the spin coating process.

It is further concluded that that temperatures >25°C result in reproducibly lower *PCE*, and that this decrease can be assigned to the increased density of traps within the bandgap of the perovskite. The electrical characterization of devices prepared at different temperatures, shows that higher quality perovskite crystals may be formed at lower ambient temperatures and that this can contribute to increased *PCE* through more efficient charge extraction. Processing the active layer at lower ambient temperature would be expected to lower the concentration of defects. As a consequence, the number of recombination centers decreases, thus minimizing shunt losses induced by this recombination. This mechanism impacts directly all the other solar cells parameters, such as $V_{oc}$ and $J_{sc}$. Finally, if the temperature was not controlled, i.e. considering all the devices prepared for this experiment, the standard deviation of the PCE would reach 42%.

Establishing the fabrication parameters of the solar cells is a baseline for further work, in which doping can be used in devices. Perovskite doping is believed to help to improve the solar cells efficiency by pinning the quasi Fermi hole and electron levels at the valence band maximum and conduction band minimum, respectively. This would lead to the maximization of the $V_{OC}$ up to the value of the semiconductor bandgap, leading to a significant increase of the PCE.

**References**

[1] M. Saliba, J. P. Correa-Baena, C. M. Wolff, M. Stolterfoht, N. Phung, S. Albrecht, D. Neher, A. Abate, *Chem. Mater.* **2018**, *30*, 4193.

[2] Y. Chen, **2017**.

[3] N. J. Jeon, J. H. Noh, Y. C. Kim, W. S. Yang, S. Ryu, S. Il Seok, *Nat. Mater.* **2014**, *13*, 897.

[4] A. C. Dies, *Biographische Nachrichten von Joseph Haydn*, Camesinaische Buchhandlung, **1810**.

[5] P. Jeandet, S. S. Heinzmann, C. Roullier-Gall, C. Cilindre, A. Aron, M. A. Deville, F. Moritz, T. Karbowiak, D. Demarville, C. Brun, F. Moreau, B. Michalke, G. Liger-Belair, M. Witting, M. Lucio, D. Steyer, R. D. Gougeon, P. Schmitt-Kopplin, *Proc. Natl. Acad. Sci.* **2015**, *112*, 5893.

[6] W. Specht, K. Fischer, *Vergiftungsnachweis an Den Resten Einer 900 Jahre Alten Leiche*, Schmidt-Römhild, **1959**.

[7] W. M. J. Franssen, B. J. Bruijnaers, V. H. L. Portengen, A. P. M. Kentgens, *ChemPhysChem* **2018**, *19*, 3107.

[8] D. Forgács, M. Sessolo, H. J. Bolink, *J. Mater. Chem. A* **2015**, *3*, 14121.

[9] J. A. Chang, J. H. Rhee, S. H. Im, Y. H. Lee, H. J. Kim, S. Il Seok, M. K. Nazeeruddin, M. Gratzel, *Nano Lett.* **2010**, *10*, 2609.

[10] Q. Chen, H. Zhou, T. Bin Song, S. Luo, Z. Hong, H. S. Duan, L. Dou, Y. Liu, Y. Yang, *Nano Lett.* **2014**, *14*, 4158.

[11] B. Shi, X. Yao, F. Hou, S. Guo, Y. Li, C. Wei, Y. Ding, Y. Li, Y. Zhao, X. Zhang, *J. Phys. Chem. C* **2018**, *122*, 21269.

[12] L. Wang, C. McCleese, A. Kovalsky, Y. Zhao, C. Burda, *J. Am. Chem. Soc.* **2014**, *136*, 12205.

[13] Z. Li, K. Ho Chiu, R. Shahid Ashraf, S. Fearn, R. Dattani, H. Cheng Wong, C.-H. Tan, J. Wu, J. T. Cabral, J. R. Durrant, *Sci. Rep.* **2015**, *5*, 1.

[14] M.-A. Pan, T.-K. Lau, Y. Tang, Y.-C. Wu, T. Liu, K. Li, M.-C. Chen, X. Lu, W. Ma, C. Zhan, *J. Mater. Chem. A* **2019**, *7*, 20713.

[15] S. N. Pugliese, J. K. Gallaher, M. A. Uddin, H. S. Ryu, H. Y. Woo, J. M. Hodgkiss, *J. Mater. Chem. C* **2022**, *10*, 908.

[16] Y. Zhong, M. Hufnagel, M. Thelakkat, C. Li, S. Huettner, *Adv. Funct. Mater.* **2020**, *30*, 1908920.

[17] J. Seo, S. Park, Y. Chan Kim, N. J. Jeon, J. H. Noh, S. C. Yoon, S. Il Seok, *Energy Environ. Sci.* **2014**, *7*, 2642.

[18] C. H. Chiang, C. G. Wu, *Nat. Photonics* **2016**, *10*, 196.

[19] J. C. Hummelen, B. W. Knight, F. LePeq, F. Wudl, J. Yao, C. L. Wilkins, *J. Org. Chem.* **1995**, *60*, 532.

[20] A. Kanwat, J. Jang, *J. Mater. Chem. C* **2014**, *2*, 901.

[21] S. Rafique, S. M. Abdullah, M. M. Shahid, M. O. Ansari, K. Sulaiman, *Sci. Rep.* **2017**, *7*, 39555.

[22] E. Jin Bae, Y. Hun Kang, K.-S. Jang, S. Yun Cho, *Sci. Rep.* **2016**, *6*, 1.

[23] K. N. K. S. L. SH, *Adv. Mater* **2014**, *26*, 2268.

[24] W. H. Kim, A. J. Mäkinen, N. Nikolov, R. Shashidhar, H. Kim, Z. H. Kafafi, *Appl. Phys. Lett.* **2002**, *80*, 3844.

[25] K. Fehse, K. Walzer, K. Leo, W. Lövenich, A. Elschner, *Adv. Mater.* **2007**, *19*, 441.

[26] Y. Tao, Q. Wang, C. Yang, K. Zhang, Q. Wang, T. Zou, J. Qin, D. Ma, *J. Mater. Chem.* **2008**, *18*, 4091.

[27] D. Khodagholy, J. Rivnay, M. Sessolo, M. Gurfinkel, P. Leleux, L. H. Jimison, E. Stavrinidou, T. Herve, S. Sanaur, R. M. Owens, others, *Nat. Commun.* **2013**, *4*, 1.

[28] Y. Wen, J. Xu, *J. Polym. Sci. Part A Polym. Chem.* **2017**, *55*, 1121.

[29] J. Lee, Y. H. Kim, *Synth. Met.* **2018**, *242*, 99.

[30] X. Fan, W. Nie, H. Tsai, N. Wang, H. Huang, Y. Cheng, R. Wen, L. Ma, F. Yan, Y. Xia, *Adv. Sci.* **2019**, *6*, 1900813.

[31] W. F. Quirós-Solano, N. Gaio, C. Silvestri, G. Pandraud, P. M. Sarro, *Procedia Eng.* **2016**, *168*, 1184.

[32] X. Yang, X. Zhang, J. Deng, Z. Chu, Q. Jiang, J. Meng, P. Wang, L. Zhang, Z. Yin, J. You, *Nat. Commun.* **2018**, *9*, 1.

[33] K. Lin, J. Xing, L. N. Quan, F. P. G. De Arquer, X. Gong, J. Lu, L. Xie, W. Zhao, D. Zhang, C. Yan, others, *Nature* **2018**, *562*, 245.

[34] T. S. Glen, N. W. Scarratt, H. Yi, A. Iraqi, T. Wang, J. Kingsley, A. R. Buckley, D. G. Lidzey, A. M. Donald, *J. Polym. Sci. Part B Polym. Phys.* **2016**, *54*, 216.

[35] A. Iyer, D. A. A. Trujillo, J. Hack, R. Opila, in *2020 47th IEEE Photovolt. Spec. Conf.*, **2020**, pp. 2786–2789.

[36] S. Sandrez, Z. Molenda, C. Guyot, O. Renault, J. P. Barnes, L. Hirsch, T. Maindron, G. Wantz, *Adv. Electron. Mater.* **2021**, *7*, 1.

[37] P. Mao, Q. Zhou, Z. Jin, H. Li, J. Wang, *ACS Appl. Mater. \& Interfaces* **2016**, *8*, 23837.

[38] C.-Y. Chang, W.-K. Huang, Y.-C. Chang, K.-T. Lee, C.-T. Chen, *J. Mater. Chem. A* **2016**, *4*, 640.

[39] M. Dehghan, A. Behjat, *RSC Adv.* **2019**, *9*, 20917.

[40] C. Liu, C. Xiao, W. Li, *J. Mater. Chem. C* **2021**, *9*, 14093.

[41] F. Pan, C. Sun, Y. Li, D. Tang, Y. Zou, X. Li, S. Bai, X. Wei, M. Lv, X. Chen, others, *Energy \& Environ. Sci.* **2019**, *12*, 3400.

[42] W. Wang, Z. Lin, X. Li, C. Zhang, T. Yang, Y. Liang, *ACS Appl. Mater. \& Interfaces* **2022**, *14*, 18736.

[43] E. Moustafa, M. Méndez, J. Pallarès, L. F. Marsal, *Sol. Energy Mater. Sol. Cells* **2022**, *248*, 111985.

[44] Y. H. Seo, I. H. Cho, S. I. Na, *J. Alloys Compd.* **2019**, *797*, 1018.

[45] J. Cameron, P. J. Skabara, *Mater. Horizons* **2020**, *7*, 1759.

[46] N. K. Elumalai, M. A. Mahmud, D. Wang, A. Uddin, *Energies* **2016**, *9*, DOI 10.3390/en9110861.

[47] N. Hong, X. Qiu, W. Deng, Z. He, Y. Li, *RSC Adv.* **2015**, *5*, 90913.

[48] Z. Molenda, S. Chambon, D. M. Bassani, L. Hirsch, *Eur. J. Inorg. Chem.* **2021**, *2021*, 2533.

[49] Y. Han, J. Wang, C. G. Bischak, S. Kim, K. Lee, D. Shin, M. J. Lee, D. S. Ginger, I. Hwang, *ACS Photonics* **2020**, *7*, 2489.

[50] P. Scherrer, *Kolloidchem. Ein Lehrb.* **1912**, *277*, 387.

[51] A. L. Patterson, *Phys. Rev.* **1939**, *56*, 978.

[52] M. van Eerden, M. Jaysankar, A. Hadipour, T. Merckx, J. J. Schermer, T. Aernouts, J. Poortmans, U. W. Paetzold, *Adv. Opt. Mater.* **2017**, *5*, 1.

[53] Y. Wang, T. Gould, J. F. Dobson, H. Zhang, H. Yang, X. Yao, H. Zhao, *Phys. Chem. Chem. Phys.* **2014**, *16*, 1424.

[54] K. Tanaka, T. Takahashi, T. Ban, T. Kondo, K. Uchida, N. Miura, *Solid State Commun.* **2003**, *127*, 619.

[55] F. Urbach, *Phys. Rev.* **1953**, *92*, 1324.

[56] T. H. Keil, *Phys. Rev.* **1966**, *144*, 582.

[57] S. De Wolf, J. Holovsky, S. J. Moon, P. Löper, B. Niesen, M. Ledinsky, F. J. Haug, J. H. Yum, C. Ballif, *J. Phys. Chem. Lett.* **2014**, *5*, 1035.

[58] S. A. Moyez, S. Roy, *Sol. Energy Mater. Sol. Cells* **2018**, *185*, 145.

[59] G. J. A. H. Wetzelaer, M. Scheepers, A. M. Sempere, C. Momblona, J. Ávila, H. J. Bolink, *Adv. Mater.* **2015**, *27*, 1837.

[60] D. Luo, R. Su, W. Zhang, Q. Gong, R. Zhu, *Nat. Rev. Mater.* **2020**, *5*, 44.

[61] T. Hwang, B. Lee, J. Kim, S. Lee, B. Gil, A. J. Yun, B. Park, *Adv. Mater.* **2018**, *30*, 1.

[62] W. Xu, Y. Gao, W. Ming, F. He, J. Li, X. H. Zhu, F. Kang, J. Li, G. Wei, *Adv. Mater.* **2020**, *32*, 1.

[63] J. Zhang, H. Yu, *J. Mater. Chem. A* **2021**, *9*, 4138.

[64] V. Sarritzu, N. Sestu, D. Marongiu, X. Chang, S. Masi, A. Rizzo, S. Colella, F. Quochi, M. Saba, A. Mura, G. Bongiovanni, *Sci. Rep.* **2017**, *7*, 1.

[65] K. Tvingstedt, O. Malinkiewicz, A. Baumann, C. Deibel, H. J. Snaith, V. Dyakonov, H. J. Bolink, *Sci. Rep.* **2014**, *4*, 1.

[66] X. Cui, G. Chen, X. Han, *J. Chem. Eng. Data* **2006**, *51*, 1860.

# 4. Thin film doping with Cd, Pd, Ru, Sm and Sn

Just as silicon's great success in electronics started from undoped, pristine material, followed by the mastering of the doping process, a similar path seems to await perovskites. So far, however, only undoped materials have been explored to be integrated into perovskite, with only a few attempts of electrically significant doping of perovskites[1–3]. It is believed that this direction is a natural next step for this class of semiconductors. However, due to ionic character of the perovskite crystal, doping by substitution is challenging due to the presence of counter ions that compensate the doping. For these reasons, as presented in Chapter 2, perovskite doping reported so far, took place at grain boundaries, rather than by substitution. In this chapter, some possible dopant ions, that can substitute $Pb^{2+}$ in the perovskite crystal, will be explored.

The potential candidate for a dopant should have an ionic radius close to that of $Pb^{2+}$ in order to conserve the crystal lattice. Too many defects can decrease charge mobility, mitigating the doping effect. Ionic radii of $Cd^{2+}$, $Pd^{2+}$, $Ru^{2+}$, $Sm^{2+}$ and $Sn^{2+}$ are shown in Table 4.1. Additionally, an ion whose oxidation state 2+ is metastable and likely to oxidize to 3+ will release an electron to the conduction band, thus shifting the Fermi level towards the conduction band minimum, resulting in an n-type semiconductor. Analogously, we can expect that a metastable ion that undergoes the reduction to 1+, i.e. a hole is released to the valence band, will shift the Fermi level towards the valence band maximum, resulting in a p-type semiconductor. The scheme of this concept is presented in Figure 4.1. The 2+ metal ions listed above are likely to act as n-type dopants. Exceptionally, $Sn^{2+}$ is rather likely to oxidize to the state 4+ and $Cd^{2+}$ is not likely to change its oxidation state.

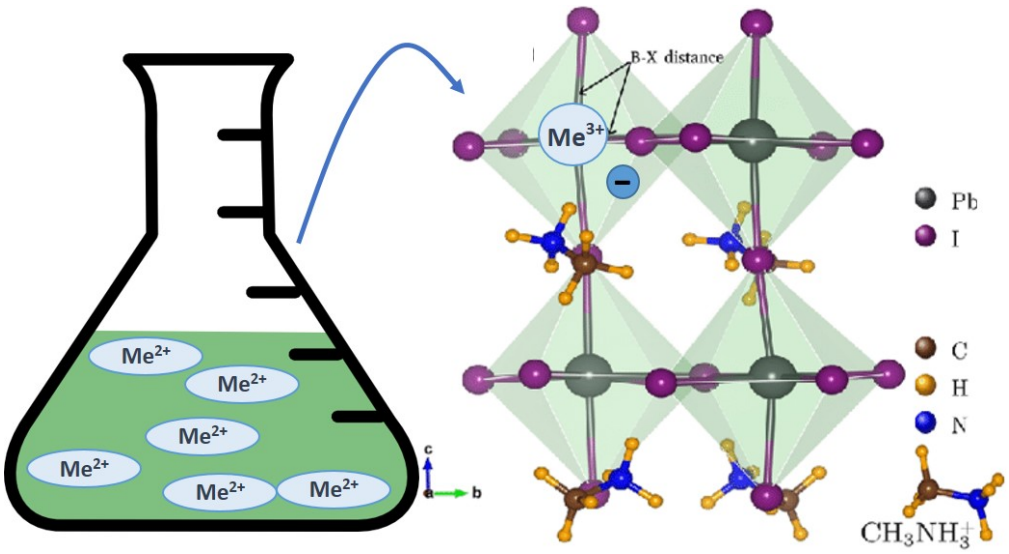


*Figure 4.1. Schematic representation of the doping concept. The perovskite doped with metal ions at the oxidation state 2+ ($Me^{2+}$) oxidizes in the crystal lattice to $Me^{3+}$, releasing a free electron. Analogous process can potentially happen for metals metastable at the oxidation state 2+ and stable at 1+; the reduction from $Me^{2+}$ to $Me^{1+}$ will lead to a release of a free hole.*

*Table 4.1. Ionic radii of dopant candidates at different oxidation states.*

| | **Pb** | **Cd** | **Pd** | **Ru** | **Sm** | **Sn** |
|---|---|---|---|---|---|---|
| **2+** | 1.19 Å [4] | 0.96 Å [5] | 0.86 Å [6] | no data | 1.27 Å [7] | 1.18 Å [8] |
| **3+** | | | 0.76 Å [6] | 0.68 Å [6] | 1.13 Å [7] | 0.69 Å ($Sn^{4+}$) [6] |

To test this concept, the dopants, were introduced directly into a solution of MAPI precursors, in the form of halides. $CdI_2$ is a white hygroscopic solid used in lithography, photography, electroplating and the manufacturing of phosphors. $PdCl_2$ is mostly used as a starting material in palladium-based catalysis in the organic synthesis. It is synthesized by the reaction of palladium and chlorine at high temperatures. Dichlorotetrakis(dimethyl sulfoxide) ruthenium(II) $RuCl_2(DMSO)_4$ was identified in 1983 to be a potential treatment for cancer[9]. Continuous research[10,11] has led to the development of certain DMSO and Ru-containing drugs, some of them reaching the stage of clinical tests. Typically, $SmI_2$ is used as single electron transfer reagents in organic chemistry due to its ability to reduce organic compounds[12]. As $Sm^{3+}$ is more stable than $Sm^{2+}$, $SmI_2$ is obtained by electrochemical reduction of samarium triiodide[6] applying a potential of -2V. $SnI_2$ almost solely serves as a precursor in lead-free perovskites.

## 4.1 One step doping

The perovskite precursors with dopant salts were spin coated onto substrates patterned with gold electrodes, resulting in a layer around 270 nm thick. For the investigation of the doping impact on the electrical properties, the increase of conductivity is a first indication. Even though doping is expected to increase the conductivity, this doesn't prove doping, as conductivity combines the effect of both the charge carrier density and their mobility. Conductivity measurements were made by the two probe technique on lateral geometry in order to avoid any artefact due to possible shortcuts in vertical geometry. The conductivity of the MAPI films, doped with 10 mol% of different dopants was measured. The results in Figure 4.2 show the conductivity increase for Cd (up to 2-fold), for Pd (around 5-fold) and for Sm (up to 4.5 times increase). For Ru- and Sn-doped MAPI rather insignificant impact was observed.

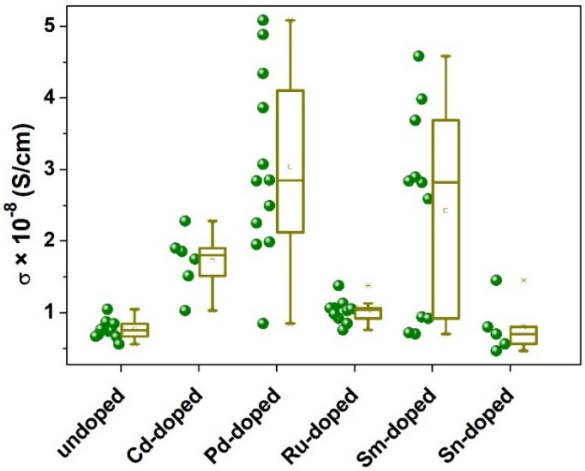


*Figure 4.2. Conductivity of the undoped MAPI film and doped with five different dopants.*

The conductivity increase observed for the addition of $Pd^{2+}$ and $Sm^{2+}$ lead to a more thorough investigation of these 2 dopants by varying their concentration in the perovskite solution. Therefore, doping concentrations from 0.01 to 5 mol% were explored and the results are shown in Figure 4.3. As one can see, a maximum of 8-fold increase of the conductivity was observed for the 1% addition of $Pd^{2+}$ and up to 10-fold increase for 2% of $Sm^{2+}$. In both cases the standard deviation is of the same order of magnitude as the conductivity increase, nonetheless, an at least 2-fold increase was observed for all the samples of the batches composed of 12 samples each. The same minimum 2-fold increase was noted for 2% of $Pd^{2+}$ and 5% of $Sm^{2+}$.

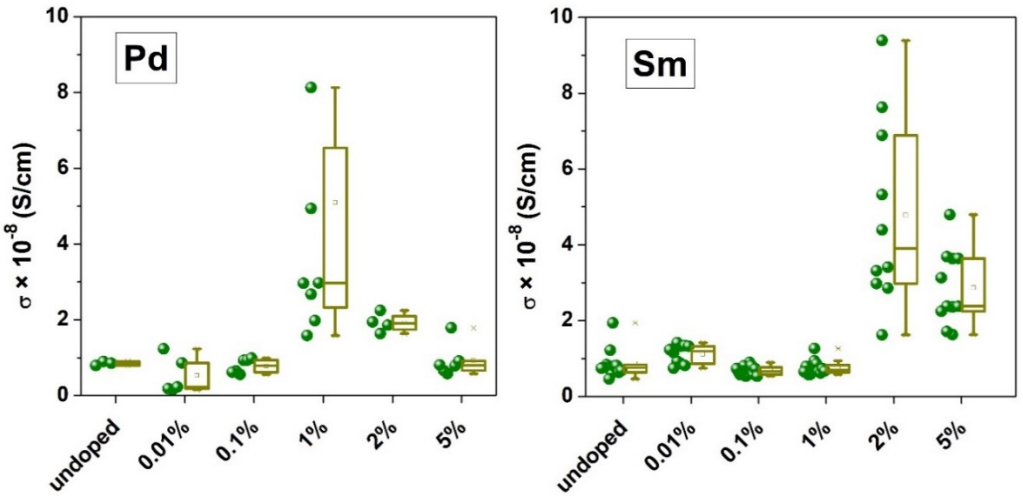


*Figure 4.3. Conductivity of MAPI thin films doped with $Pd^{2+}$ (left) and $Sm^{2+}$ (right) as a function of the dopant concentration.*

In order to investigate the activation energies of the most conductive samples, i.e. 1% $Pd^{2+}$ and 2% $Sm^{2+}$ doped MAPI thin films, a study of the temperature dependence of the conductivity was performed. The activation energy $E_a$ can be determined from the dependence of the conductivity on the temperature, as:

$$\sigma = \sigma_0 exp\left(\frac{-E_a}{k_B T}\right) \tag{4.1}$$

where $k_B$ is the Boltzmann constant, equal to 8.617 × $10^{-5}$ eV $K^{-1}$ and $\sigma_0$ is the pre-exponential constant[13].

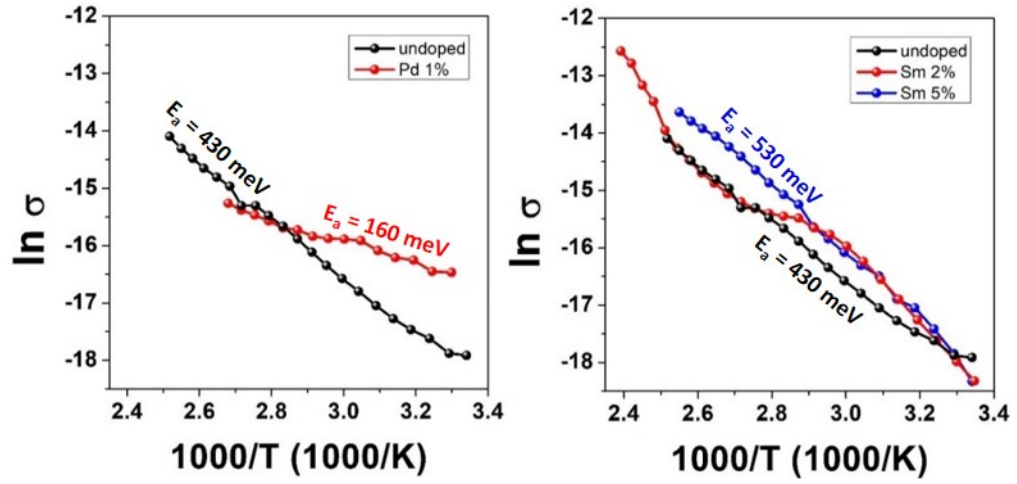


*Figure 4.4. Arrhenius plots of the conductivity as a function of temperature for the $Pd^{2+}$ and $Sm^{2+}$-doped MAPI films at T>RT.*

The slope of the Arrhenius plot of the conductivity versus temperature provides the activation energy. In Figure 4.4, these plots are shown for the undoped, 1% $Pd^{2+}$ doped and 2 and 5% $Sm^{2+}$-doped MAPI thin films. Lack of apparent tetragonal to cubic phase transition at around 340 K may be due to insufficiently small temperature range[14–16]. As one can see, the $E_a$ of the undoped MAPI film is 430 meV, while for the 1% $Pd^{2+}$-doping the activation energy decreases to only 160 meV. However, considering a minimal impact on the conductivity, it is possible that either only a small amount of dopant is activated, or that the mobility of the additional charge carrier is significantly decreased, perhaps by the defects in the crystal lattice, as a result of the introduction of the dopant. The deterioration of the perovskite layer crystallinity upon Sm-doping is shown by the XRD pattern in Figure 4.5a, while the diffraction pattern typical for tetragonal MAPI is conserved. A 4-fold decrease of the diffraction peak intensity is observed upon doping and a Scherrer equation analysis (Equation 3.2) suggests a decrease of the crystalline domain from 72 nm for the undoped MAPI to 58 nm for the MAPI doped with 1mol% Sm. It is noteworthy that no phase separation is observed upon doping, as the diffraction peaks at the same positions are observed for both doped and undoped material, with minimal phase separation of $PbI_2$ and MAI, marked by asterisk and caret in Figure 4.5b. For the $Sm^{2+}$-doping, the $E_a$ increases to 530 meV for 5% doping concentration. For 2%, the plot is not linear over the whole measurement range and there is no clear effect on the transport mechanism resulting from the introduction of samarium ions in to the material. Despite the large dispersion of the results, introduction of $Pd^{2+}$ or $Sm^{2+}$ seem to have an impact on the conductivity. Nevertheless, no clear conclusion can be drawn from these preliminary results.

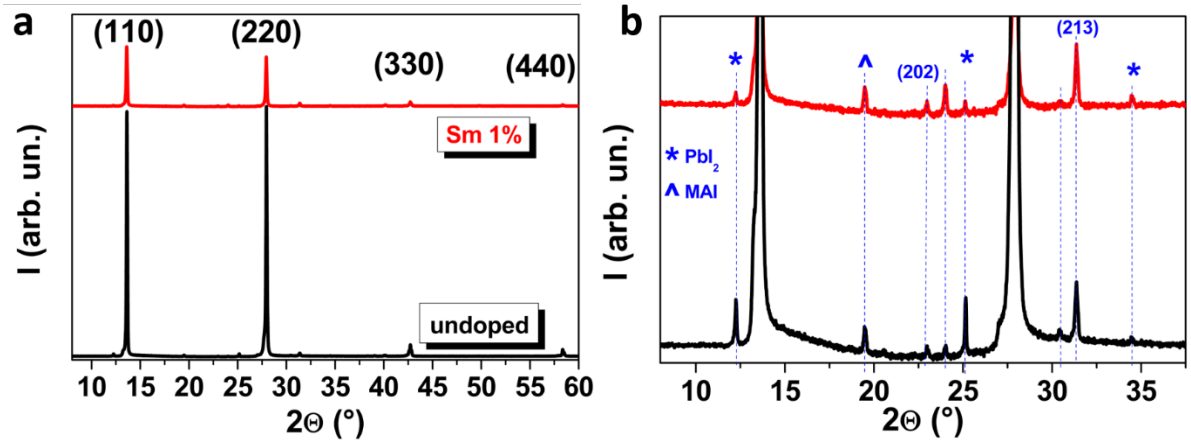


*Figure 4.5. a) XRD pattern of the undoped MAPI and doped with 1mol% Sm; b) zoom-in.*

The samarium-doped MAPI turned out to be the most promising candidate due to the observed conductivity increase as well as the reproducibility of the results. In the following part of this chapter, $Sm^{2+}$ is thoroughly investigated, while other potential dopants are planned to be explored in the future.

Halide perovskites have clearly more ionic character than covalent crystals. Using numerical simulations, Yin *et al*.[17] have shown that defects with low formation energies create only shallow traps, whereas defects with deep levels require high formation energies. On one hand this is an advantage for perovskite devices, as it is facile to fabricate relatively pure material and obtain high efficiencies. On the other hand, it is an obstacle to intentionally dope such a "self-purifying" system: it was shown that single crystal doping from solution is extremely inefficient and only a tiny fraction of the dopant present in the solution finds its place in the final crystal[18]. With it in mind, the doping of thin films remains a challenge: since only a fraction of the dopant from the solution contributes to build the crystal, where does the rest of the dopant go? Indeed, most of the work on doping perovskite thin films reported this far demonstrates that the dopant resides mostly on the surface or at grain boundaries[2,19].

## 4.2 Two-step doping

Doping directly from solution, presented at the beginning of this chapter, results in a poor enhancement of the conductivity. Such a result can be due to the presence of water in the perovskite precursors that leads to the oxidation of $Sm^{2+}$ to $Sm^{3+}$ prior to the perovskite formation. Another reason can be the fact that it is more energetically favorable to form the ionic crystal of MAPI, leaving the dopant precipitate on the grain boundaries or on the film surface. To overcome these challenges, an alternative two-step process is therefore employed. First, the perovskite layer is spin coated and annealed. Second, the $SmI_2$ solution is spin coated on top of the perovskite film and dried to evaporate the rest of the solvent or re-anneal. This way, the $Sm^{2+}$ ions may migrate through the already formed crystal lattice and occupy the energetically favorable positions in the middle of the octahedron of iodine. The $Sm^{2+}$ ions may replace $Pb^{2+}$ at these sites, or fill vacancies. The solvent used for the $SmI_2$ solution is isopropanol (that does not dissolve the perovskite) and DMF in the ratio of 999:1. It is expected that the small addition of DMF weakens the bonds in the crystal thus allowing the dopant to penetrate throughout the layer, instead of remaining on the surface or at grain boundaries. Addition of DMF in the formulation also helps for the wetting of the dopant solution onto the already formed perovskite thin film.

The concept is applied in 5 different ways to optimize the two step approach as shown in Figure 4.6. The doping solution concentration used in all the methods was 10 mg/mL. The efficiency of each method is confirmed by the conductivity measurements (Figure 4.7). Method 1 consists of spin coating and annealing of the perovskite layer, followed by spin coating the $SmI_2$ solution on top of the perovskite film and re-annealing of the stack. Method 2 follows the first three steps from method 1, while the last re-annealing is omitted. Method 3 consists of spin coating the perovskite solution, followed by

spin coating of the $SmI_2$ solution and annealing the whole stack. Methods 4 and 5 consist of spin coating the perovskite solution and adding the $SmI_2$ solution after 60 s or 30 s after the spin coating has begun, respectively. Already in the first batch, the two-step doping strategy was proved to be successful, as for all the doped samples a significant increase of the conductivity was observed. Methods 1 and 2 turned out to be more efficient than methods 3, 4 and 5, resulting in a 2 order of magnitude conductivity increase for the methods 1 and 2, with a little bit higher deviation for the method 2, while the increase of the conductivity for the three other methods was only around 5 times. From this result, it is clear that the dopant incorporation must take place when the undoped MAPI is well crystalized, otherwise the situation partially resembles the one when the dopant is added to the solution.

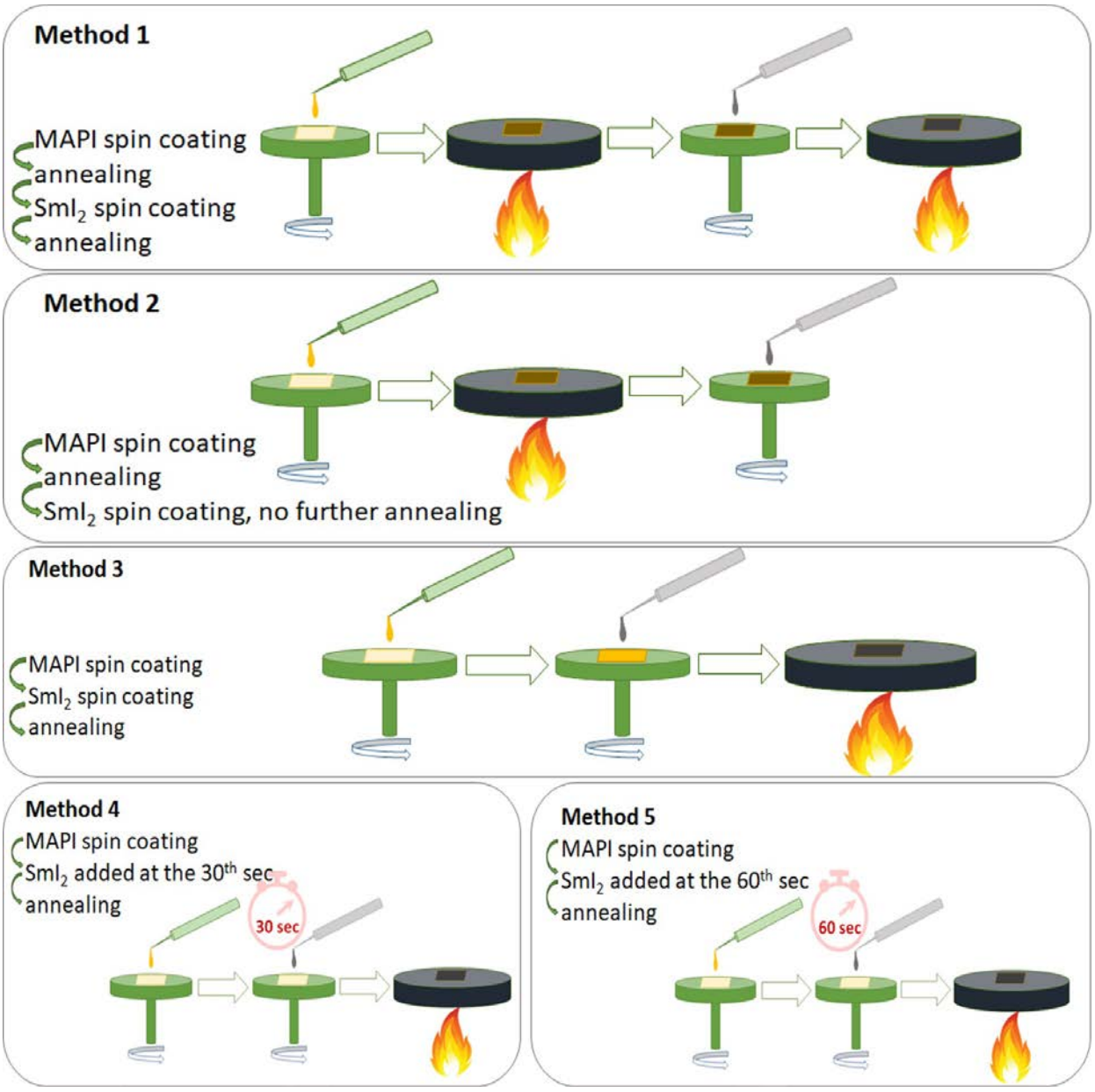


*Figure 4.6. Five different variations of the two-step doping method.*

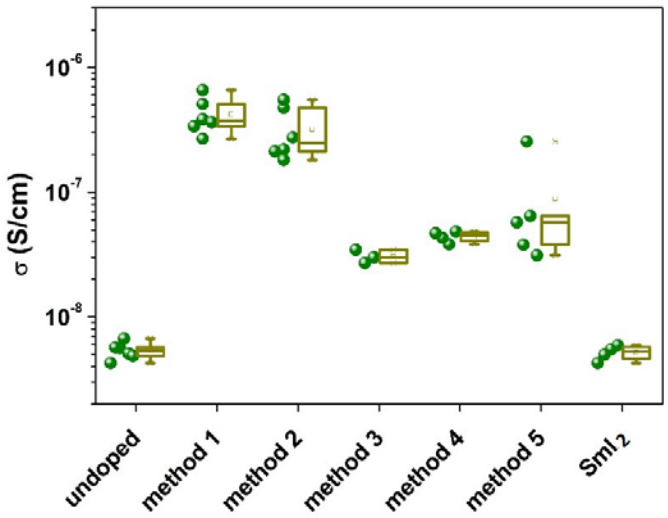


*Figure 4.7. Conductivity of the sto-step Sm-doped MAPI thin films, using 5 different methods.*

**In all the following experiments, method 1 will be applied, unless stated otherwise**. The evidence of the effect of the $SmI_2$ treatment on the conductivity of the perovskite layer as a function of the doping concentration, is shown in Figure 4.8. The doping concentration is shown as the $SmI_2$ concentration in the doping solution. An increase of up to 3 orders of magnitude is achieved with a concentration of 10 mg/mL. It is evident that the conductivity occurs in the perovskite layer and not in the $SmI_2$ layer on the top of perovskite layer, as the conductivity of a bare $SmI_2$ layer is even lower than that of the undoped perovskite layer. This effect is neither due to the solvent, as the sample marked as "0 mg/mL" represents the undoped MAPI treated with the isopropanol and DMF solvent mix without the dopant. For that reason, the increase of conductivity must be due to the combination of the perovskite and $SmI_2$. Similar results were obtained from more than 3 different batches comprising 4-6 identical samples, as shown in Figure 4.9. Notably, for the highest concentrations (15 and 20 mg/mL), the conductivity drops dramatically: around 200 times for 15 mg/mL, comparing to the highest conductivity achieved and down to the level of the undoped sample for 20 mg/mL. This rather unexpected behavior may be due to crystal lattice distortion due to over doping or dopant agglomeration at grain boundaries, effectively blocking the charge carriers.

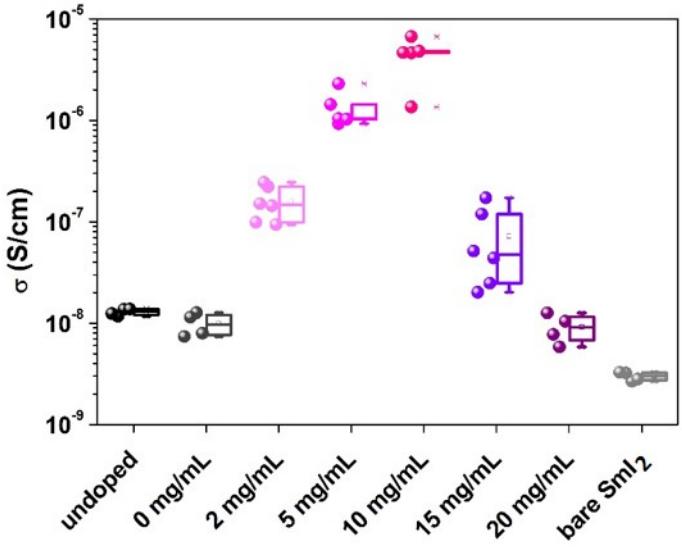


*Figure 4.8. Conductivity as a function of the doping with $SmI_2$. 0 mg/Ll describes the sample treated with the doping solvent only.*

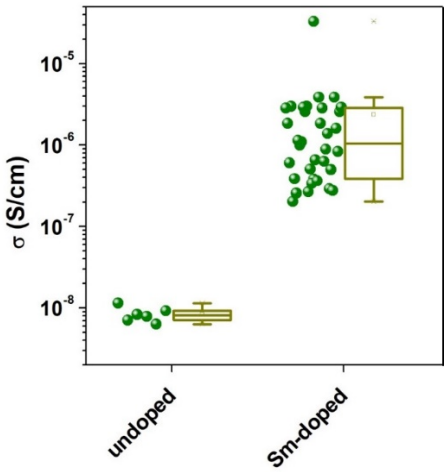


*Figure 4.9. Conductivity of the undoped and Sm-doped MAPI with the use of 10 mg/mL $SmI_2$ solution. Presented results come from 3 different batches.*

In order to confirm that the additional electron resulting from the $Sm^{2+}$ to $Sm^{3+}$ oxidation contributes to the conductivity increase, MAPI was doped with $Sm^{3+}$ and the conductivity was measured. $SmI_3$ was synthesized by dissolving 1 mmol Sm powder in 6 mmol HI (57% aq. solution) and evaporating water and excess iodine under inert atmosphere. The resulting yellow powder was dried under vacuum at RT overnight. The $SmI_3$ solution was prepared in the same way as the one with $SmI_2$ and the same doping procedure was used. Doping solutions of the same molar concentrations as for $SmI_2$ doping were

used, which corresponds to slightly higher mg/mL values. The conductivity as a function of the $SmI_3$ concentration are presented in Figure 4.10. As one can see, no significant conductivity increase was observed over the sampled concentration which demonstrates that it is crucial to introduce the metastable unoxidized $Sm^{2+}$ ions in order to obtain the conductivity enhancement.

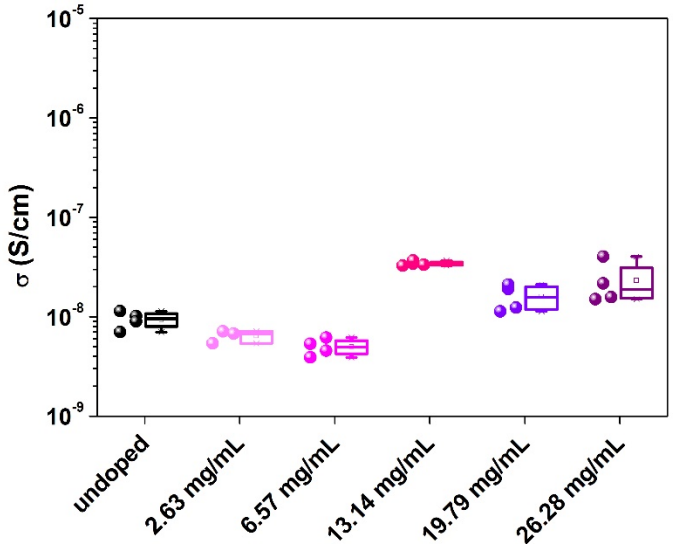


*Figure 4.10. Conductivity as a function of the doping with $SmI_3$.*

The concept of doping described above is expected to work not only for MAPI, but for other perovskites as well. Indeed, formamidinium lead iodide ($FAPbI_3$) and mixed cation $MA_{0.07}FA_{0.93}PbI_3$, doped with $Sm^{2+}$, using the same procedure as for MAPI demonstrated increased conductivity by up to 2 and 2.5 orders of magnitude, respectively (Figure 4.11). This approach, however, did not work for methylammonium lead bromide ($MAPbBr_3$) (Figure 4.12), probably due to its higher conduction band bottom position (between -3.1 and -3.6 eV)[20,21] inducing higher dopant activation energy. The same measurement at higher temperature may therefore result in the observation of the conductivity increase. Possibly, the halide mismatch may play a role: using $SmBr_2$ instead of $SmI_2$ as the dopant precursor would be necessary to confirm this.

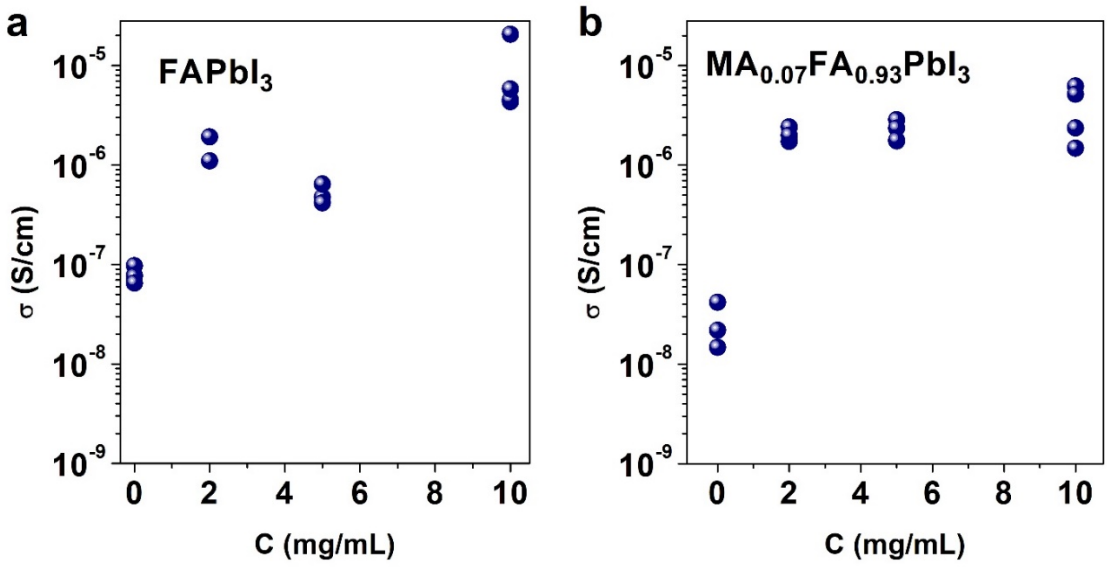


*Figure 4.11. Conductivity of Sm-doped $FAPbI_3$ and $MA_{0.07}FA_{0.93}PbI_3$ as a function of the doping concentration.*

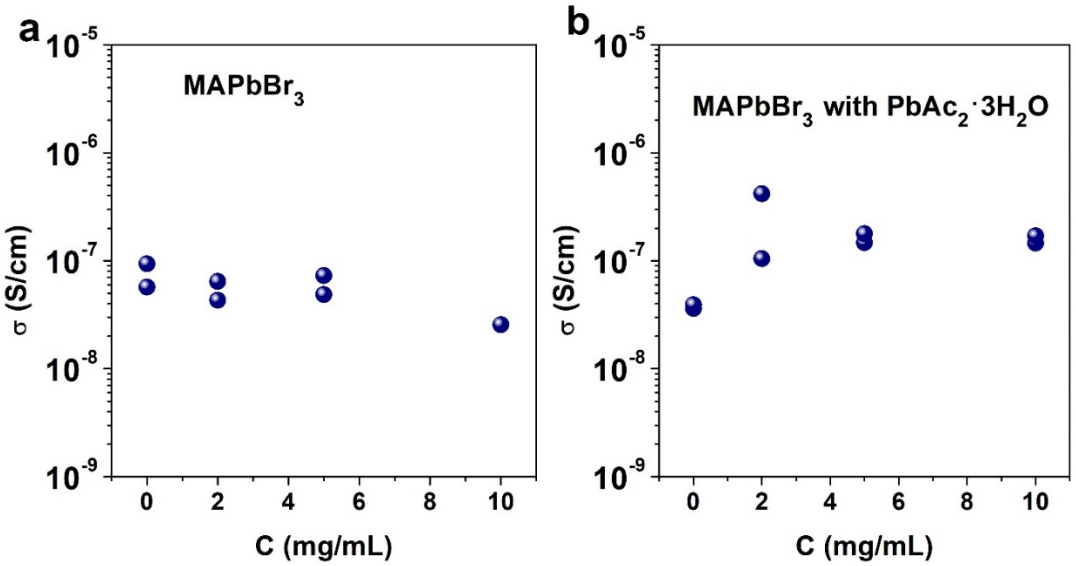


*Figure 4.12. Conductivity of Sm-doped $MAPbBr_3$ as a function of the doping concentration. Left: $MAPbBr_3$ synthesized from MABr and $PbBr_2$, right: $MAPbBr_3$ synthesized from MABr and $PbAc_2 \cdot 3H_2O$.*

Considering that the idea behind the doping method is correct, spin coating must not necessarily be used and a simple well-controlled drop casting should give a similar result. Three different concentrations of the $SmI_2$ solution (2, 5, and 10 mg/mL) were drop casted onto the MAPI thin films prepared according to the procedure described before. They were subsequently dried at RT, until the solvent evaporated, and annealed at 100°C. The conductivity in comparison to the samples prepared by

"method 1" (Figure 4.6) is presented in Figure 4.13. Even though the highest conductivity value for the drop casting-based method is somewhat lower than that obtained by the spin coating method, it is likely that adjustment of the doping parameters, notably, concentration, would yield similar conductivity values as for spin coating. Since during the spin coating, most of the deposited solution is discarded, while in case of the drop casting, all of the doping solution remains on the substrate, one would expect that a rather lower $SmI_2$ concentration for the drop casting process would give a similar material to the 10 mg/mL spin coating. Interestingly, the tendency in Figure 4.13 suggests that the concentration even higher than 10 mg/mL would have to be used to reach the highest conductivity achieved via spin coating. This result suggests a different kinetic of doping for these two processes and further studies are needed.

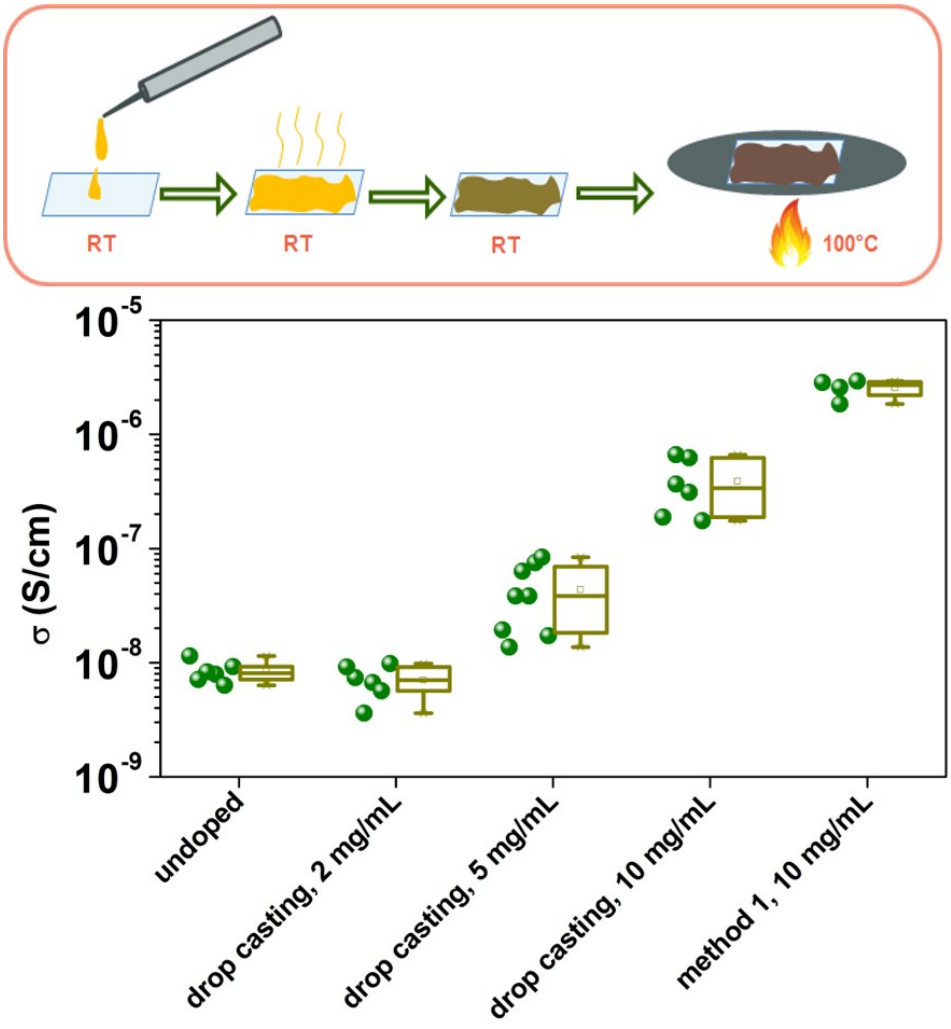


*Figure 4.13. Top: schematic representation of the drop casting based doping of the MAPI thin films. Bottom: conductivity of the drop casting doped MAPI films in comparison with the undoped and doped with spin coating ("method 1").*

## 4.3 Investigation of the doping mechanism

In the following studies, the focus is put on the $Sm^{2+}$-doped MAPI, obtained using "method 1", i.e. post-annealing spin coating-based doping, followed by the additional annealing of the doped sample. In order to explain the physical origin of the conductivity enhancement, the following analysis were performed:

- determination of the $Sm^{2+}$ and $Sm^{3+}$ presence in the perovskite layer,
- surface and bulk dopant distribution,
- doping impact on the surface morphology and crystal structure
- doping type (n or p)
- charge carrier density

### 4.3.1 Valence of samarium ions and their incorporation into the perovskite film

Samarium (2+) was selected as a dopant because its oxidation is expected to release an electron to the conduction band. In order to determine the presence of the $Sm^{2+}$ and $Sm^{3+}$ ions in the doped perovskite and $SmI_2$ reference films, X-ray photoemission spectroscopy (XPS) analysis was performed, since each valence has a specific signature[22,23].

As reference for the doping solution, a spin coated solution of $SmI_2$ was used (the layer was not annealed). The XPS spectra were recorded while the sample surface was etched with a beam of argon clusters. The depth profile of the $SmI_2$ film is presented in Figure 4.14. The rather unexpected presence of $Sm^{3+}$ in the $SmI_2$ film can be explained by the partial $Sm^{2+}$ oxidation in the solution, owing to the reactivity of $SmI_2$ towards traces of water in the isopropanol solvent. To minimize the risk of sample degradation, the samples were transported under inert atmosphere to the XPS vacuum chamber. A significant amount of $Sm^{2+}$ ions is present only on the surface, while in the bulk only $Sm^{3+}$ ions were detected. This may suggest that the argon clusters used for the surface etching induce the $Sm^{2+}$ oxidation. Therefore, in further analysis, only the surface spectrum is considered.

From the depth-resolved spectral evolution for perovskite films doped with 2, 5 and 10 mg/mL of $SmI_2$ (Figure 4.15) it is evident that samarium ions are present throughout the layer for all the doping concentrations. Additionally, in the bulk of the layer one can notice small signals corresponding to $Sm^{2+}$, suggesting that some part of $Sm^{2+}$ remains unoxydized, while in the surface region, there is solely $Sm^{3+}$.

Depth profiles of O 1s (Figure 4.16) reveal the presence of oxygen. On the very surface, it probably comes from $H_2O$ and/or C-O bonding from the solvent or solvent vapors present in the glovebox, that could adsorb to the surface. In the region just below the surface, the O 1s position is characteristic for the Me-O bonding. Combining that with the fact that in this region Sm is at the oxidation state 3+, those peaks may therefore correspond to $Sm_2O_3$. Therefore, the Sm $3d_{5/2}$ spectra in Figure 4.17 come from the layer depth of ~200 nm, as a negligible amount of oxygen can be found there, so we can rule out that the Sm spectra come from $Sm_2O_3$. Most of the $Sm^{2+}$ present in the reference $SmI_2$ layer, oxidizes into $Sm^{3+}$ in MAPI, for all the doping concentrations. Additionally, a shift of the peak corresponding to $Sm^{3+}$ in the doped MAPI reveals a different environment of the $Sm^{3+}$ ion, suggesting it might be incorporated into the perovskite crystal structure.

As the sputtering beam reaches the ITO substrate, the Auger electrons from indium are collected as noted in Figure 4.14 and Figure 4.15.

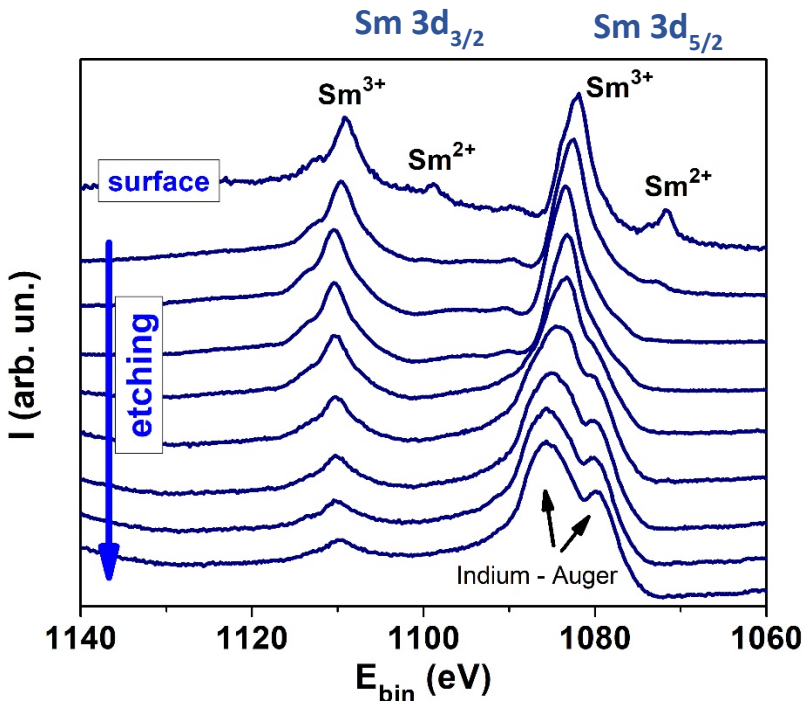


*Figure 4.14. Depth-resolved spectral evolution for the $SmI_2$ spin coated layer.*

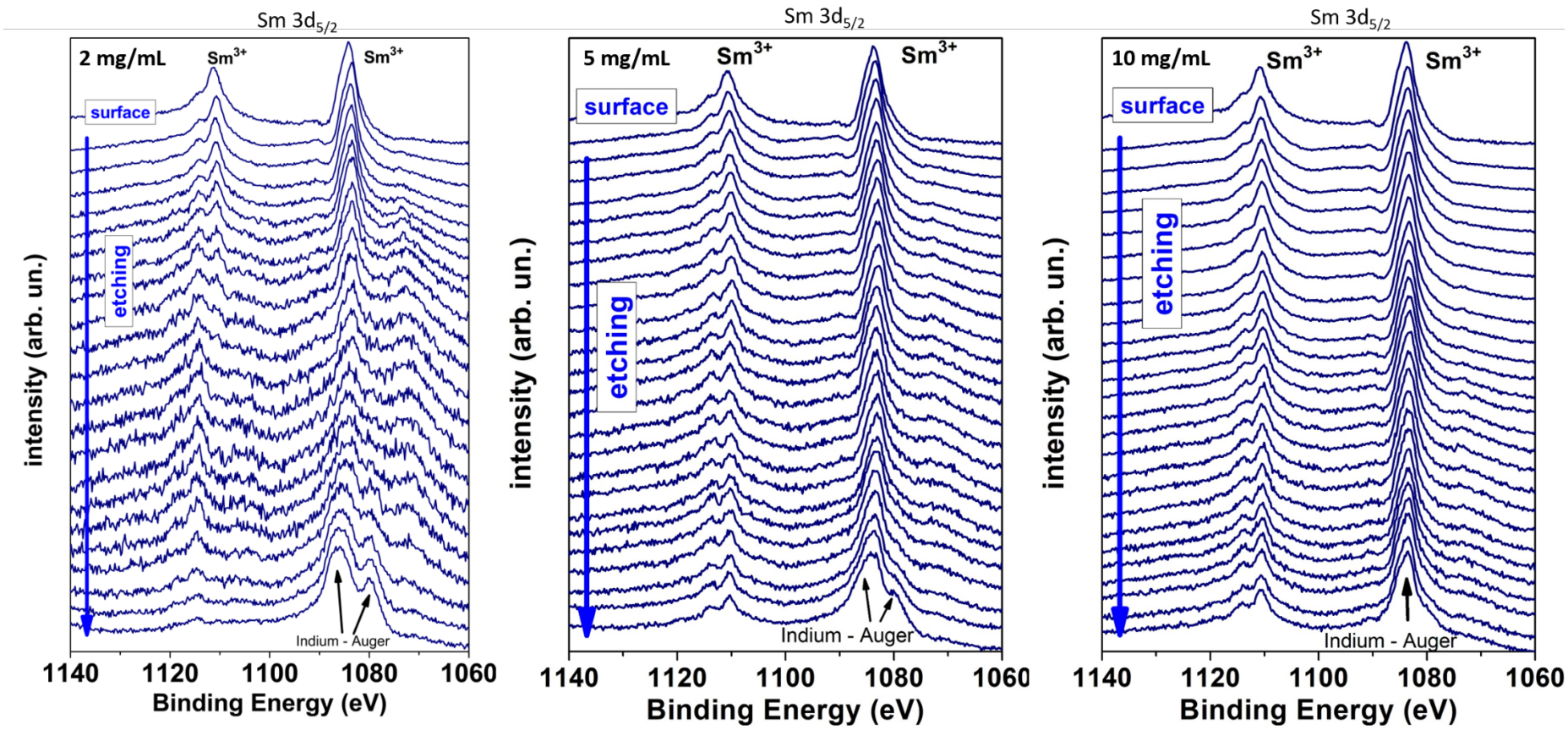


*Figure 4.15. Depth-resolved spectral evolution for MAPI doped with 2, 5 and 10 mg/mL $SmI_2$.*

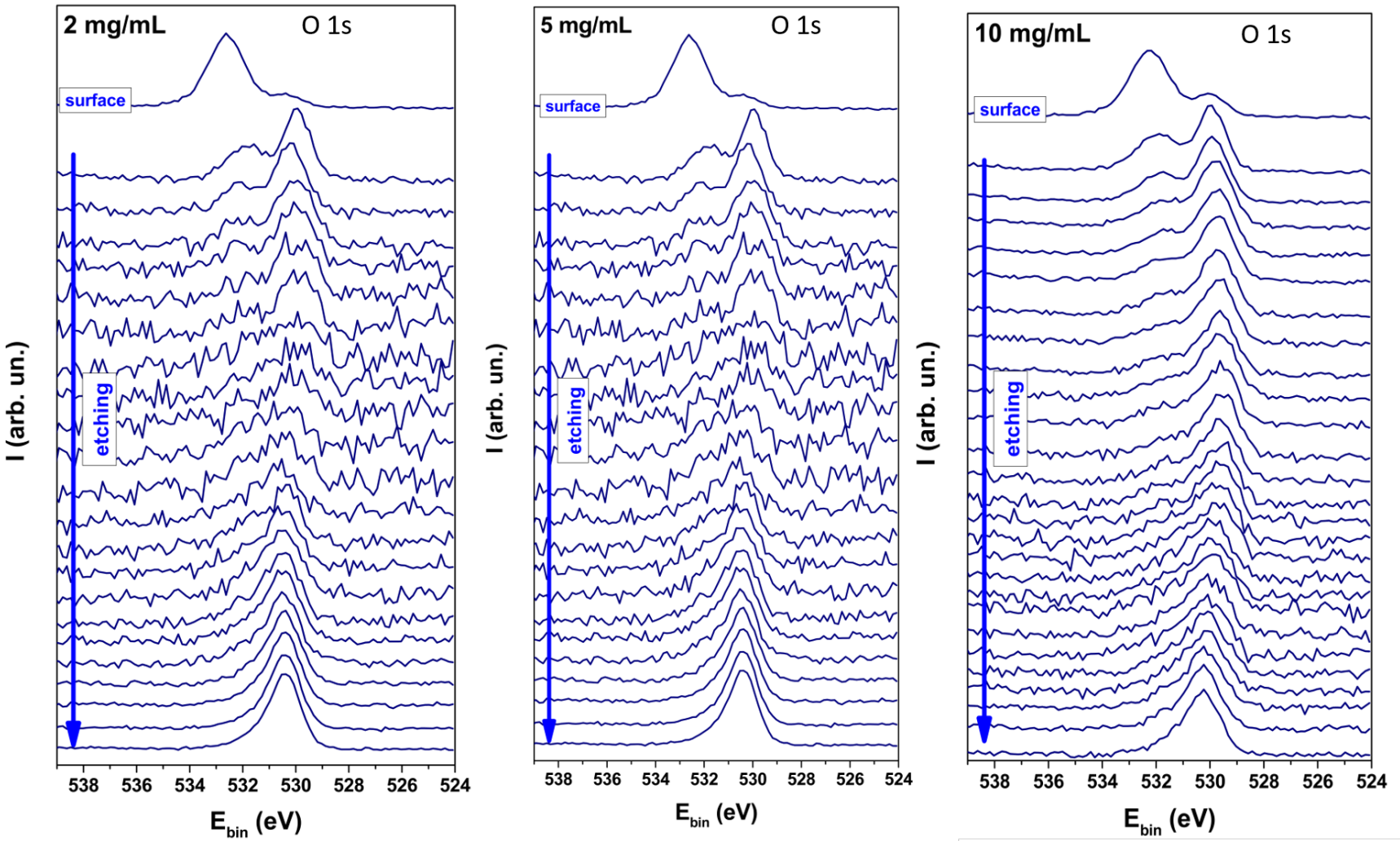


*Figure 4.16. Depth-resolved spectral evolution for MAPI doped with 2, 5 and 10 mg/mL $SmI_2$.*

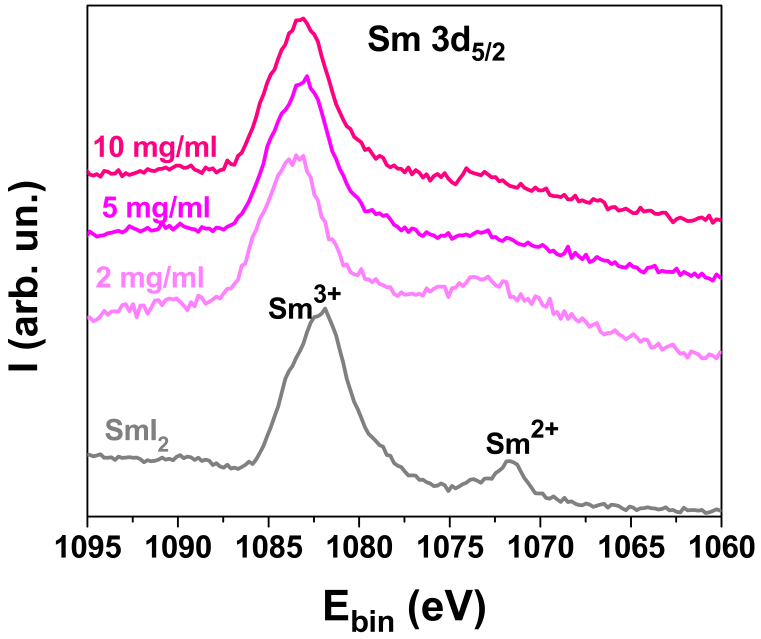


*Figure 4.17. XPS spectra for a thin film of $SmI_2$ and Sm-doped perovskite thin films with different doping concentrations. The spectra are separated on the Y-axis for clarity.*

The integration of the area below the XPS peaks allows to calculate the atomic contribution of $Sm^{3+}$ to the total number of atoms in the sample. In the Figure 4.18a-c the peak integrations for each atom are plotted against the etching time. While it is expected that the $I^-$ and $Pb^{2+}$ concentrations be constant throughout the layer, they appear to be lower on the surface and at the interface with the substrate than in the bulk of the layer. On the surface, the $Pb^{2+}$ and $I^-$ amount is offset by the $Sm^{3+}$ content, as the plots show the atomic % with respect to all the elements (except hydrogen and nitrogen). Close to the interface with the substrate, this effect must be coupled with the gradual, not sharp, rise of the indium and oxygen content, corresponding to the ITO substrate. These artefacts are linked to the energy of the argon clusters used for the etching[24]. The same effect probably takes place for $Sm^{3+}$, but it cannot be observed due to another artefact: the Sm $3d_{5/2}$ spectral line coincides with the Auger lines of In, therefore samarium seems to be even more pronounced below the In cutoff. In fact, it is the signal from Auger electrons from In, interpreted as $Sm^{3+}$. An unexpected increased amount of oxygen on the surface can come from the traces adsorbed to the surface. The oxygen signal parallel to $In^+$ comes from the ITO.

The rise of indium can roughly indicate that the whole sample has been etched and the sputtering beam reached the substrate. The first appearance of the In signal is identified as the sample thickness in Figure 4.18d. The $Sm^{3+}$ content is normalized to the sample thickness and compared between the samples with three different doping concentration as the $Sm^{3+}$: $Pb^{2+}$ atomic ratio. One can see that there is a spike of $Sm^{3+}$ content on the surface followed by a gradual decrease for all three doping concentrations. This is

perfectly justified by the doping method. The concentration of around 90% of $Sm^{3+}$ on the surface can be explained by residual Sm-compounds, presumably $SmI_3$. The concentrations from 20 to 40% of $Sm^{3+}$ close to the interface with the substrate seem to be extremely high, which is a result of an overestimation of the $Sm^{3+}$ content due to the overlapping of the $Sm^{3+}$ -corresponding XPS peak and the peak corresponding to Auger electrons of In. If the $Sm^{3+}$ content is effectively high, it would indicate that the doping is quite inefficient, which will be further developed in the following part of this chapter.

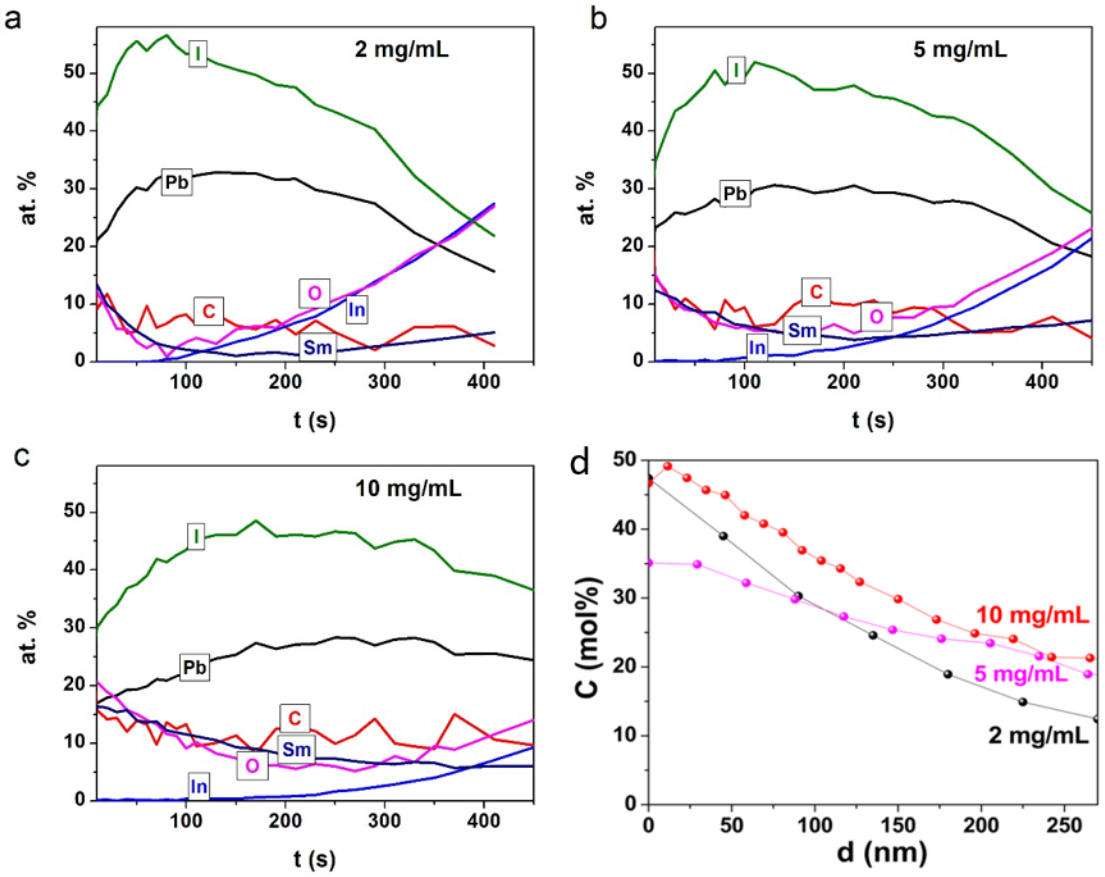


*Figure 4.18. Atomic profiles of MAPI doped with a) 2 mg/mL, b), 5 mg/mL and c) 10 mg/mL $SmI_2$. d) Depth-resolved profile of the $Sm^{3+}$ concentration.*

To confirm the dopant penetration inside the perovskite layer, time of flight secondary ion mass spectroscopy (ToF-SIMS) analysis of the samples was performed. This technique, coupled with ion sputtering on the surface, allows to track the elemental composition throughout the layer. Figure 4.19 shows the depth-resolved profiles of the perovskite layer, either undoped, or treated with the dopant solvent with no dopant, or doped with the $SmI_2$ solution in different concentrations. Similarly to the atomic profiles from integrated XPS peaks in Figure 4.18 and for the same reasons, the signals of $Pb^+$ and

$I^-$ of the ionic perovskite crystal do not fall sharply, and the signal corresponding to the substrate, in this case $In^+$, rises gradually. Similar artefacts were reported previously[25–27]. Another bizarre artefact is the monotonic decrease of the signal coming from the methylammonium ion. This is assigned to the sputtering ions damaging the fragile organic structure, causing what appears to be a decrease in the methylammonium content[28].

In order to compare different $Sm^{3+}$ content for the samples doped with different $SmI_2$ concentrations, the Sm-corresponding ToF-SIMS depth profiles are plotted in Figure 4.20. As one can see, the signal intensity corresponding to $Sm^{3+}$ is increased for all the samples in the area close to the surface. Effectively, taking into consideration the doping method, it is expected that a significant amount of the dopant remains on the surface. Similar features are present on the XPS profiles. Interestingly though, the signal corresponding to $Sm^{3+}$ is detected throughout the layer, until the signal from the ITO substrate is detected (rise of $In^+$). Contrarily to the XPS profile, the dopant content stabilizes below the surface and it is constant until the substrate interface, with the exception of the samples doped with 2 and 5 mg/mL, where a monotonous decrease is observed. Consequently, based on these XPS and ToF-SIMS experimental results, it is unclear whether the doping concentration stabilizes at some point under the surface or it decreases gradually throughout the layer. However, considering that in order for the doping concentration to be constant, the perovskite would have to (in a way) saturate with the dopant, it is highly unlikely that there can be different levels of doping saturation, i.e. the maximum amount of dopant that perovskite can accept, them being on different levels for each sample. Therefore, it is concluded that the XPS profile is more realistic in this matter. Nevertheless, the intensity of the signal corresponding to $Sm^{3+}$ increases along the increase of $SmI_2$ concentration in the doping solution.

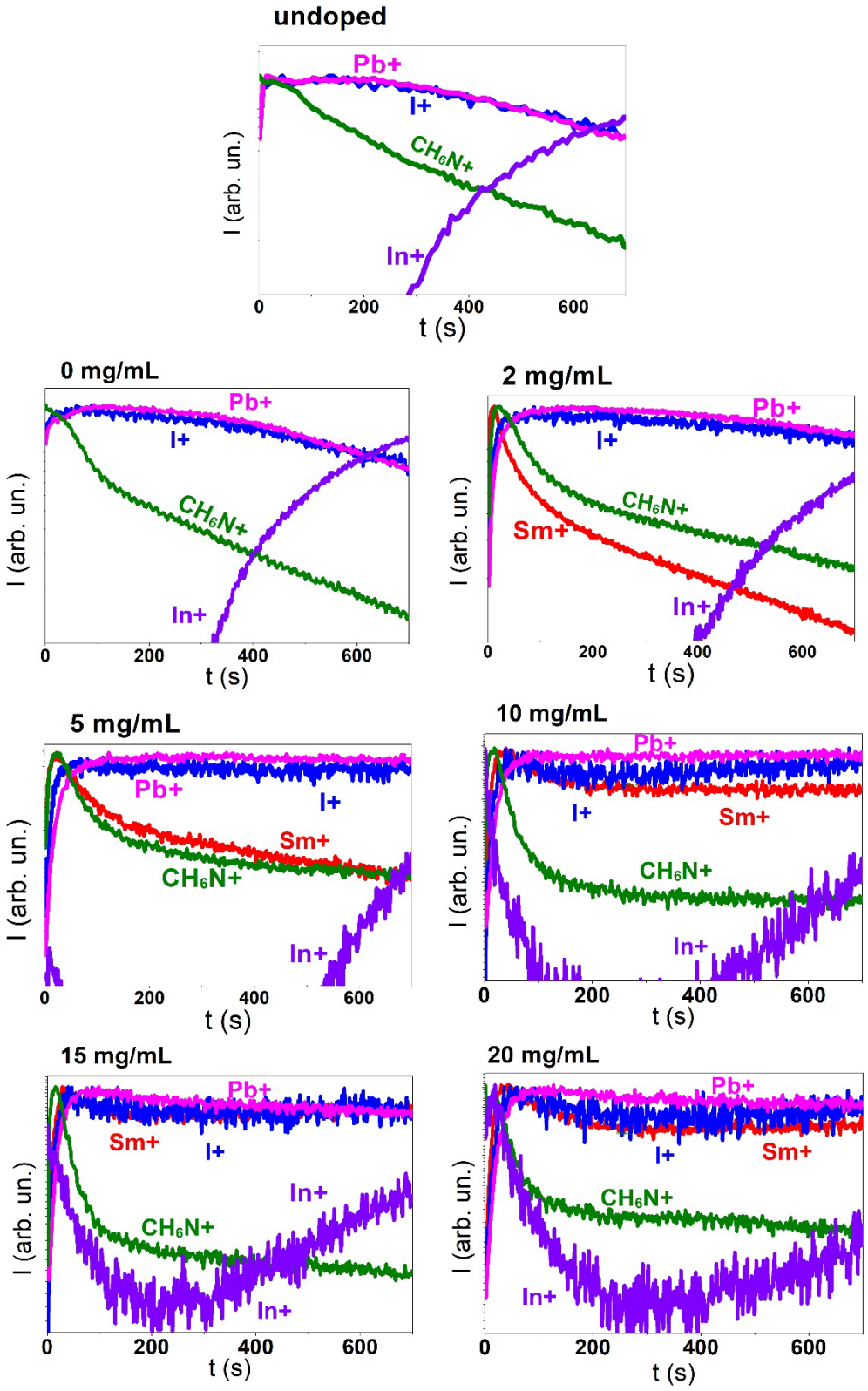


*Figure 4.19. ToF-SIMS spectra with the in-depth profiles for the undoped MAPI, MAPI treated with the solution used for the dopant and five different doping concentrations. The Y-axis in in a semi-log scale.*

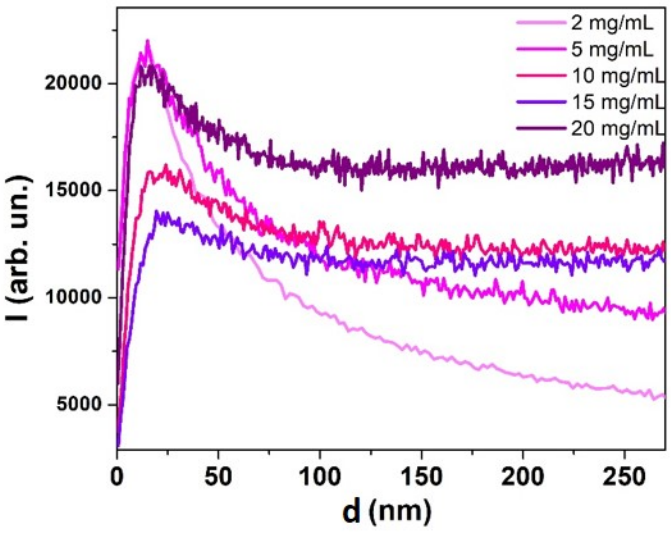


*Figure 4.20. ToF-SIMS Sm depth-resolved profiles for different concentrations of $SmI_2$ used for the doping of MAPI thin films.*

## 4.3.2. Surface morphology

The depth-resolved profiles of ToF-SIMS and XPS both show an increased content of Sm on the surface for the samples doped with all the $SmI_2$ concentrations. In these circumstances, the surface morphology can provide more insightful information about the surface properties. As shown in Figure 4.21, the surface topology imaged by AFM and scanning electron mictroscopy (SEM) of the 10 mg/mL doped sample shows significantly different morphology than those of the undoped sample and only for these samples the SEM images were acquired in combination to their AFM counterparts. For the other doping concentrations, only AFM images were made, as it is evident that the surface is changed for all of them. While on the surface of the undoped perovskite film grain sizes of 100-500 nm are clearly seen, the doped layer is covered with the oval-like grains of a much smaller size: between 50 and 100 nm. Presumably, the small grains on the surface of the doped sample correspond to the residual Sm compounds on the surface, resulting from the doping method. Notably, the topology of the sample treated only with the dopant solvent ("0 mg/mL") is unaltered compared to undoped MAPI, which proves again that the solvent treatment does not impact the perovskite grain morphology.

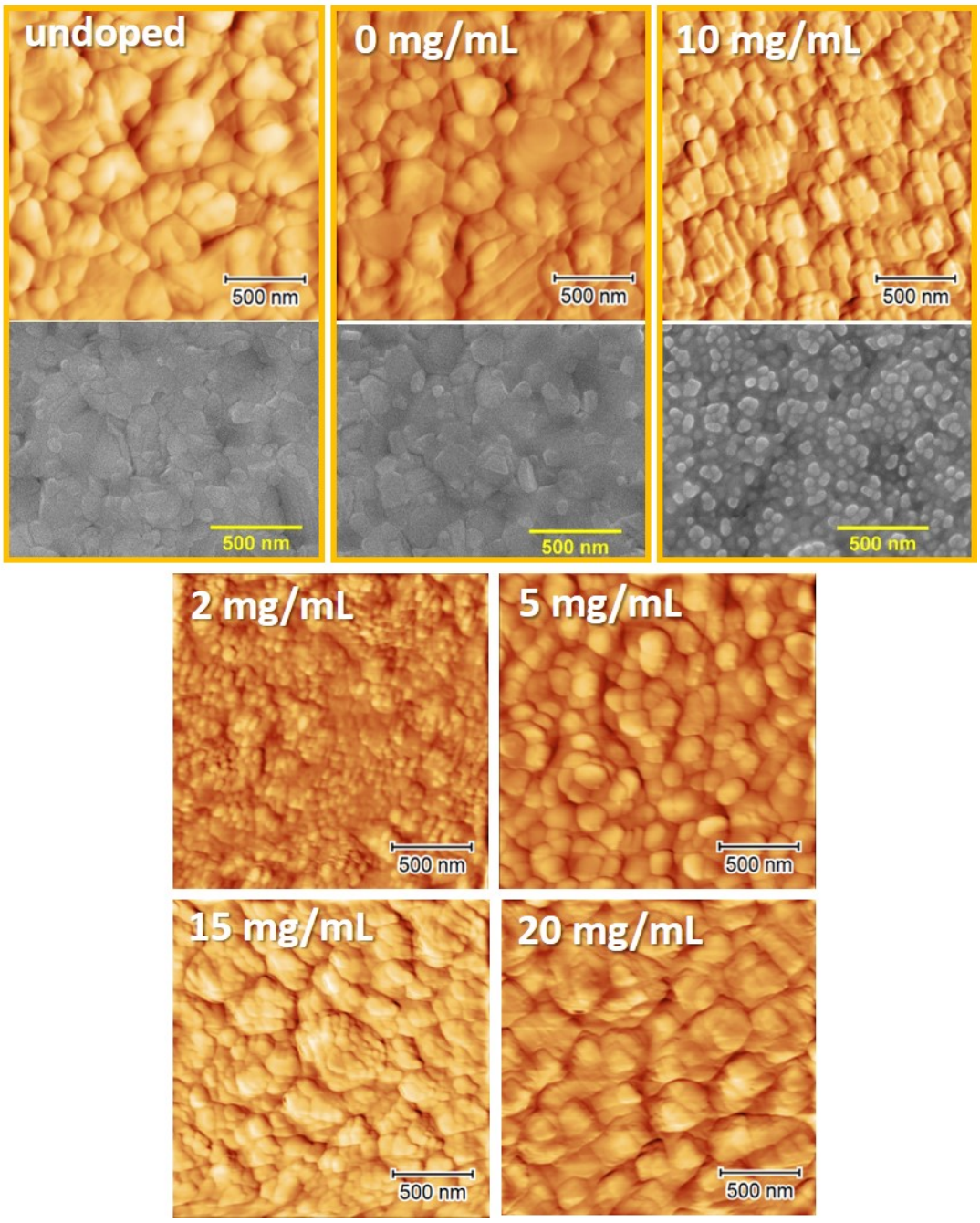


*Figure 4.21. AFM and SEM images of the undoped MAPI, MAPI treated with the solution used for the dopant and five different doping concentrations.*

## 4.3.3. Structural properties

To determine the impact of doping treatment on the crystal structure of the MAPI layer, XRD patterns of the doped and undoped MAPI were collected and are presented in Figure 4.22. The XRD spectra for the undoped sample and those doped with the concentrations 2-20 mg/mL exhibit a diffraction

pattern, that is characteristic for tetragonal MAPI[29], with the diffraction peaks at 13.6°, 27.8°, 31.3°, 42.6° and 58.3°, that correspond to (110), (220), (213), (330) and (440) Miller planes, respectively. Small peaks corresponding to $PbI_2$ at 12° and 25° are also present, as it is not uncommon to find small amounts of $PbI_2$ in MAPI thin films[30]. The same positions of the principal diffraction peaks indicate that the crystal structure of the perovskite remains unchanged upon doping. A decrease in the peak intensity with the increase of the doping concertation suggests however that the incorporation of dopant renders the polycrystalline layers more defective. For the highest doping concentration (20 mg/mL) two more peaks are present, at 10.5° and 16.0° (marked by asterisks), that do not appear for other doping concentrations. They are presumed to originate from the phase separation of the $SmI_3$. This might be the reason for the decreased conductivity observed at high doping concentration, as the inclusion of an insulating phase in the perovskite layer leads to a charge mobility decrease.

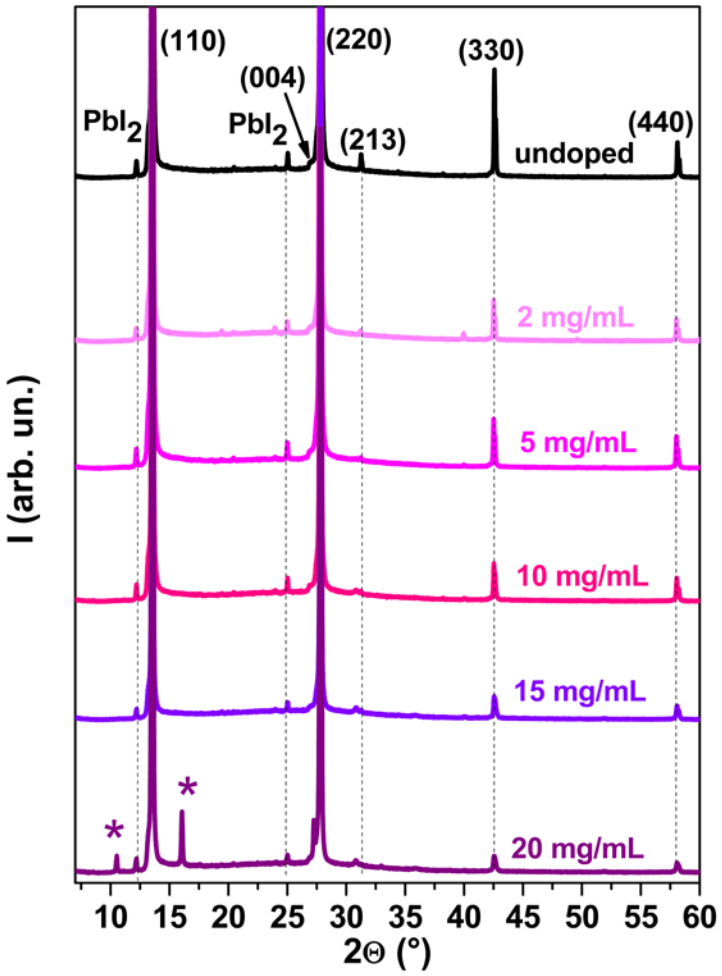


*Figure 4.22. XRD patterns of the undoped and doped MAPI at different doping concentrations.*

## 4.3.4. Optical properties

The UV-visible absorption spectra for the doping concentrations 2-20 mg/mL, together with the undoped MAPI and with MAPI treated with the dopant solvent are presented in Figure 4.21. The absorption edge at 765 nm, typical for undoped MAPI, is present also for all the doping concentrations. The Tauc plot in the inset was plotted without the baseline and normalized in order to demonstrate that the bandgap of the samples does not change upon doping, and that it is the same as for the undoped MAPI (1.62 eV). This can exclude the increase of the conductivity being due to additional energy bands within the bandgap.

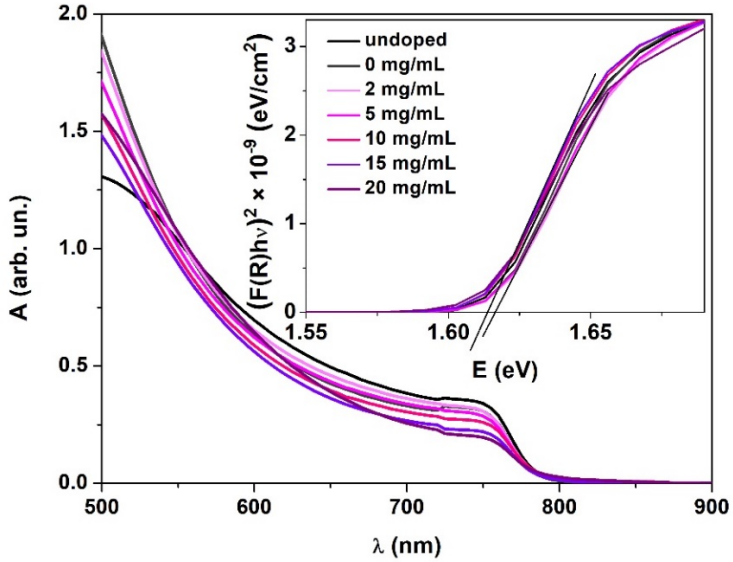


*Figure 4.23. Absorption spectra in the visible region of the undoped and doped MAPI at different concentrations. Tauc plot shown in the inset.*

In agreement with a bandgap of 1.62 eV (corresponding to 765 nm), the photoluminescence peak occurs at 780 nm (Figure 4.24), which is in the proximity to this value, with a small Stokes shift of 0.03 eV. For doping concentrations of 2-20 mg/mL, one can observe the total quenching of the PL signal (Figure 4.24a). Probing the concentrations lower than 2 mg/mL (Figure 4.24b), an image of a partial quenching emerges for the concentrations from 0.5 and 1 mg/mL. For the lowest doping concentrations, namely 0.05 and 0.1 mg/mL, a slight increase in the PL intensity is observed instead. There are two possible explanations of this phenomenon:

- Since the trap density in the undoped MAPI was reported to be ≈$10^{16}$ $cm^{-3}$ [31], it is possible that a small amount of doping fills the traps that act as non-radiative recombination centers, thus increasing the PL compared to the undoped perovskite.

- If the undoped MAPI layer on ITO behaves like slightly p-doped semiconductor, small amounts of n-type dopant would shift the Fermi level closer to the middle of the bandgap, resulting in the increase of PL intensity.

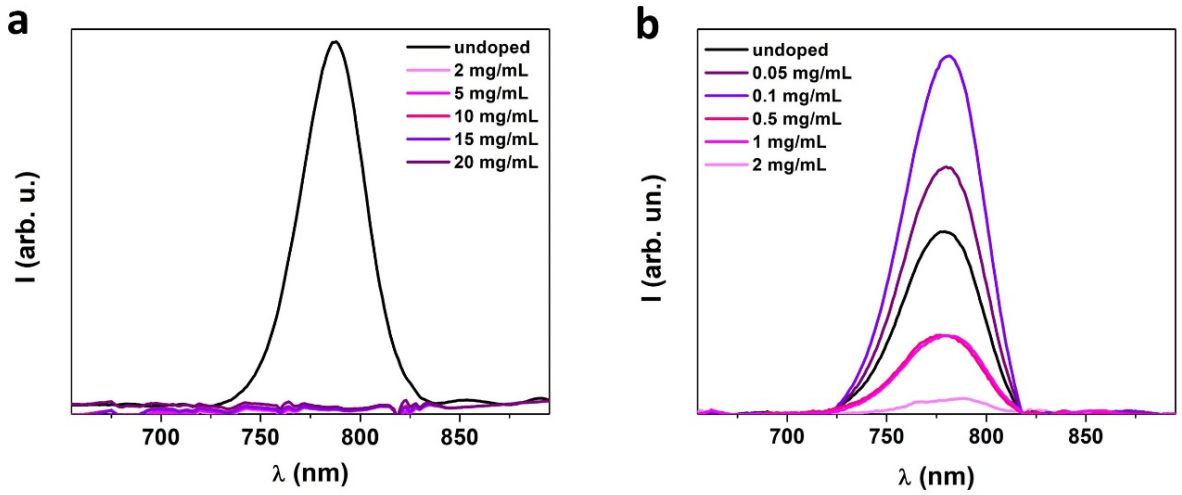


*Figure 4.24. PL of the undoped and doped MAPI at different $SmI_2$ concentrations: a) 2-20 mg/mL and b) 0.05-2 mg/mL.*

## 4.3.5. Semiconductor type

The n or p semiconductor type is crucial in characterizing the effect of doping on the electrical properties since it directly impacts the position of the Fermi level in the bandgap of the semiconductor. In the simplest case the Fermi level position would be inferred from the work function (*WF*). In reality, work function depends not only on the energy of the Fermi level, but also on the surface dipole and on the substrate on which the thin film is deposited. Surface dipole can originate from the dangling bonds on the crystalline surface, altered surface composition (most likely oxides, after reacting with the oxygen from the atmosphere) or from the adsorbed molecules from the air, e.g. $H_2O$, $O_2$, $N_2$. The substrate can impact the measured work function of a semiconductor due to the depletion layer created at the metal/semiconductor interface. The depletion layer thickness is the thicker the lower free charge carrier density of the semiconductor. MAPI has a relatively low free charge carrier density, therefore the depletion layer thickness reported for this material is in the range of hundreds of nm, up to microns in some cases. In order to measure the work function, two methods are commonly used: Kelvin probe and UPS.

Work function of the undoped MAPI and doped with the $SmI_2$ solutions of the concentrations 2-20 mg/mL were measured using a Kelvin probe. The freshly cleaved highly oriented pyrolytic graphite (HOPG) with work function of 4.6 eV[33] was used as a reference. The samples were measured in a nitrogen filled glovebox. The *WF* of the undoped MAPI was measured to be 5.5 eV. Considering that the literature value spreads from 3.9 to 5.4 eV[34–36], the value measured here is above the higher limit of the reported range. In spite of the use of the Faraday cage, the electrostatic noise could be responsible for the erroneous tip calibration, as the experiments were performed in the glove box. Moreover, a decrease of 1.4 eV, observed for all the doped samples (Figure 4.25), seems to be quite large, considering that the band gap is 1.63 eV. If the *WF* charge reflects the change of the $E_F$, then the *WF* of the heavily doped samples would be close to the electron affinity, suggesting that the undoped MAPI is strongly p-doped. This would in contradiction with the high PL intensity of the undoped sample, as well as with its low conductivity. One explanation could be connected with a strong dipole on the surface, coming from residual Sm-species, resulting from the doping method and observed on the AFM and SEM images (Figure 4.21), as well as on the XPS and ToF-SIMS depth profiles (Figure 18 and Figure 4.20). Another reason could be the iodine adsorption of the golden tip used for the surface potential difference measurement during the measurement. Such behavior was observed by Zhang *et al.*[37][37]. As MHPs can easily degrade upon light or moisture, one of the product of the degradation can be $I_2$, which can adsorb to the tip surface. This results in the increase of the *WF* of the tip. Consequently, the potential difference between the tip and the measured sample appears to be lower, resulting in the apparent *WF* of the measured sample to be lower than it really is. These two effects could result in the *WF* difference as high as 1.4 eV between the undoped and doped samples.

Nevertheless, it was interesting to measure the samples with doping concentrations below 2 mg/mL. Indeed, for doping concentrations from 0.001 to 0.2 mg/mL an almost linear increase of the work function with the concentration is observed, suggesting a monotonous transition towards the n-type semiconductor for doped samples. While the actual values are burdened with error, the trend of the gradual decrease of the *WF* is consistent with n-doping.

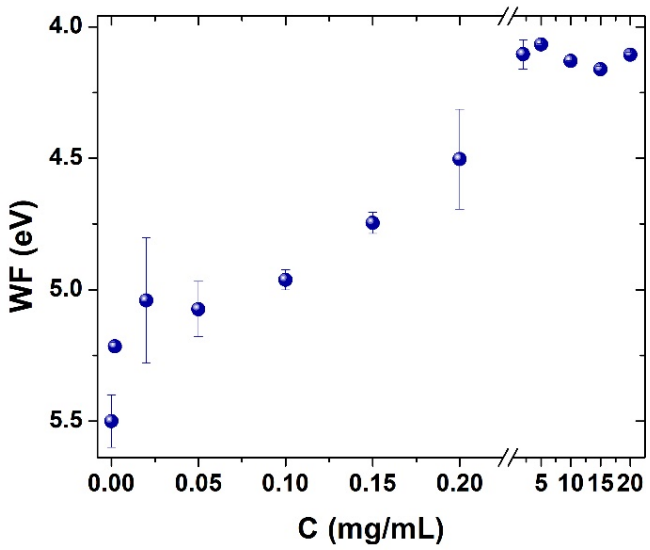


*Figure 4.25. Work function versus doping concentrations, measured using Kelvin probe.*

In order to verify the Kelvin probe-measured *WF* values, UPS measurements were performed on the undoped and doped samples with concentrations ranging from 0.01 to 0.50 mg/mL, together with 2 and 10 mg/mL (Figure 4.26). The kinetic energy cut-off value corresponds to the work function of the material. The WF of the undoped MAPI was determined to be 4.5 eV. The difference between the *WF* determined by KP and UPS can come from a different ambient (nitrogen vs. vacuum), therefore nitrogen or traces of oxygen or water could adsorb to the sample surface, increasing its work function. Additionally, the electrostatic forces in the glovebox could also contribute to the increased *WF* of the samples measured using KP. The samples doped with 2 and 10 mg/mL $SmI_2$ have work functions of 3.8 and 3.7 eV, respectively, which results in the *WF* differences of 0.8 and 0.7 eV between the undoped MAPI and doped with 2 and 10 mg/mL, respectively. Assuming that the shift of the *WF* corresponds to the shift of the $E_F$ and that the Fermi level of the undoped MAPI is close to the middle of the bandgap, the highly doped samples would have to be strongly n-doped, with their Fermi levels just below the conduction band bottom. Such a conclusion would not be in agreement with a relatively low conductivity increase (3 orders of magnitude maximum) and the fact that the lowest doping concentration for which the conductivity increases is 1 mg/mL, while a *WF* decrease by almost 1 eV is observed for a concentration as low as 0.01 mg/mL (Figure 4.27).

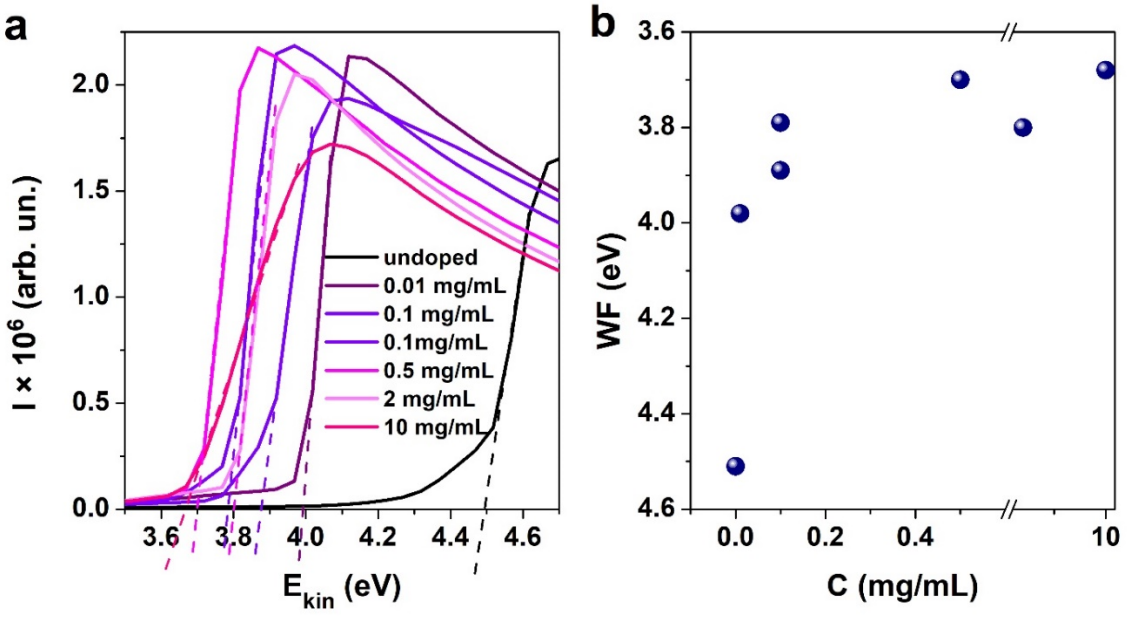


*Figure 4.26. a) cut-off region of the UPS spectra and a) work function versus doping concentrations, determined by UPS.*

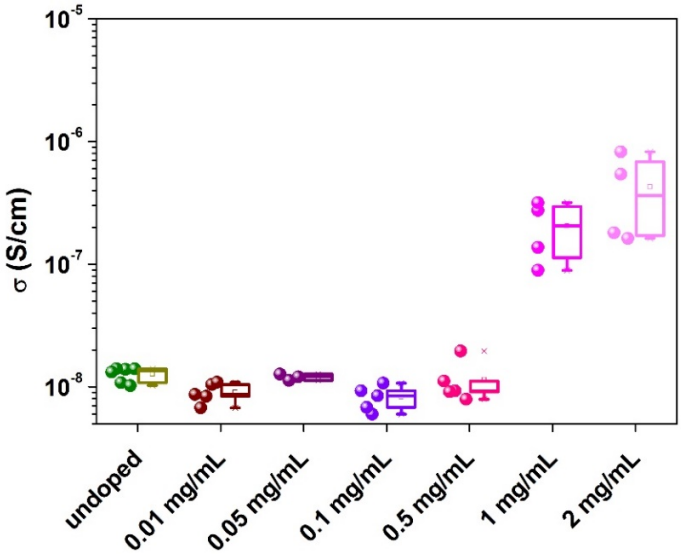


*Figure 4.27. Conductivity for MAPI doped with low $SmI_2$ concentrations.*

*WF* defines the position of the $E_F$ with respect to the vacuum level ($E_{vac}$), which is different for every material and can change due to the presence of surface dipoles. In order to define the position of the $E_F$ in the bandgap, the valence band region of the UPS spectra was also analyzed. Due to the low density of states in the valence band in perovskites, the onset of the valence band in the original dataset is not clear (Figure 4.28), especially for the highly doped samples, while for the undoped MAPI the direct extraction of the onset energy value might lead to erroneous conclusions. As pointed out by Zhang *et*

*al.*[38], the helium lamp used as a source of UV radiation produces not only He I monochromatic line (21.22 eV), but it is also "contaminated" by satellite lines of He $I^{\alpha}$, He $I^{\beta}$ and He $I^{\gamma}$, with respective energies of 23.09 eV, 23.75 eV and 24.05 eV. The contribution of these satellites is not bigger than 2% and it depends on the pressure of the He lamp. Nevertheless, when the density of states is low, like in case of MAPI, even this small degree of non-monochromaticity can be an obstacle in the correct data interpretation. The amount of He $I^{\alpha}$, He $I^{\beta}$ and He $I^{\gamma}$ radiation in this experiment was estimated to be 1.8%, 0.03% and 0.01%, respectively. In the Figure 4.29a. the spectrum acquired for the sample 10 mg/mL is plotted, together with the satellite lines and in Figure 4.29b the result of the subsequent satellite lines removal is presented. In Figure 4.30 the *E w.r.t.* $E_F$ are extracted for each doping concentration, after the satellites have been removed.

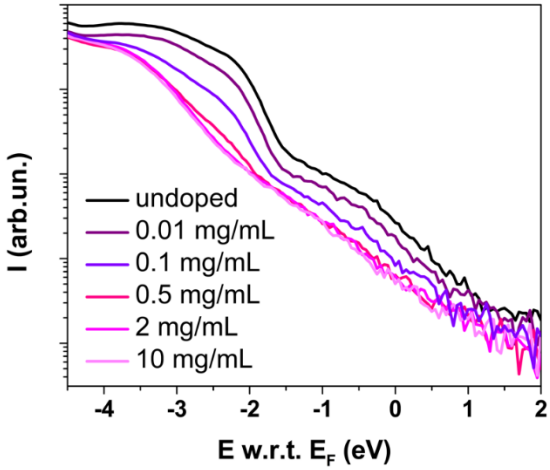


*Figure 4.28. Original data from the UPS experiment in the valence region.*

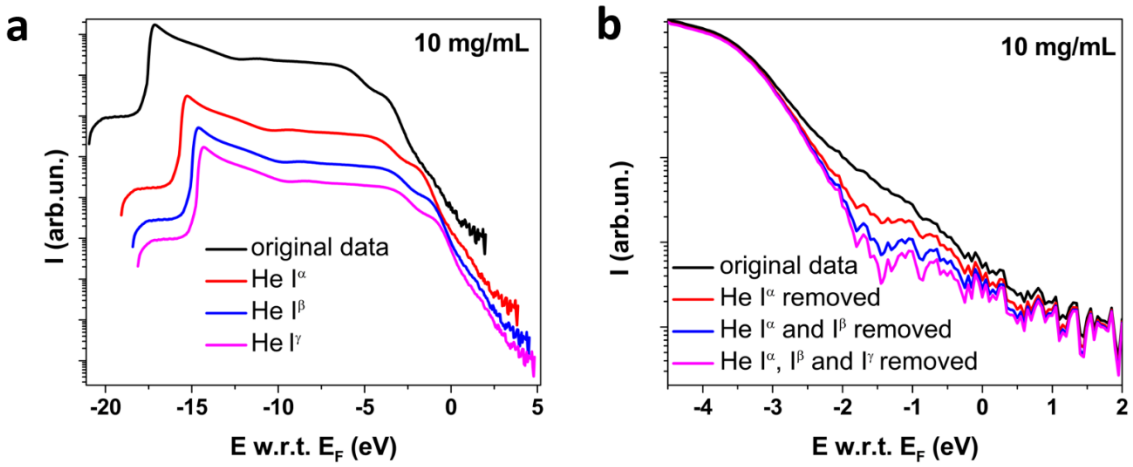


*Figure 4.29. UPS spectra of the "10 mg/mL" sample, plotted together with the spectra resulting from the non-monochromatic radiation (a) and the same spectrum with gradually removed satellites (b).*

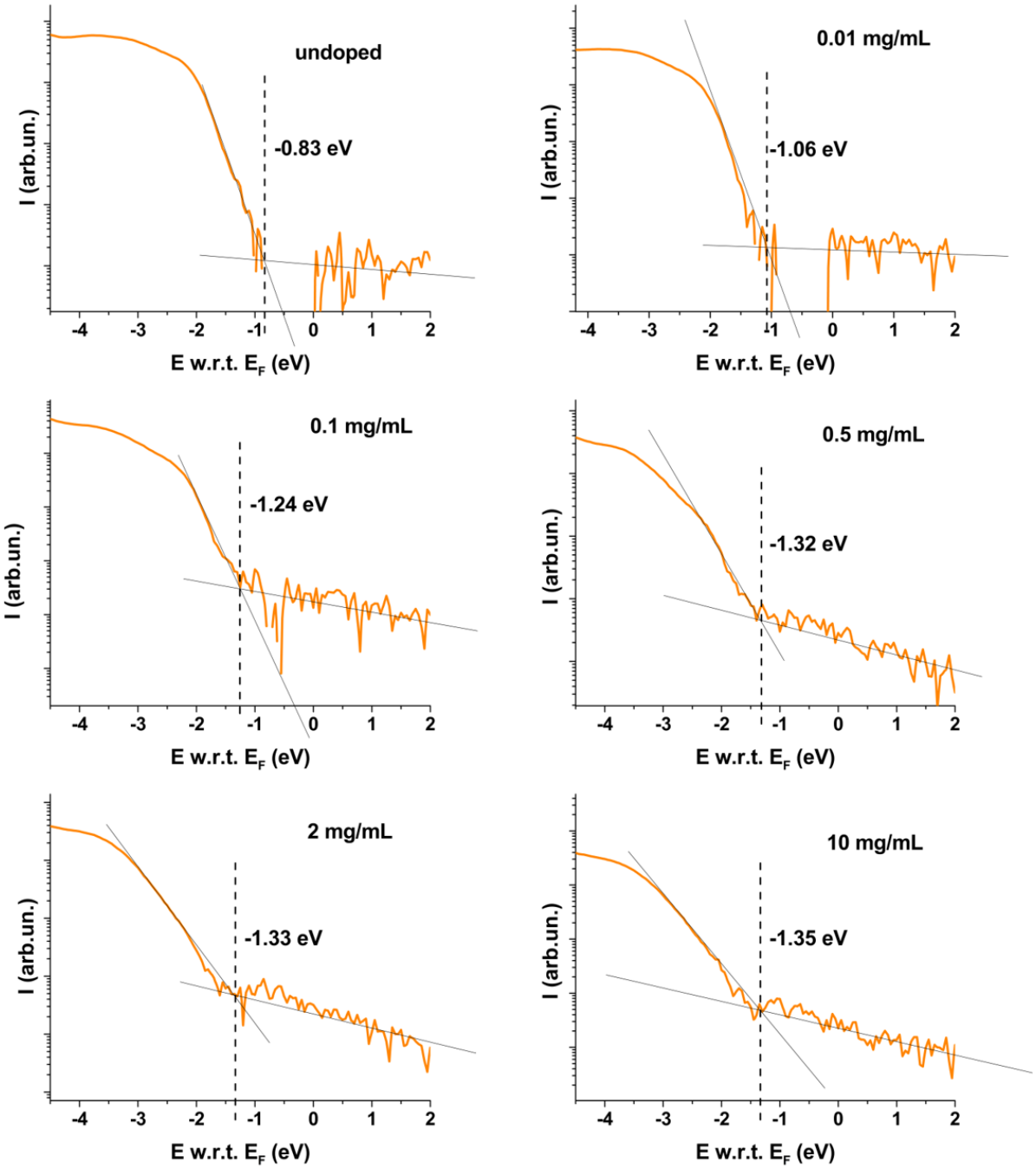


*Figure 4.30. E w.r.t. $E_F$ extracted for each doping concentration.*

Figure 4.31 shows the valence band onset energy with respect to $E_F$ for different dopant concentrations. The intersection of the average background level with the extrapolation of the linear part of the valence band onset allows the determination of the ionization energy with respect to Fermi level (*E w.r.t.* $E_F$). For the undoped MAPI samples, the absolute value of this difference is around 0.83 eV, placing the $E_F$ in the middle of the bandgap.[39] The position of $E_F$ increases along with the dopant concentration, reaching ~0.3 eV below the $E_C$ at dopant concentrations ≥ 0.2 mg/mL. This clearly demonstrates the n-type character of the doped samples. For the doped samples, $E_{vac}$ changed by around –0.3 eV, which can be interpreted as the energy of the surface dipoles ($E_\mu$) resulting probably from the altered surface composition due to the doping method. The energy of the surface dipole for the undoped MAPI was therefore assumed to be close to zero. The energy levels are schematically presented in Figure 4.32 for different doping concentrations and the values of *E w.r.t.* $E_F$, *WF* and $E_\mu$ are tabulated in Table 4.2.

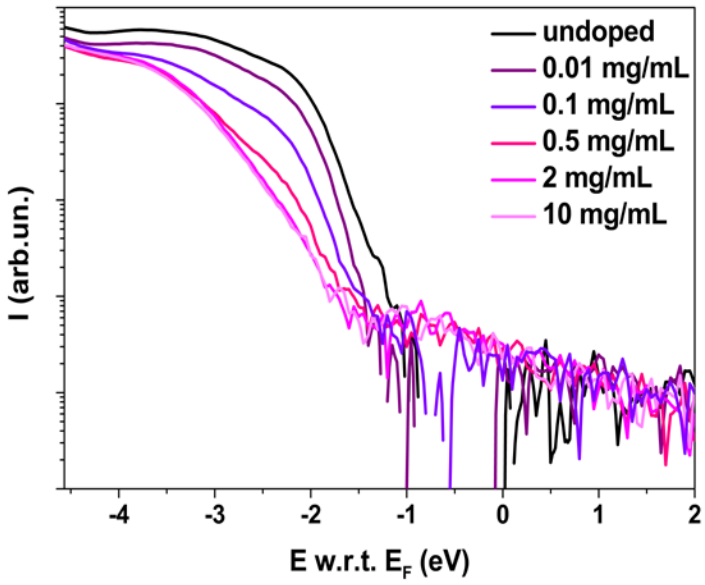


*Figure 4.31. UPS spectra of the valence band region, after removing the satellites for different doping concentrations.*

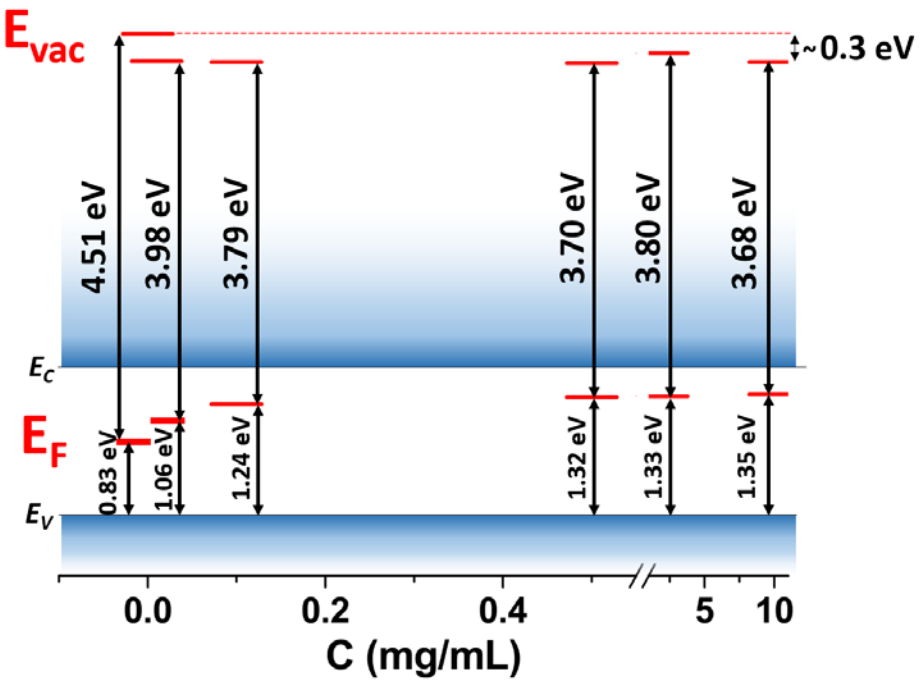


*Figure 4.32. Energy levels concluded from the UPS spectra and the bandgap calculated from the UV-Vis spectra.*

*Table 4.2. Energy values for different doping concentrations, determined from the UPS measurement and Eg = 1.63 eV.*

| ***C* (mg/mL)** | **0** | **0.01** | **0.1** | **0.5** | **2** | **10** |
|---|---|---|---|---|---|---|
| ***E w.r.t.E*$_F$ (eV)** | -0.83 | -1.06 | -1.24 | -1.32 | -1.33 | -1.35 |
| ***WF* (eV)** | 4.51 | 3.98 | 3.79 | 3.70 | 3.80 | 3.68 |
| ***E*$_\mu$ *(eV)*** | 0 | -0.3 | -0.31 | -0.32 | -0.21 | -0.31 |

## 4.3.6 Mott-Schottky analysis

The Mott-Schottky analysis allows to estimate the majority charge carrier concentration on a semiconductor. It consists in measuring the capacitance as a function of voltage at given frequency. A blocking contact is located on one side of a semiconductor and an ohmic contact on the other to form a sandwich-like structure. Low leakage current under reverse bias allows for an accurate capacitance measurement and, in the ideal case, makes the series capacitance and parallel capacitance equal. In order to reduce the leakage current, an ultrathin layer (<10 nm) of an insulating polymer (poly(methyl methacrylate), PMMA) between MAPI and gold electrode was introduced (see Chapter 6 for details).

The frequency applied in this measurement was chosen to be high enough in order to avoid the impact of the mobile ions on the capacitance[40–42]. To that aim, the capacitance was measured as a function of frequency and voltage and the result for MAPI doped with 10 mg/mL $SmI_2$ is shown in Figure 4.33a. At lower frequencies ions can contribute to the overall capacitance, which is manifested in dramatic rise of this value. At the frequency above 1 MHz, probably the artefact coming from the setup can be observed. A small window of plateau is present at around 100 kHz, thus this frequency was selected for further analysis. As mobile ions are known to cause the hysteresis[43], the samples were measures at the rate of 120 mV/s.

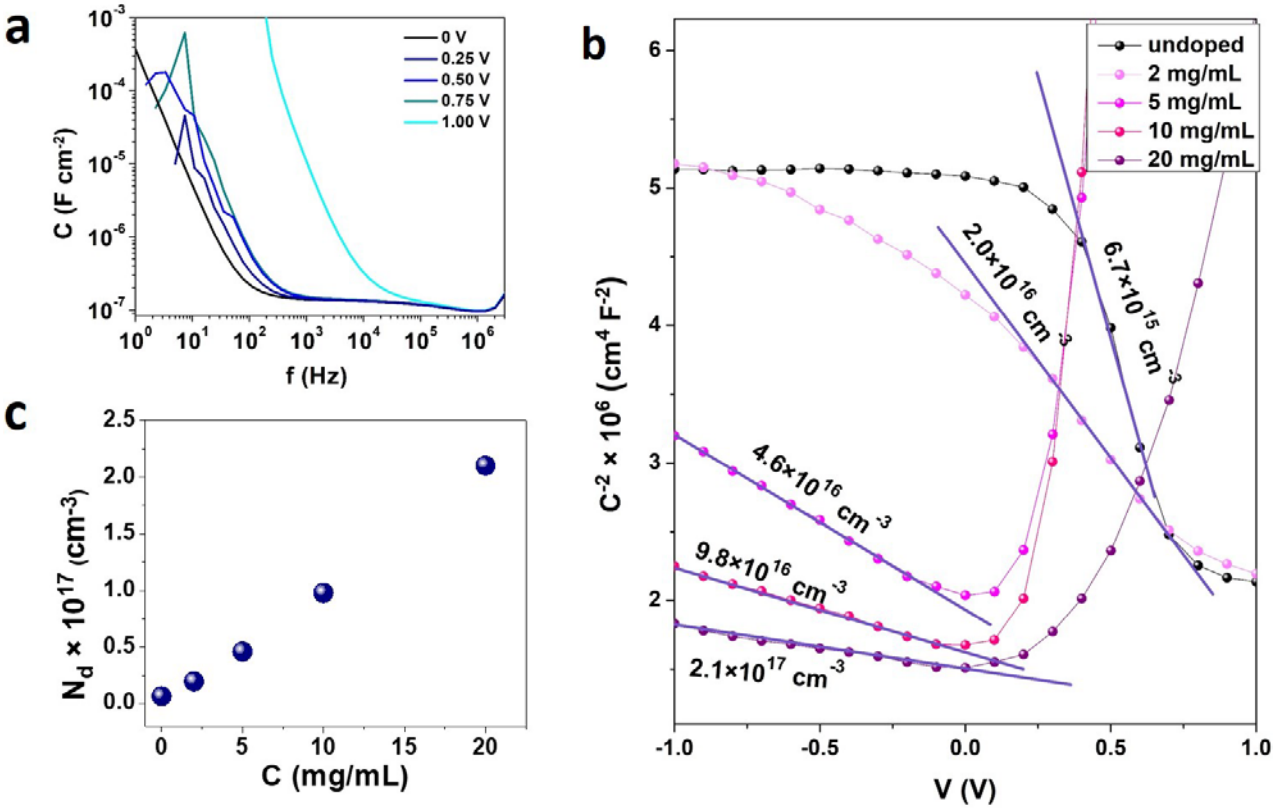


*Figure 4.33. Capacitance as a function of frequency and bias for MAPI doped with 10 mg/mL $SmI_2$ (a), Mott-Schottky plots of the undoped MAPI and doped with different $SmI_2$ concentrations (b) and charge carrier density (c).*

On the Mott-Schottky plots presented in Figure 4.33b, a clear plateau at reversed bias is observed for the undoped sample. It is associated with the depletion layer thickness that is higher than the thickness of the sample[44]. As charge carrier density increases with the doping concentration, the depletion layer thickness increases, thus the plateau region shifts towards lower voltage. To calculate the majority charge carrier density from the slope of the Mott-Schottky plot, *Fluxim* software was used, taking into account

the layer of insulating PMMA between perovskite and top metal electrode*. The electron concentration was estimated to be $2.1 \times 10^{17}$ $cm^{-3}$ for the highest conductivity, with an almost linear charge carrier concentration increase with the doping concentration (Figure 4.33c), ranging from $2\times10^{16}$ $cm^{-3}$ for the undoped MAPI to $2.1\times10^{17}$ $cm^{-3}$ for the highest doping concentration. These values are lower than expected, considering the XPS analysis, where measured samarium concentrations are in the range of $10^{21}$ $cm^{-3}$. In order to elucidate this discrepancy, conductivity measurements as function of temperature were carried out. The investigation focused on the sample exhibiting the highest conductivity increase, (10 mg/mL) taking the undoped MAPI sample as a reference. The measurement of the conductivity as a function of temperature was performed by cooling the sample from 373 K to 188 K (Figure 4.34). The activation energy $E_a$ is determined from the slope of Arrhenius plot. For the doped sample, two different slopes can be distinguished, corresponding probably to two different transport mechanisms with the offset at around 250 K. Above that temperature, the activation energy is similar for both undoped and doped MAPI ($E_a \approx E_{a1} \approx 500$ meV). Similar values of $E_a$ and $E_{a1}$ suggest that the charge transport takes place mainly at grain boundaries, where 500 meV would be the energy barrier of the grain boundaries. Below 250 K, the transfer at grain boundaries can only occur by tunneling due to the height of the barrier. Tunneling mechanism is not activated by temperature since the transfer occurs at constant energy. Nevertheless, below 250 K the activation energy $E_{a2}$ can be determined for the doped sample and it was found to be around 350 meV. Such activation energy could result of the dopant ionization giving rise to a phenomenon of dopant freezing, even at room temperature. Such dopant freeze-out may explain the discrepancy of the charge carrier density values measured using the Mott Schottky method and the XPS measurement, as the prior is sensitive only to the ionized dopant, while the latter measures the overall dopant concentration. Note that a similar behavior was observed for Mg dopants in p-type GaN where ionization energy is about 190 meV[45]. Similarly to the results presented in Figure 4.4. a slight discontinuity at around 340 K can correspond to the phase transition for both samples and a measurement at larger temperature range would make it more evident.

* Calculations of the charge carrier density and simulations of the Mott-Schottky plots, discussed in the next section, were carried out in collaboration with Dr. Bastien Politi and Dr. Raphael Clerc from the Hubert Curien Laboratory at the University of Saint-Etienne.

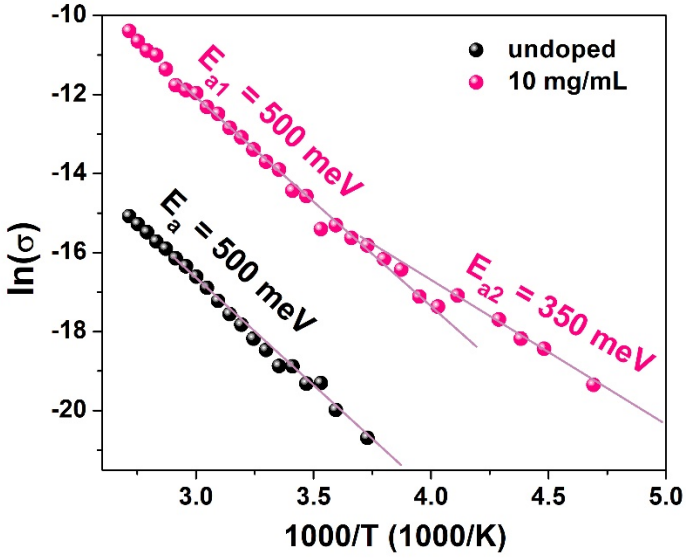


*Figure 4.34. Arrhenius plot of the temperature dependent conductivity for undoped MAPI and doped with 10 mg/mL $SmI_2$.*

To confirm that the dopant freeze-out can explain both low charge carrier density measured using the Mott-Schottky method and two distinguished transport mechanisms observed on the temperature dependent conductivity measurements, simulations were carried out, using *Fluxim* software. Mott-Schottky plots of the sample exhibiting the highest conductivity (10 mg/mL) were simulated for different activation energies, using the experimental data for the $E_a$ = 350 meV. The simulations were carried out using a small signal drift diffusion solver[46] and ionic transport parameters (concentration, mobility) reported elsewhere[47–49]. Charge carrier concentration values ($N_d$) extracted from the simulated plots are plotted against the dopant concentration ($C_d$) determined using the XPS measurement in Figure 4.35. As the $E_a$ decreases, the charge carrier concentration values approach the values of dopant concentration, suggesting that indeed the dopant freeze-out can be the reason of the low level of ionized dopant at room temperature.

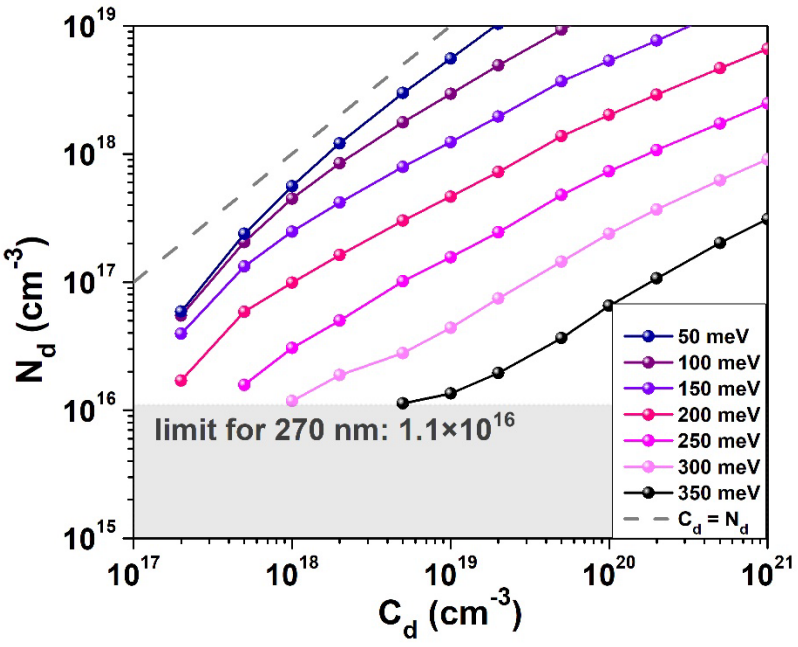


*Figure 4.35. Impact of the dopant activation energy $E_a$ on the charge carrier density ($N_d$), extracted from simulated Mott-Schottky plots, as a function of the dopant concentration, determined from the XPS.*

## 4.3.7. Hall effect[†]

Hall effect measurement allows to determine the type of majority charge carriers, as well as to obtain free charge carrier density. When combined with the conductivity measurement, it is possible to calculate the charge carrier mobility. Samples of high resistivity, such as perovskites, require a measurement in AC mode, in order to increase the signal-to-noise ratio. Such mode consists in applying a sinusoidal magnetic field (***B***) and measuring a sinusoidal resistance of the sample. A Hall effect measurement in the dark and AC mode was performed on MAPI doped with 10 mg/mL $SmI_2$ solution (Figure 4.36a) and a relatively clear signal was obtained, which is confirmed by the Fourier transform in Figure 4.36b. The majority charge carrier was found to be n-type, which is in agreement with all the previous findings. The majority charge carrier density of this sample is $2.4 \times 10^{13}$ $cm^{-3}$, which is 4 orders of magnitude lower than what stems from the Mott-Schottky analysis and 7 orders of magnitude lower comparing to the XPS. The calculated charge carrier mobility is 12.63 $cm^2V^{-1}s^{-1}$. These values, in spite of being in disagreement with the findings from different experimental techniques, are quite similar to the

[†] The Hall effect measurement was performed in collaboration with Semilab Semiconductor Physics Laboratory Co. Ltd. Budapest, Hungary

values found in the literature (Table 4.3), except for the $MAPb_{0.5}Sn_{0.5}I_3$ doped with 5% $F_4TCNQ$, that demonstrated the highest so far conductivity increase and is extensively described in Chapter 2. This discrepancy can indicate still insufficient understanding of the electronic properties of perovskite materials and of doped perovskites in particular. In these circumstances further investigation of the charge transport mechanism is necessary in order to fully understand the properties of the majority charge carrier of these materials.

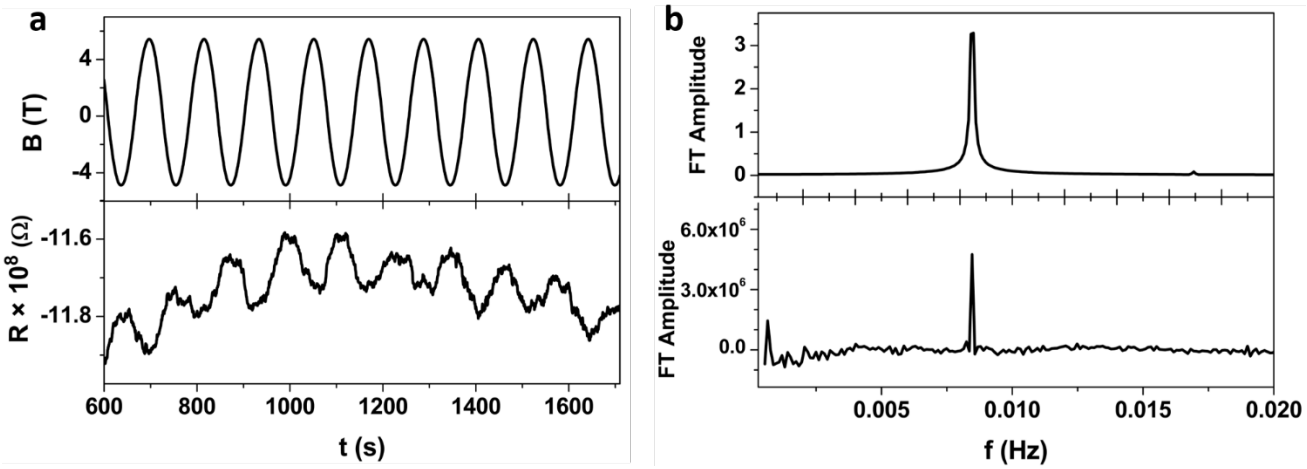


*Figure 4.36. AC Hall effect measurement of MAPI doped with 10 mg/mL $SmI_2$ solution.*

*Table 4.3. majority charge carrier density (Nd) and mobility (m) for different perovskite-based materials, measured using different techniques.*

| system | method | $N_d$ ($cm^{-3}$) | μ ($cm^2 V^{-1}s^{-1}$) | reference |
|---|---|---|---|---|
| $MAPb_{0.5}Sn_{0.5}I_3$ + 5% $F_4TCNQ$ | Hall effect | $5.0 \times 10^{17}$ | 2.2 ± 0.9 | [1] |
| $MAPbI_3$ | Photo-Hall | $1.5 \times 10^{11}$ | 21 | [2] |
| $MAPbI_3$ + 5%$PbI_2$ | Photo-Hall | $2.8 \times 10^{12}$ | 20 | |
| $MASnI_3$ | Seebeck coefficient | $1.1 \times 10^{14}$ | n/d | [50] |
| $MAPbI_3$ | Seebeck coefficient | $4.8 \times 10^{11}$ | n/d | |
| $MAPbBr_3$ | Hall effect | $5.0 \times 10^{9}$ | n/d | [18] |
| $MAPbBr_3$ + 10% $Bi^{3+}$ | Hall effect | $10^{12}$ | n/d | |

## Conclusions

This chapter presents the MAPI thin film doping with five different dopants, $Cd^{2+}$, $Pd^{2+}$, $Ru^{2+}$, $Sm^{2+}$ and $Sn^{2+}$, amongst which $Sm^{2+}$ was chosen to run a more in-depth study, mainly due to its metastable $Sm^{2+}$ ion and a possible subsequent oxidation inside the perovskite crystal lattice. MAPI thin films were fabricated using the spin coating method and doped with $Sm^{2+}$ from a solution of $SmI_2$ spin coated on top of the existing film, resulting in the $Sm^{2+}$ incorporation into the MAPI layer. The XRD patterns for the samples doped with concentration 2-20 mg/mL resemble those typical for MAPI. For the highest doping concentration, additional peaks are observed, pointing to phase separation with the dopant containing species, which might be the reason for the decreased conductivity. Complete PL quenching is observed for doping concentrations 2-20 mg/mL. Yet, the detailed quenching mechanism cannot be determined from the existing data. Interestingly, the value of the band gap remains unchanged upon doping. The oxidation of the dopant to $Sm^{3+}$ is confirmed by XPS analysis. The presence of $Sm^{3+}$-containing residue on the surface was evidenced using AFM and SEM, whereas ToF SIMS and XPS depth-atomic profiles showed the dopant penetration throughout the layer. The release of an electron during the oxidation of $Sm^{2+}$ is the direct reason for the n-type doping, which was confirmed by the UPS measurement, that showed a shift of the Fermi level from the middle of the bandgap to around 280 meV below the conduction band bottom. Upon this shift, the conductivity increased by almost 3 orders of magnitude for a doping concentration of 10 mg/mL. The temperature-dependent conductivity measurements allowed to calculate the activation energy for the 10 mg/mL doped sample of to be of 350 meV. This is therefore the energy needed for all the Sm2+ ions to oxidize and it is in agreement with the EF. This energy being rather high, comparing to traditional semiconductors, leads to the effect of dopant freeze-out at RT, which was confirmed by Mott-Schottky plots simulations for different activation energies. The Hall effect measurements revealed once again the n-type of majority charge carrier, however, the charge carrier density was found to be roughly 4 orders of magnitude lower than the one found using the Mott-Schottky method, which indicates that more profound investigation towards the transport mechanism in these materials should be undertaken in the future.

**References**


[1] J. Euvrard, O. Gunawan, X. Zhong, S. P. Harvey, A. Kahn, D. B. Mitzi, *Mater. Adv.* **2021**, *2*, 2956.

[2] J. Euvrard, O. Gunawan, D. B. Mitzi, *Adv. Energy Mater.* **2019**, *9*, DOI 10.1002/aenm.201902706.

[3] J. Euvrard, Y. Yan, D. B. Mitzi, *Nat. Rev. Mater.* **2021**, *6*, 531.

[4] K. Arashiba, R. Kanega, Y. Himeda, Y. Nishibayashi, *Chem. Lett.* **2020**, *49*, 1171.

[5] G. M. Cockrell, G. Zhang, D. G. VanDerveer, R. P. Thummel, R. D. Hancock, *J. Am. Chem. Soc.* **2008**, *130*, 1420.

[6] R. D. Shannon, *Acta Crystallogr. Sect. A* **1976**, *32*.

[7] M. Szostak, D. J. Procter, *Angew. Chemie - Int. Ed.* **2012**, *51*, 9238.

[8] T. Wang, K. C. Pitike, Y. Yuan, S. M. Nakhmanson, V. Gopalan, B. Jalan, *APL Mater.* **2016**, *4*, 126111.

[9] G. Sava, T. Giraldi, G. Mestroni, G. Zassinovich, *Chem. Biol. Interact.* **1983**, *45*, 1.

[10] M. Coluccia, G. Sava, F. Loseto, A. Nassi, A. Boccarelli, D. Giordano, E. Alessio, G. Mestroni, *Eur. J. Cancer* **1993**, *29*, 1873.

[11] I. Bratsos, B. Serli, E. Zangrando, N. Katsaros, E. Alessio, *Inorg. Chem.* **2007**, *46*, 975.

[12] M. Szostak, M. Spain, D. J. Procter, *J. Org. Chem.* **2014**, *79*, 2522.

[13] N. B. Desai, K. Byrappa, G. S. Gopalakrishna, S. Srikantaswamy, A. B. Kulkarni, *Bull. Mater. Sci.* **1987**, *9*, 317.

[14] D. Barboni, R. A. De Souza, *Energy Environ. Sci.* **2018**, *11*, 3266.

[15] Y. C. Zhao, W. K. Zhou, X. Zhou, K. H. Liu, D. P. Yu, Q. Zhao, *Light Sci. Appl.* **2017**, *6*, e16243.

[16] T.-Y. Yang, G. Gregori, N. Pellet, M. Grätzel, J. Maier, *Angew. Chemie* **2015**, *127*, 8016.

[17] W.-J. Yin, T. Shi, Y. Yan, *Appl. Phys. Lett.* **2014**, *104*, 63903.

[18] A. L. Abdelhady, M. I. Saidaminov, B. Murali, V. Adinolfi, O. Voznyy, K. Katsiev, E. Alarousu, R. Comin, I. Dursun, L. Sinatra, E. H. Sargent, O. F. Mohammed, O. M. Bakr, *J. Phys. Chem. Lett.* **2016**, *7*, 295.

[19] N. K. Noel, S. N. Habisreutinger, A. Pellaroque, F. Pulvirenti, B. Wenger, F. Zhang, Y. H. Lin, O. G. Reid, J. Leisen, Y. Zhang, S. Barlow, S. R. Marder, A. Kahn, H. J. Snaith, C. B. Arnold, B. P. Rand, *Energy Environ. Sci.* **2019**, *12*, 3063.

[20] S. Singh, D. Kabra, *J. Mater. Chem. C* **2018**, *6*, 12052.

[21] J. Even, L. Pedesseau, J.-M. Jancu, C. Katan, *J. Phys. Chem. Lett.* **2013**, *4*, 2999.

[22] G. Krill, A. Amamou, J. P. Senateur, *J. Phys. F Met. Phys.* **1980**, *10*, 1889.

[23] Y. Mori, S. Tanemura, S. Koide, Y. Senzaki, P. Jin, K. Kaneko, A. Terai, N. Nabotova-Gabin, *Appl. Surf. Sci.* **2003**, *212–213*, 38.

[24] C. Noël, J.-J. Pireaux, Y. Busby, A. Agresti, S. Pescetelli, A. Di Carlo, L. Houssiau, **2018**, 7.

[25] F. Matteocci, Y. Busby, J.-J. Pireaux, G. Divitini, S. Cacovich, C. Ducati, A. Di Carlo, *ACS Appl. Mater. \& interfaces* **2015**, *7*, 26176.

[26] Y. Zhong, G. Liu, Y. Su, W. Sheng, L. Gong, J. Zhang, L. Tan, Y. Chen, *Angew. Chemie* **2022**, *134*, e202114588.

[27] S. P. Harvey, F. Zhang, A. Palmstrom, J. M. Luther, K. Zhu, J. J. Berry, *ACS Appl. Mater. Interfaces* **2019**, *11*, 30911.

[28] S. P. Harvey, Z. Li, J. A. Christians, K. Zhu, J. M. Luther, J. J. Berry, *ACS Appl. Mater. Interfaces* **2018**, *10*, 28541.

[29] J. A. Chang, J. H. Rhee, S. H. Im, Y. H. Lee, H. J. Kim, S. Il Seok, M. K. Nazeeruddin, M. Gratzel, *Nano Lett.* **2010**, *10*, 2609.

[30] C. Jiang, S. L. Lim, W. P. Goh, F. X. Wei, J. Zhang, *ACS Appl. Mater. Interfaces* **2015**, *7*, 24726.

[31] G. Xing, N. Mathews, S. S. Lim, N. Yantara, X. Liu, D. Sabba, M. Grätzel, S. Mhaisalkar, T. C. Sum, *Nat. Mater.* **2014**, *13*, 476.

[32] Y.

[33] S. J. Sque, R. Jones, P. R. Briddon, *Phys. status solidi* **2007**, *204*, 3078.

[34] M. Caputo, N. Cefarin, A. Radivo, N. Demitri, L. Gigli, J. R. Plaisier, M. Panighel, G. Di Santo, S. Moretti, A. Giglia, M. Polentarutti, F. De Angelis, E. Mosconi, P. Umari, M. Tormen, A. Goldoni, *Sci. Rep.* **2019**, *9*, 15159.

[35] K. G. Lim, H. B. Kim, J. Jeong, H. Kim, J. Y. Kim, T. W. Lee, *Adv. Mater.* **2014**, *26*, 6461.

[36] B. J. Foley, D. L. Marlowe, K. Sun, W. A. Saidi, L. Scudiero, M. C. Gupta, J. J. Choi, *Mater. Eng. Sci. Div. 2015 - Core Program. Area 2015 AIChE Annu. Meet.* **2015**, *243904*, 581.

[37] F. Zhang, F. Ullrich, S. Silver, R. A. Kerner, B. P. Rand, A. Kahn, *J. Phys. Chem. Lett.* **2019**, *10*, 890.

[38] F. Zhang, S. H. Silver, N. K. Noel, F. Ullrich, B. P. Rand, A. Kahn, *Adv. Energy Mater.* **2020**, *10*, 1.

[39] Y. F. Chen, Y. T. Tsai, D. M. Bassani, R. Clerc, D. Forgács, H. J. Bolink, M. Wussler, W. Jaegermann, G. Wantz, L. Hirsch, *J. Mater. Chem. A* **2016**, *4*, 17529.

[40] O. Almora, C. Aranda, I. Zarazua, A. Guerrero, G. Garcia-Belmonte, *ACS Energy Lett.* **2016**, *1*, 209.

[41] T. Pang, K. Sun, Y. Wang, S. Luan, Y. Zhang, Y. Zhu, Z. Hu, R. Jia, *J. Mater. Chem. C* **2020**, *8*, 1962.

[42] G. Garcia-Belmonte, J. Bisquert, *ACS Energy Lett.* **2016**, *1*, 683.

[43] O. Almora, C. Aranda, E. Mas-Marzá, G. Garcia-Belmonte, *Appl. Phys. Lett.* **2016**, *109*, DOI 10.1063/1.4966127.

[44] T. Kirchartz, W. Gong, S. A. Hawks, T. Agostinelli, R. C. I. MacKenzie, Y. Yang, J. Nelson, *J. Phys. Chem. C* **2012**, *116*, 7672.

[45] L. Hirsch, A.-S. Barriere, *J. Appl. Phys.* **2003**, *94*, 5014.

[46] M. T. Neukom, A. Schiller, S. Züfle, E. Knapp, J. Ávila, D. Pérez-del-Rey, C. Dreessen, K. P. S.

Zanoni, M. Sessolo, H. J. Bolink, others, *ACS Appl. Mater. \& interfaces* **2019**, *11*, 23320.

[47] M. H. Futscher, M. K. Gangishetty, D. N. Congreve, B. Ehrler, *J. Chem. Phys.* **2020**, *152*, 44202.

[48] J. Thiesbrummel, V. M. Le Corre, F. Peña-Camargo, L. Perdigón-Toro, F. Lang, F. Yang, M. Grischek, E. Gutierrez-Partida, J. Warby, M. D. Farrar, others, *Adv. Energy Mater.* **2021**, *11*, 2101447.

[49] V. M. Le Corre, J. Diekmann, F. Peña-Camargo, J. Thiesbrummel, N. Tokmoldin, E. Gutierrez-Partida, K. P. Peters, L. Perdigón-Toro, M. H. Futscher, F. Lang, others, *Sol. RRL* **2022**, *6*, 2100772.

[50] F. Hao, C. C. Stoumpos, R. P. H. Chang, M. G. Kanatzidis, *J. Am. Chem. Soc.* **2014**, *136*, 8094.

# 5. Conclusions and Perspectives

Years of research on halide perovskite semiconductors resulted in ever growing knowledge of these particular semiconductors. Along with the increase of knowledge, an increase of proposed applications in which perovskites may become promising materials to replace silicon in the next generation electronics. Perovskites can be obtained by low-tech methods (such as spin coating, ink printing, doctor blade), hence the production costs can be significantly decreased. What is perhaps even more important, on the verge of an energy crisis, is that the Energy Return on Investment (EROI) is significantly lower for perovskite-based devices than silicon-based ones, mainly because perovskites do not require the high energy purification process. These aspirations are, however, impossible to achieve without the possibility of perovskite doping. The controlled doping technology, along with understanding of the mechanisms and processes that govern the doping, are on the basis of this new era in electronics, called the “perovskite era”.

This thesis attempts to addresses these challenges by providing experimental evidence for the n-type doping of MAPI. The method used for the n-doping is believed to work analogously also for the p-type doping and it is the first step for achieving controlled and low-tech doping.

This dissertation starts with a short story of the perovskite crystal structure that began in the mid nineteenth century, along with the first laboratory synthesis of halide perovskites that took place at the end of that century. More than a century later, the first prototype of a perovskite-based solar cell was fabricated[1]. A MAPI-sensitized mesoporous $TiO_2$ electrode in a liquid electrolyte and with platinum counter electrode reached the photo conversion efficiency of 3.8%. Even though the electrolyte caused the perovskite degradation, this discovery has started an everlasting race of the perovskite-based solar cell efficiency.

The second chapter gives an introduction to the core of the problem of interest: perovskite doping. To date, there have been few attempts towards perovskite doping, and even less focus on the effect of doping on the electric properties, such as conductivity, charge carrier density, charge carrier mobility or Fermi level position. Although a handful of reports show an enhancement of conductivity, the origins of such enhancement remain unclear. Most of the experimental doping covered in the literature operates in the area of doping at grain boundaries. The elucidation of the quantitative impact of the doping on the perovskite properties still needs to be achieved. The results of simulations show that doping

is a promising field with a lot still to be achieved. However, technical solutions are needed to perform doping of the ionic crystal.

The third chapter is a report of the optimization of the solar cells' fabrication parameters. The perovskite thin films were synthesized via spin coating using lead acetate trihydrate and methhylammonium iodide as perovskite precursors. The films were characterized by XRD, which exhibited typical tetragonal MAPI diffraction patterns. The absorption spectrums revealed a bandgap of 1.58 eV and the AFM images showed a smooth polycrystalline layer with a grain size of around 100 nm. The parameters of the perovskite solar cells were optimized for inverted MAPI based devices. Three different hole transporting materials and a number of electron transporting materials were compared. The final device architecture was chosen to be ITO / PTAA / MAPI / PCBM / Ca / Al with the with the average *PCE* of (10. 6 ± 1.3) %.

Chapter 4 reports the successful achievement of identifying a suitable dopant ion and method for n-type doping. Among five different plausible dopants, samarium(II) and palladium(II) seem to be the most suitable candidates. Samarium was chosen due to its known metastable 2+ oxidation state and greater stability of the 3+ state. A two-step spin coating based doping method was developed to circumvent the reactivity of Sm(II) towards residual water. It is demonstrated that $Sm^{2+}$ oxidizes inside the perovskite crystal structure to $Sm^{3+}$, thereby releasing an electron to the conduction band as confirmed by XPS. This leads to a shift of the Fermi level towards the conduction band, which was evidenced by UPS and Kelvin probe measurement. As a consequence, the conductivity increased by almost 3 orders of magnitude from $10^{-8}$ S/cm for the undoped MAPI to up to $10^{-5}$ S/cm for MAPI doped with 10 mg/mL of $SmI_2$. Finally, XRD shows no alternation of the crystal structure, except for the highest doping concentrations, and the analysis of the absorption spectra indicates no change in the bandgap.

A crucial missing element of the puzzle is definite proof that the dopant resides on the $Pb^{2+}$ site and not at grain boundaries. One technique that could bring us closer to the answer would be Kelvin probe force microscopy (KPFM) on the cross section of the doped layer. A map of work function could help to determine the dopant position. A more precise method for the investigation of the environment of the dopant would be X-ray absorption spectroscopy (XAS), coupled with transmission electron microscope (TEM). Other information that is missing in this thesis is more detailed information on the charge transport mechanism and the properties of the minority charge, that can be extracted from carrier-resolved photo Hall effect measurement[2]. These and other investigations will be the subject of interest in the continuation of this research.

The doping method presented in Chapter 4 can be used to dope the perovskite with other elements, which are metastable at the 2+ oxidation state and stable at 3+. In particular, the preliminary results with palladium(II) were shown to be promising, and an attempt of doping with Pd (II) using a two-step doping method will be undertaken in the future. Other interesting candidates could be found in the group of lanthanides, with $Eu^{2+}$ as the first example. Further search would focus on the *p* group metals, such as indium, bismuth or antimony.

Doping with metastable ions can be also employed for the p-type doping of perovskites. An ion which is metastable at 2+ and stable at 1+ will release a hole to the valence band, thus shifting the Fermi level towards VBM. Potential doping elements could be silver or thallium. Since the latter is around ten times more toxic than lead, few will try, which opens a niche for fearless scientists. Another approach to p-type doping can be to dope with the acceptors commonly used in OPV or OLED. These molecules are too large to fit in any interstitial position, hence only doping at grain boundaries is possible. This approach was already mentioned in chapter 2, however, a number of organic molecules have not been yet explored. In organic electronics, the most common acceptors are fullerene-based, such as $C_{60}$ itself or $C_{70}$, which are not practical due to low solubility in organic solvents. Other, more soluble, organic acceptors are shown in Figure 5.1. The diameter size of $C_{60}$ is 7 Å[3], so they are rather too big to occupy the $MA^+$ vacant, as the ionic radius of the methylammonium ion is 1.8 Å[4], but they might rather be homogeneously distributed in the bulk of the material.

Once the control of both n- and p-type doping of perovskite is achieved, understood and well controlled, it is possible to contemplate the inclusion of p-n junctions into devices. The device that is primarily aimed as a follow-up of this thesis is a solar cell. A perovskite-based solar cell with a p-n region within its active layer is expected to increase its $V_{OC}$ to the maximal theoretical value, i.e. to the value of the bandgap, by pinning the quasi-Fermi levels of holes and electrons respectively to the valence band maximum and conduction band minimum. This approach would result in the increase of *PCE* and, if applied to the best performance *PSC* architecture, new efficiency records would likely be achieved. Moreover, by pinning the Fermi levels of the doped sides of the perovskite respectively to the CBM and VBM, it would be possible to omit the charge transporting layers. This would simplify the fabrication process and significantly reduce the cost, as the sophisticated polymers and fullerene-derivative molecules are known for their high price. As it is well known, cost reduction opens the way for industrialization.

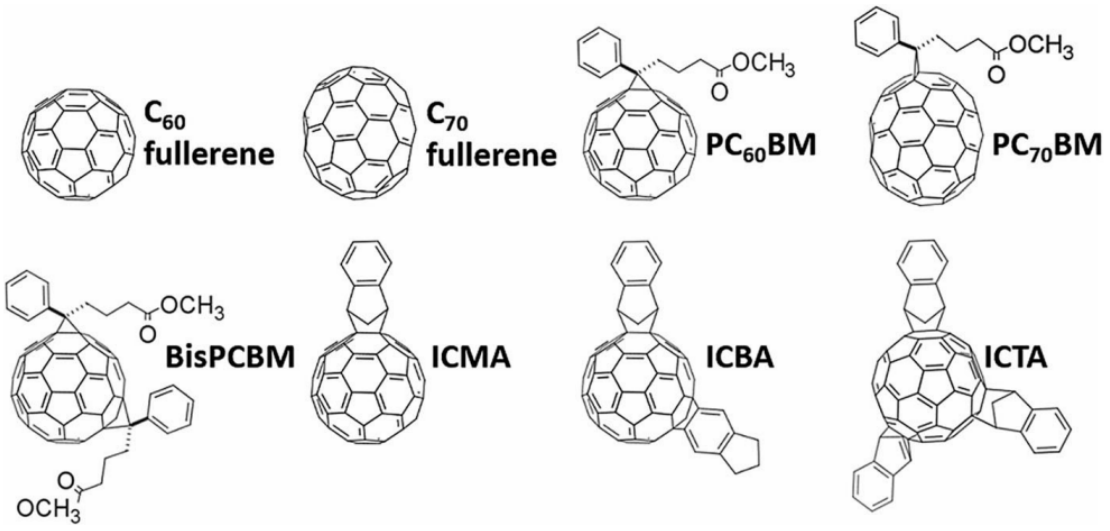


*Figure 5.1. Fullerene- based acceptors. Top: $C_{60}$ fullerene; $C_{70}$ fullerene; phenyl-$C_{61}$-butyric acid methyl ester (PCBM); phenyl-C71-butyric acid methyl ester ($PC_{70}BM$). Bottom: 1',4' -dihydro-naphtho [2',3' :1,2][5,6]fullerene-$C_{60}$ (ICMA); bis(1-[3-(methoxycarbonyl)propyl]-1-phenyl)-[6,6]C62 (BisPCBM); 1',1'',4' ,4''-tetrahydro-di [1,4]methanonaphthaleno[1,2:2',3',56,60:2'',3''][5,6]fullerene-$C_{60}$ (ICBA); indene-$C_{60}$-tris-adduct (ICTA). Reprinted with permission from* [5]

A similar approach can be employed for PeLEDs once doping has been mastered for perovskites whose structure and composition is more suitable for this type of application. Most commonly, a blend of 2D-3D perovskite is used in order to increase the density of recombination sites. For visible light emission, perovskites with wider bandgap (than MAPI) are used, with the general formula $(B)_2(A)_{n-1}Pb_nX_{3n+1}$ (where B and A = cations; X = halide)[6]. Doping of 2D structures can be more challenging, as a high concentration of dopant may accumulate between the 2D sheets and dominate the charge transport process. On the other hand, large spaces between the 2D structures can be used to host small amounts of dopants, changing the semiconductor type.

Introducing a p-n junction to perovskite-based photodetectors could, similarly to solar cells, enhance charge extraction. More importantly for photodetectors, the depletion layer at the p-n interface could reduce the charge recombination rate, resulting in a decrease of the leakage current. The most common perovskites used in photodetectors are those with the general formula $MAPbX_3$, where the halide site composition depends on the detected light[7,8]. Therefore, it is believed that the doping method developed within this thesis could be easily transferred into the application field of photodetectors.

In transistors, the *n* and *p* regions must be precisely defined. Using doped perovskites, it would be possible to fabricate both n-p-n and p-n-p transistors. To this end, a thin film of n- or p-doped

perovskite could be spin coated on a substrate, using either one or two-step doping method, referring to the nomenclature used in this work. Using a shadow mask, a stripe of dopant can be deposited, in the concentration high enough to over dope the region with the opposite domain. If the dopant is in the solution, it can be applied e.g. with a brush. Otherwise, the dopant can be thermally evaporated, provided that it will penetrate inside the perovskite film. Finally, the electrodes can be evaporated on top to finish the device.

As demonstrated above, our journey with doped perovskites has only begun. There are still a lot of unanswered fundamental questions, in particular regarding the doping location, mechanism and the charge transport properties. A motivation to answer these questions is based on the almost endless possible applications of perovskite-based p-n junctions, of which a few examples were given above. Nowadays, mankind seeks energy that is more affordable, cleaner, and more accessible to everyone. It is possible that perovskite-based electronics and energy production can satisfy these demands and contribute to making this planet a better place for all living species.

**References**


[1] M. T, K. A, T. K, S. Y, *J. Am. Chem. Soc.* **2009**, *131*, 6050.

[2] O. Gunawan, S. R. Pae, D. M. Bishop, Y. Virgus, J. H. Noh, N. J. Jeon, Y. S. Lee, X. Shao, T. Todorov, D. B. Mitzi, B. Shin, *Nature* **2019**, *575*, 151.

[3] H. W. Kroto, J. R. Heath, S. C. O'Brien, R. F. Curl, R. E. Smalley, *Nature* **1985**, *318*, 162.

[4] N.-G. Park, *Mater. Today* **2015**, *18*, 65.

[5] E. M. Speller, *Mater. Sci. Technol. (United Kingdom)* **2017**, *33*, 924.

[6] A. Tiwari, N. S. Satpute, C. M. Mehare, S. J. Dhoble, *J. Alloys Compd.* **2021**, *850*, 156827.

[7] Y. Xu, X. Wang, Y. Pan, Y. Li, E. Emeka Elemike, Q. Li, X. Zhang, J. Chen, Z. Zhao, W. Lei, *Front. Chem.* **2020**, *8*, DOI 10.3389/fchem.2020.00811.

[8] L. Dou, Y. M. Yang, J. You, Z. Hong, W.-H. Chang, G. Li, Y. Yang, *Nat. Commun.* **2014**, *5*, 1.

# 6. Methods

## 6.1 Fabrication

Perovskite thin films can be fabricated using a number of methods. Amongst them we can list thermal evaporation[1], spray coating[2], inkjet printing[3], doctor blade[4], drop casting[5] and spin coating[6–8]. The latter is especially popular for the small laboratory scale, solution processed fabrication, as it is uncomplicated, fast and fairly reproducible[9]. Moreover, the layer thickness can be controlled and reproduced quite precisely, manipulating either the spinning rate or the solution concentration. In this chapter, the process of solar cells fabrication will be described, including notably the techniques such as spin coating and thermal evaporation.

### 6.1.1 Perovskite solar cells

To fabricate the perovskite solar cell devices, as-purchased ITO-covered glass substrates were used. Perovskite thin films, as well as both charge transporting layers were deposited using spin coating, while the metal top electrodes were thermally evaporated.

**Spin coating**

This facile method of forming thin and uniform films from solution was first used to spread paint or pitch in 1940s. In 1958 it entered the world of science with the theoretical model of Emslie et al.[10]. Ever since, the choice of spin coating method for preparing thin films based devices seems a natural first choice, considering its low price, reproducibility and simplicity. The substrate, typically ITO or FTO coated glass in the case of perovskite solar cells, is placed on the sample holder (Figure 6.1). After the solution has been dropped onto the substrate, it is spun with a rate of hundreds to thousands rotations per minute (rpm). The centrifugal force causes the solvent to spread over the substrate and a part of it is, inevitably, discarded. As the spinning continues, the solvent evaporates, leading to an increase in the solvent concentration on the substrate and the creation of crystals nuclei, after reaching the supersaturation regime. Those nuclei that reach the critical radius $r_c$, will continue growing, so that the Gibbs free energy can decrease, as showed in Figure 6.2. The crystal growth continues until the sample is placed on a hot plate, where the rest of the solvent evaporates, freezing the polycrystalline film.

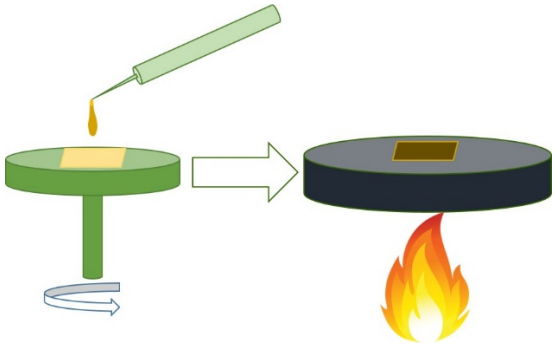

*Figure 6.1. Spin coating and annealing process.*

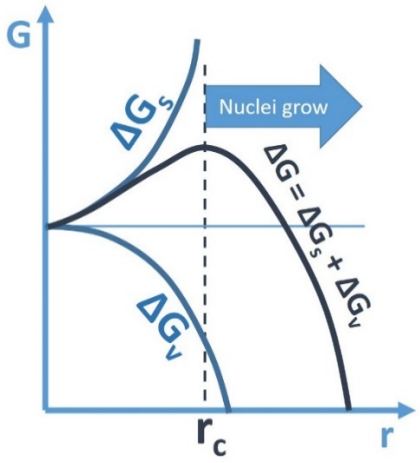


*Figure 6.2. Gibbs Free Energy G diagram for the crystal nucleation and growth. Free energy of the crystal is the sum of the free energy of the surface ($G_s$) and of the bulk ($G_v$). As the surface/bulk ratio is high for embryos, the surface term $G_s$ is dominant and it becomes less significant as the crystal grows.*

In this work, the optimization of the perovskite deposition process was made for a planar solar cell architecture. ITO (10 Ω/sq) covered glass substrates were cleaned in a sonication bath, first with the Hellmanex™ III (Sigma Aldrich) and in the DI water for 15 minutes each, then in isopropanol (4N) for 10 min. Subsequently, they were exposed to UV-ozone treatment for 15 minutes. 4.5 mg of poly(triaryl amine) (PTAA) was dissolved in 1 mL of toluene and stirred overnight at RT. After filtration with 0.45µm PTFE, the solution was spin coated onto the clean substrate at a spin rate of 6000 rpm for 30 s and dried for 10 min at 100°C, resulting in a 15 nm thin layer. For the perovskite solution, 0.72 M $PbAc_2 \cdot 3H_2O$ and 2.2 M MAI were dissolved in *N*,*N*-Dimethylformamide (DMF) and stirred at room temperature for 30 min. The solution was filtered with 0.45µm PTFE filter and spin coated at a spin rate of 6000 rpm for 2 min. The sample was then dried at RT for 3 min and annealed for 25 min at 100°C. The resulting perovskite film was around 190 nm thick. 20 mg of phenyl-$C_{61}$-butyric acid methyl ester (PCBM) was dissolved in 1 mL of

chlorobenzene (CB) and stirred overnight at 50°C. After filtering through a 0.45µm PTFE filter, the solution was spin coated at a spin rate of 2500 rpm for 1 min, forming a layer of the thickness of around 90 nm. Figure 6.3 shows the scheme of the solar cell device.

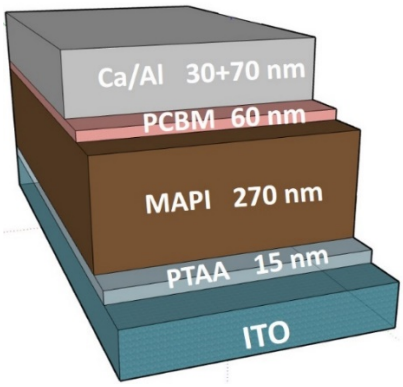


*Figure 6.3. Perovskite solar cell architecture.*

**Thermal evaporation**

A high current flow through a tungsten crucible containing a metal will cause it to heat. Together with the high vacuum in the evaporation chamber, it causes the metal to evaporate from the crucible and deposit on the samples mounted on the opposite wall of the metal source (Figure 6.4). The thickness of the matter deposited is controlled by the piezoelectric silica sensors placed next to the samples and properly calibrated. The sample holder can rotate to ensure a homogeneous layer thickness.

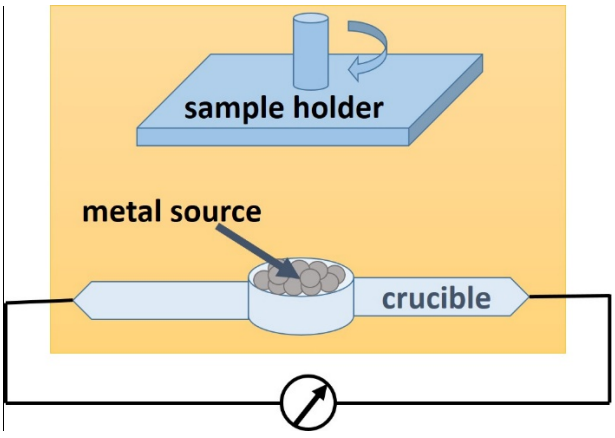


*Figure 6.4. Schematic representation of the thermal evaporation process.*

In this work, electrodes consisted of 30 nm Ca and 70 nm Al were thermally evaporated using a mask that defined the area of the cells to be 10.5 $mm^2$.

## 6.2 Microscopy

In the characterization of thin films, the morphology is one of the first and basic properties to examine. It allows to assure about the reproducibility and quality of the layers. While the optical microscopy might seem like the first choice, in case of micro- and nanomaterials, it is not capable of providing all the desired information about the samples, such as the grain size, shape, or layer roughness. Optical microscopy employs visible light with wavelengths of hundreds of nm, so all the features whose size is lower than that will be inevitably missing. This includes the grain size, which in perovskite thin films is typically in the range of tens to hundreds of nanometers. It is therefore impossible to reach the proper resolution and other types of microscopy need to be used. One of them is the atomic force microscopy (AFM), that is based on the mechanical measurement using an ultra-small tip or on the van der Waals force between the tip and the sample. Another technique is scanning electron microscopy, that uses electrons, with their wavelength small enough to be able to observe the surface details.

### 6.2.1 Atomic force microscopy (AFM)

One of the types of microscopy suitable for observing the features with the size below the visible wavelength is atomic force microscopy (AFM). The principle of operation is based on the van der Waals force between the probe and the sample that cause the deflection of the cantilever, on which the probe is mounted. This deflection is registered by the voltage on the piezoelectric element or by the laser light reflection position on the photodetector. Scanning over a couple of micrometers along and across, a height image is mapped. There are three modes in which AFM can operate: contact, non-contact and tapping mode.

In the contact mode, the probe swipes over the sample surface in the distance short enough to provide the repulsive van de Waals force to occur. The cantilever deflects as a result of this force.

In the non-contact mode, the probe oscillates in a short distance to the surface, where the van der Waals force is attractive. The oscillation prevents the probe to crash on the surface and leaves the sample untouched. As the height of the surface increases, the oscillation amplitude decreases. The feedback loop is used to adjust the amplitude to its original value and to gather the information about the surface topography.

In the tapping mode, the probe also oscillates over the surface, but with much higher amplitude than in case of the non-contact mode. This allows for a higher deflection signal, so easier control of the feedback loop information. On the other hand, working in this mode, the probe blunts faster.

In this work, Bruker NanoScope AFM was used and the imaging was performed in the tapping mode.

### 6.2.2 Scanning electron microscopy (SEM)

The other technique used for micro and nano imaging is Scanning Electron Microscopy (SEM). The electron emitter it typically made of $LaB_6$ or a tungsten wire. Field emission electron emitter is used for the high resolution nanostructure imagining. After being accelerated, an electron beam is scattered by the condenser lens and then focused by the objective lens down to 2-10 nm diameter at the sample surface. The lens aperture determines the angular distribution of the beam. The two directional scanning by the electron beam leads to the emission of Auger electrons, secondary and back scattered electrons, as well as emission of photons: characteristic and continuum X-rays, cathodolumiscence and fluorescent X-rays (Figure 6.5). These signals are collected by proper detectors, amplified and analyzed.

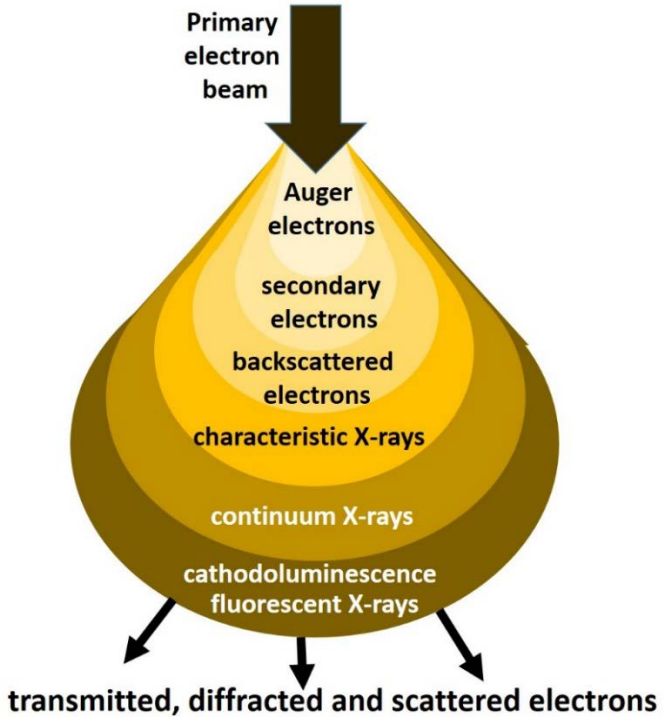


*Figure 6.5. Emission of electrons of different energy from different sample thickness. For the imaging, the secondary electrons are used. With the EDX spectrometer extension to SEM, the Auger electrons spectrum can determine the sample composition.*

For morphology analysis, the electrons of interest are the secondary electrons (SE). With their relatively low energy (around 50 eV), the SE's mean free path in the solid state matter is rather low. Consequently, only those close to the surface (a few nm) are able to escape. They are collected by the Everhart-Thornley detector. This detector responds also to the back scattered electrons, however, due to a low collection angle, the resulting signal from these electrons and consequently the image resolution is very low. The analysis of the secondary electrons allows to image the topology of the surface.

In this work, a SEM-FEG HR (JEOL 6700F) was used to perform the imaging.

## 6.3 Crystal structure - X-ray diffraction (XRD)

In 1912 Max von Laue discovered that crystal lattice can act as a grating for X-rays, causing their diffraction. Two years later, this discovery brought him a Nobel prize in physics. The X-rays are generated in the ray cathode tube by heating the filament and releasing the electrons that bombard the target material. The emitted spectrum is composed of several components, typically $K_{\alpha 1,}$ $K_{\alpha 2}$ and $K_{\beta}$. Among the four target materials used, Mo, Fe, Cr and Cu, the latter is the most popular, with themonochromated light of $CuK_{\alpha}$ = 1.5418Å. The collimated beam is directed onto the sample, while varying the angle $\Theta$. At those angles that satisfy the Braggs' law $n\lambda = 2d\sin\Theta$ (where $\lambda$ is the length of the electromagnetic radiation), constructive interference is observed, registered as a peak of intensity of the diffracted light. From the peak positions, the spacing *d* between the atoms in the crystal can be calculated. This enables the identification of the material, as each crystal has specific distances between the atoms. The sample is typically a powder in order to receive the average diffraction from all the crystallographic planes, but in this work, all the XRD patters are gathered from the as-annealed thin films surfaces. Therefore, in most of the XRD patters, the intensity peak characteristic only for one crystallographic plane is observed.

X-ray diffraction in this work was obtained using Bruker D2 Phaser.

## 6.4 Spectroscopy

### 6.4.1 UV-Vis-NIR absorption spectroscopy

Using this spectroscopic method, it is possible to measure the light absorption as a function of the incident light wavelength. A deuterium lamp is used for the ultraviolet (UV) light and a tungsten lamp is used for the visible and near-infrared (NIR) range. A collimated beam of monochromatic light passes through the sample and falls on the photodetector. The information about the gathered signal is then represented as the absorption or transmission spectrum. The measurement consists of the comparison

between the incident light intensity and the light passing through the sample (or reflects from it), i.e. $I_i/I_0$. The Lambert-Beer law applies for every wavelength:

$$\frac{I_i}{I_0} = (-\varepsilon x) \tag{6.1}$$

where $\varepsilon$ is the absorption or extinction coefficient and $x$ is the distance in the material that the light passed through.

The determination of the optical bandgap is based on the application of the empirical Kubelka-Munk equation, that originated from the work on the paint coatings of Paul Kubelka and Franz Munk[11]. Their original work focused on predicting the reflection of the infinite number of paint coating layers $R_\infty$, knowing their absorption and re-emission fractions, respectively $a_0$ and $r_0$, which in fact are absorption and reflection (back-scattering) coefficients.

$$R_\infty = 1 + \frac{a_0}{r_0} - \sqrt{\frac{a_0^2}{r_0^2} + 2\frac{a_0}{r_0}} \tag{6.2}$$

The ratio of absorption to reflection as a reflection function can be found from the Kubelka-Munk equation.

$$F(R_\infty) = \frac{a_0}{r_0} = \frac{(1-R_\infty)^2}{2R_\infty} \tag{6.3}$$

For the practical application for semiconductors, $(FR_\infty\ hv)^n$ is plotted against the incident light energy, where $n$ depends on the nature of the transition. Table 6.1 sums up the values of $n$. The root square of the linear part of the plot determines the optical bandgap of the semiconductor. The resulting plot is called a Tauc plot, after the Czech-American physicist Jan Tauc, who proposed this method during his work on amorphous germanium.

*Table 1. Exponential values in the Tauc-like plots.*

| n | Transition nature |
|---|---|
| **2** | Direct allowed |
| $\mathbf{\frac{2}{3}}$ | Direct forbidden |
| $\mathbf{\frac{1}{2}}$ | Indirect allowed |
| $\mathbf{\frac{1}{3}}$ | Indirect forbidden |

In this work, Shimadzu UV-3600 Plus UV-Vis-NIR Spectrophotometer was used.

### 6.4.2 Photoluminescence (PL) [12]

Photoluminescence spectroscopy helps to describe the electronic structure of the material. Photoluminescence occurs when the chromophore from the excited state returns to its ground state, which results in a photon emission with the energy equal to the difference between these states. This phenomenon can happen in a very different timescale. Depending on how much time passes from the light absorption to the emission, photoluminescence can be divided into fluorescence, with short times, typically around nanoseconds, while phosphorescence may take milliseconds to even hours.

The most common way to describe different processes that lead to photoluminescence is the use of the Jabłoński diagram. Professor Aleksander Jabłoński was a Polish scientist who, in spite of his great passion for violin, devoted his career to fundamental problems of theoretical and experimental fluorescence. A part of his diagram is depicted in Figure 6.6. The ground state is marked as $S_0$, while sequential excited singlet states are respectively $S_1$ and $S_2$. At every electronic state state, the chromophores can exist at a number of vibrational states, marked as 0, 1, 2 etc. The incident light is absorbed by the electron that changes its energy from the ground state to one of the excited states. With few exceptions the chromophores rapidly thermalize to the lowest excited state through internal conversion (dashed arrows). The chromophore spontaneously relaxes from the exited to one of the highest vibrational state of the ground state, then rapidly relaxes to the thermal equilibrium. During this process, it emits the photon with the energy equal to the difference between those states. The losses on the vibrational states are the reason why the emitted energy is almost always lower that the absorbed energy. The difference between these energies is called the Stokes shift. Even higher difference between the absorption and emission energy difference can be due to solvent effects, excited state reactions, complex formation and/or energy transfer.

In some cases, the excited chromophore undergoes the intercrossing system, reaching the triplet state $T_1$. The relaxation from the triplet to the ground state is called phosphorescence. This transition is forbidden due to parallel spins, therefore it takes place rarely and at longer timescales.

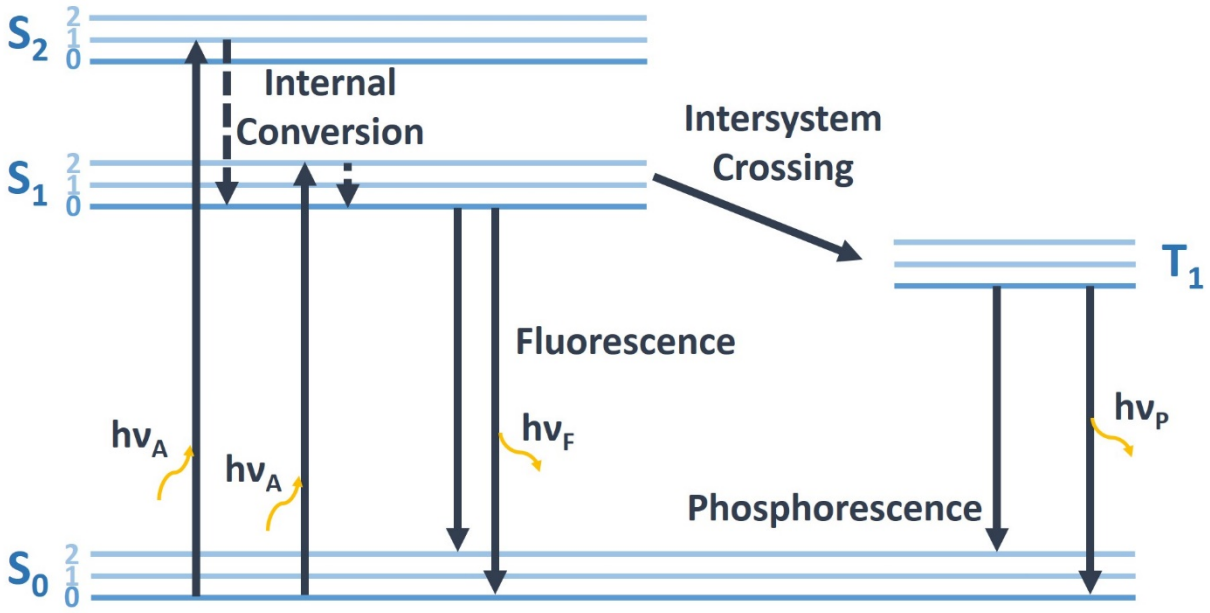


*Figure 6.6. Jabłoński diagram.*

Sometimes, the intensity of the emitted light can be decreased (quenched) and there is a number of mechanisms that can cause it:

- Dynamic (collisional) quenching – occurs through the energy transfer of the chromophore to a quencher that can after absorb it, resulting in a decrease of the total emitted light. Halogens and heavy atoms can act as quenchers due to spin-orbit coupling and intersystem crossing to the triplet state. The emission intensity decrease is described by the Stern-Volmer equation:

$$\frac{F_0}{F} = 1 + K[Q] = 1 + k_q \tau_0 [Q] \quad (6.4)$$

  where $K$ is the Stern-Volmer quenching constant, $k_q$ is the bimolecular quenching constant, $\tau_0$ is the unquenched lifetime, and $[Q]$ is the quencher concentration.

- Formation of non-fluorescent complexes with the quencher
- Attenuation of the incident light by the fluorophore itself or a foreign species

In this work, the photoluminescence spectra were recorder using the Photo Technology International setup, model: P21LRXS-LNN-NS-17.

### 6.4.3 Time of flight secondary ion mass spectroscopy (ToF-SIMS)

ToF-SIMS is a surface sensitive method for quantitative analysis of the sample composition. It uses a pulsed ion beam, typically Cs, Ga or Ar clusters for soft and/or organic matter to sputter the surface of the sample. Then, the secondary ions are analyzed by mass spectroscopy, either with magnet sector or time of flight. This technique allows to image the elemental map of the examined surface, as every pixel results in a specific spectrum. It is also possible to obtain depth-resolved composition profile by sputtering the sample from the surface. The measurement is performed in ultrahigh vacuum.

In this work, ToF SIMS profiles were performed with TOF.SIMS 5 ION-TOF and argon clusters were used for in-depth sputtering.

### 6.4.4 X-ray photoemission spectroscopy (XPS)

The basis of the Photoelectron Spectroscopy is the photoelectric effect, predicted by Albert Einstein in 1905 and rewarded by Nobel prize in 1912. An electron can be removed from atoms by photons whose energy exceeds the binding energy of this electron to the atom. The kinetic energy of the emitted photon is therefore a difference between its binding energy and the energy of the incident photon, decreased by the instrument's work function correction factor $\varphi$. This dependency is presented on the following equation:

$$E_{kinetic} = E_{binding} - E_{photon} - \varphi \tag{6.5}$$

In 1981 Dr. Kai Siegbahn received a Nobel prize for applying this effect for chemical analysis, therefore this technique was initially known as Electron Spectroscopy for Chemical Analysis (ESCA). Today known rather as X-ray Photoemission Spectroscopy, it is a non-destructive, surface sensitive method that provides information about:

- Elemental composition,
- Relative abundance (semi-quantitative), as elements ratios,
- Oxidation state, as the binding energy shifts slightly in different environments.

The spectra are presented as the number of photo-electrons as a function of binding energy. Each element has its well-known characteristic spectrum. Characteristic positions indicate the oxidation state of the element. The electrons in p, d and f orbitals show a double peak, indicating the spin-orbital splitting. The spin-orbit splitting ratio, observed as the peaks intensity is 1:2 for p orbitals, 2:3 for d orbitals and 1:4 for f orbitals.

In this work, XPS spectra were obtained using K-Alpha ThermoFisher Scientific spectrometer and the and in-depth profiles were performed by etching the surface with Ar ions.

### 6.4.5 Ultraviolet photoemission spectroscopy (UPS)

UPS also applies the photoelectric effect to analyze the electrons emitted from a sample's surface. The difference is that the UPS uses the ultraviolet light to extract electrons. As the energy used is lower, the emitted electrons do not come from the core electrons, but from the most outer valence band and Fermi level. The technique therefore allows, with great precision, to determine the Fermi level position and valence band maximum position in reference to the Fermi level. Together with the UV-vis absorption spectroscopy, it allows also to precisely place the conduction band bottom when the exciton binding energy is negligible.

In this work, UPS was obtained with the PHOIBOS 100 hemispherical energy analyzer, equipped with SPECS UVS 10/35 light source.

## 6.5 Electronic characterization

For the material analyzed within this work, the electronic measurements tell probably the most about their potential applications. The current-voltage characterization of the solar cell gives a direct insight into the efficiency, as well as indirect information about the losses that might occur as a result of the charge recombination at different places of the device. An especially useful technique in the loss analysis in solar cells is to measure their electroluminescence by applying the voltage and measuring the luminosity. External Quantum Efficiency measurement will be the last method used in this work for the analysis of the solar cell devices. Conductivity, Kelvin probe and Hall Effect measurements will serve for the doping characterization, revealing such parameters as doping type, charge carrier density and carrier mobility.

### 6.5.1 Solar cell current – voltage characterization

This simple method allows to scan rapidly the solar cell device and obtain a direct information about the efficiency. The method is essentially the superposition of the linear voltammetry in the dark and under the sun simulating illumination. The typical diode characteristic in the dark shifts upon illumination as a result of photo-current generation. In Chapter 1, it was briefly described how to calculate

the efficiency from the JV characteristics. In this chapter, we'll have a closer look on what other information can be withdrawn from this technique.

Short circuit current $I_{SC}$ is the current under illumination measured at 0 V. As its value depends on the cell area, typically it is represented as short circuit current density $J_{SC}$ (mA/cm$^2$). Except when the series resistance is very high (>10 Ωcm$^2$), the short circuit current is equal to the light generation current $I_L$. For the ideal cells, i.e. with the perfectly passivated surface and uniform charge generation, the $I_{SC}$ is a function of the generation rate $G$ and the electron and hole diffusion lengths, $L_e$ and $L_h$, respectively.

$$I_{SC} = qG(L_e + L_h) \tag{6.6}$$

Since $I_{SC}$ depends also on the light intensity and spectrum, a standardized condition is used for this measurement, with light spectrum AM 1.5 and intensity 100 mW/cm$^2$. Other material dependent parameters that impact the $I_{SC}$ are the optical properties, such as absorption, reflection and bandgap (the higher the bandgap, the lower the $I_{SC}$), and the minority carrier collection probability, which in turn depends on the minor carrier lifetime and the surface passivation.

The open circuit voltage is the voltage measured at zero current. It is strongly dependent on the absorber's bandgap and it increases as the bandgap increases. Perovskite solar cells are known for having one of the highest ratio of $V_{OC}$ to the bandgap, reaching over 0.75[13–15].

If plotting the solar cell power as a function of voltage, one can observe there is a clear maximum of the power, for certain V and I. This point is called a Maximum Power Point (MPP). The ratio of MPP and the product of $I_{SC} \cdot V_{OC}$ represents the "squareness" of the IV curve and is called a fill factor *FF* (Figure 6.7). The FF can be limited by high charge carrier recombination and internal resistance.

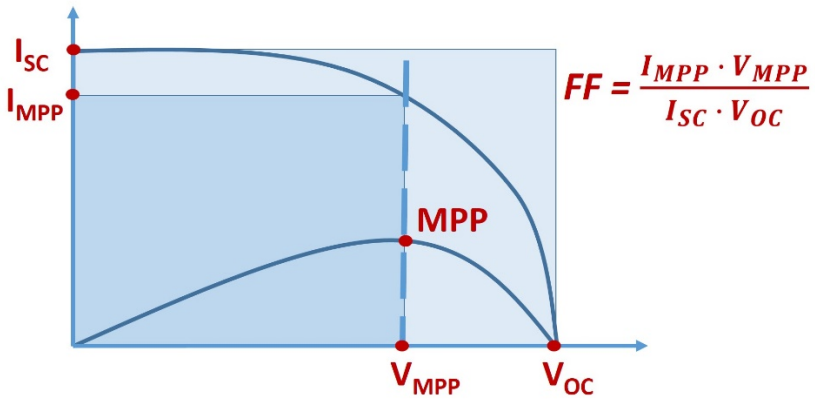


*Figure 6.7. The IV curve with the Maximum Power Point representation.*

Another parameter that can cause the *FF* decrease is the series resistance. Moreover, its extensively high values may also decrease the $I_{SC}$. There are three primary reasons for the series resistance to occur:

- movement of current through from the anode to the cathode,
- contact resistance on the interfaces,
- resistance of the metal contacts.

The intrinsic shunt resistance is due to minority charge carriers in the dark. For materials with a bandgap >1.5 eV, the intrinsic shunt resistance can be neglected. In perovskite solar cells, shunt resistance is most frequently due to the manufactural problems. It essentially creates an alternative path for the charge flux, causing the decrease of both voltage and current available for the energy generation. It can be an important cause of power loss.

In this work, the IV curves were registered using Keithley 2400 source meter unit (SMU) controlled by a custom-made LabView software. The solar cell devices were scanned from -1 V to 1.2 V with the rate of 10 mV/s. the HMI lamp was used with the AM 1.5G spectrum and light intensity 100 mW/cm$^2$.

### 6.5.2 External quantum efficiency (EQE)

External quantum efficiency is the ratio of the electrons collected to the incident photon flux at each wavelength. The ideal spectrum should have a square shape, i.e. ideally, every photon with the energy below the bandgap generates an electron and this electron is then collected from the electrodes. In practice, every solar cell is a subject to losses. Except for manufactural losses, the main reason of the deviation of the spectrum from the square is the low diffusion length, which means that the charge recombines before it reaches the contact electrode. Another common case is the optical loss, for example due to reflection of the incident light on the solar cell surface. High energy photons of the visible spectrum (blue light) are absorbed close to the surface of the absorber, therefore they will be affected by the surface and interface defects and recombine easily. It is the reason for low EQE for low wavelengths. The light from the UV region is absorbed by the bottom electrode, typically ITO or FTO.

### 6.5.3 Electroluminescence (EL)

The principle of the electroluminescence is the radiative recombination of charge, also known as spontaneous emission, after the charges have been injected by applying an electric field or current. As the

emission occurs in the red and near infrared for $CH_3NH_3PbI_3$, (≈780nm) silicon photodetector is sufficient to provide the information on the sample luminescence.

Measuring the electroluminescence of a solar cell is not the most common approach, however, it can be a mean of tracking non-radiative recombination in these devices that can lead to shunt losses[16,17]. They can be due to Auger recombination, band-tail recombination, electron-phonon coupling and defect-assisted recombination[18]. These losses can deteriorate the open circuit voltage ($V_{oc}$), short circuit current ($J_{sc}$) and fill factor (*FF*), resulting in a decrease of the overall solar cell performance. Excessive non-radiative recombination may additionally impact the solar cell's stability, which can impede their industrialization[19,20].

In this work, the emission energy was found using Ocean Optics High Resolution Spectrometer HR2000, while the luminescence was measured using Keithley multimeter connected to the photosensor amplifier Hamamtsu C9329. The calibration of the photodetector signal to luminescence was performed using a luminance meter Konica Minolta LS-100.

### 6.5.4 Conductivity

Conductivity is typically the first test to perform when investigating the doping of semiconductors. The conductivity increase can suggest that the Fermi level approached one of the edges of the bandgap, i.e. valence band maximum or conduction band minimum, therefore, it can be the first clue that the doping impacted the electrical properties of the semiconductor. Moreover, this method is inexpensive, fast and facile to perform.

In this work, the conductance was measured between two symmetric Ti/Au electrodes (10 and 50 nm, respectively) with the distance 200 µm between them, deposited on the glass substrates using the electron beam evaporator. The perovskite samples were spin coated on top of the electrodes, as shown in Figure 6.8.

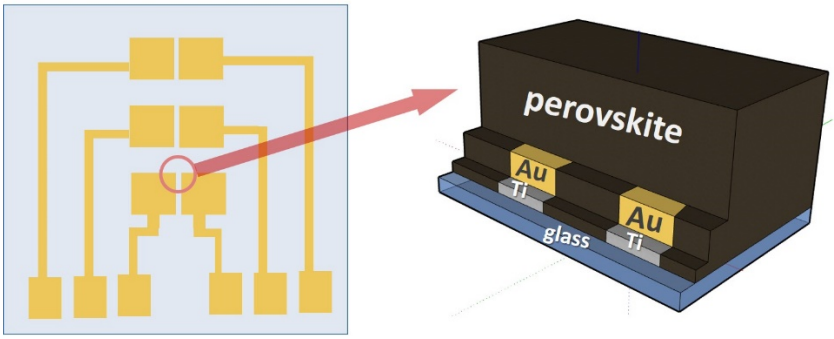


*Figure 6.8. The sample architecture for the conductivity measurement with the top view on the left and cross section on the right.*

In this work, conductivity was calculated from the IV curves that were registered using Keithley 4200 source meter unit (SMU). The samples were scanned from -1 V to 1 V with the rate of 5 mV/s. For the temperature dependent conductivity measurement, Biologic SP-200 was used and the temperature was controlled by cryostat Omron E5AN.

### 6.5.5 Kelvin probe (KP)

This surface sensitive method is used to measure the work function (*WF*) with respect to a reference sample, most often highly oriented pyrolytic graphite (HOPG) whose *WF* is assumed to be 4.6 eV, which is in the range of the theoretical values that are between 4.46 eV and 4.64 eV, depending on the number of layers[21]. The literature value spreads from 4.5 eV up to 5 eV[22,23,32,24–31]. The technique relies on measuring the contact potential difference $V_{CPD}$ between a gold probe and the sample. The result depends on the work function ($\varphi$) difference, as in the equation below.

$$qV_{CPD} = \varphi_1 - \varphi_2 \tag{6.7}$$

where $q$ is the elementary charge.

The electrons move from the material with lower WF to the higher *WF*, resulting in the current flow when the samples are in contact. This strategy would allow the *WF* difference measurement, but only once. Therefore, the probe and the sample are not in contact, but act like a capacitor. When the probe oscillates, the distance $d$ between the capacitor plates changes, so the capacitance $C$ also changes, like:

$$C = \varepsilon_0 \varepsilon_r \frac{A}{d} \tag{6.8}$$

where A is the area of the capacitor plates, $\varepsilon_0$ is the vacuum permittivity, $\varepsilon_r$ is the dielectric constant of the insulator. Since:

$$C = \frac{Q}{\Delta V_{CPD}} \tag{6.9}$$

and the total amount of charge $Q$ remains constant, the amplitude of $V_{CPD}$ determines the WF difference between the probe and the sample. The HOPG with the known WF sets the zero and the value measured for the examined samples is the WF difference between the HOPG reference and the sample.

### 6.5.6 Mott-Schottky

The Mott-Schottky plot shows the inverse of squared capacitance ($1/C^2$) versus the voltage V applied between the semiconductor and the electrolyte. When the voltage is applied, a depletion layer is formed at this interface and its thickness $w$ is known to be:

$$w = \sqrt{\frac{2\varepsilon_0 \varepsilon_r}{qN_D}(V + V_{bi})} \tag{6.101}$$

Where $N_D$ is the doping concentration and $V_{bi}$ is a build-in potential. The charge separation occurs also on the semiconductor/metal interface, forming a dielectric capacitor. As the capacitance for an electrode with area $A$ is

$$C = \frac{\partial Q}{\partial V} = N_D q A \frac{\partial w}{\partial V} \tag{6.11}$$

Combining Equations 6.10 and 6.11, one obtains

$$C = A \frac{\varepsilon_0 \varepsilon_r}{w} \tag{6.12}$$

Replacing $w$ with Equation 6.10:

$$C^{-2} = \frac{2}{q\varepsilon_0 \varepsilon_r N_D}(V + V_{bi}) \tag{6.13}$$

Therefore, by plotting $C^{-2}$ against the applied voltage, and determining the slope of the linear part of the plot, it is possible to obtain the doping concentration. The intercept of the linear part corresponds to the built in voltage.

This theory has recently started to be applied to the perovskite solar cells to investigate the device interfaces. However, the interpretation of the results is not trivial, mainly due to multiple or zero linear

regions on the plot. The application of this method to measure the perovskite doping concentration has not yet been explored. In this work, the Mott-Schottky analysis is used for the doped perovskite with a thin layer of $SnO_2$ deposited on the ITO to ensure an ohmic contact for electrons. For the top contact, an Au electrode is used to have a blocking contact for electrons. An ultrathin (<10 nm) layer of insulating poly(methyl methacrylate) (PMMA) is intercalated between the gold electrode and perovskite, in order to reduce leakage current. The scheme of the stacked sample is presented in the Figure 6.10.

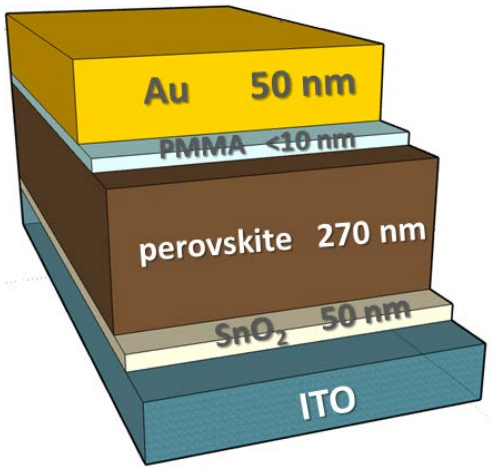


*Figure 6.9. Sample stack for the Mott-Schottky measurements.*

### 6.5.7 Hall Effect

The phenomenon discovered by Edwin Hall in 1879 was a part of his doctoral thesis at the University of Johns Hopkins in Baltimore, Maryland. In the article titled "On a New Action of the Magnet on Electric Currents"[33], he presented the results that for the first time experimentally proved the phenomenon we now know as the Hall effect. It relies on the Lorentz force ***F*** that causes the deflection of the charge *q* in a flat semiconductor (or conductor), when the electric current flows through it and it is in a trasverse magnetic field ***B***. The equation for the Lorentz Force is given below.

$$\boldsymbol{F} = q(\boldsymbol{E} + \boldsymbol{v} \times \boldsymbol{B}) \tag{6.14}$$

The scheme of this phenomenon is presented in Figure 6.9. The voltage between two sides of the bar is called the Hall voltage $V_H$ and it is proportional to the applied current and magnetic field and inversely proportional to the sample thickness *d*, according to the equation below.

$$V_H = \frac{HI\boldsymbol{B}}{d} \tag{6.15}$$

where $H$ is the Hall coefficient, defined as:

$$H = \frac{r}{qn_{Hall}} \tag{6.16}$$

with the scattering factor $r$ depending on the scattering mechanism[34]. From the sign and value of $H$, the semiconductor type and charge carrier density $n_{Hall}$ can be determined. From the charge carrier density and conductivity $\sigma$, the majority carrier mobility $\mu$ is calculated, as:

$$\mu_{n\ or\ p} = \pm\sigma H \tag{6.17}$$

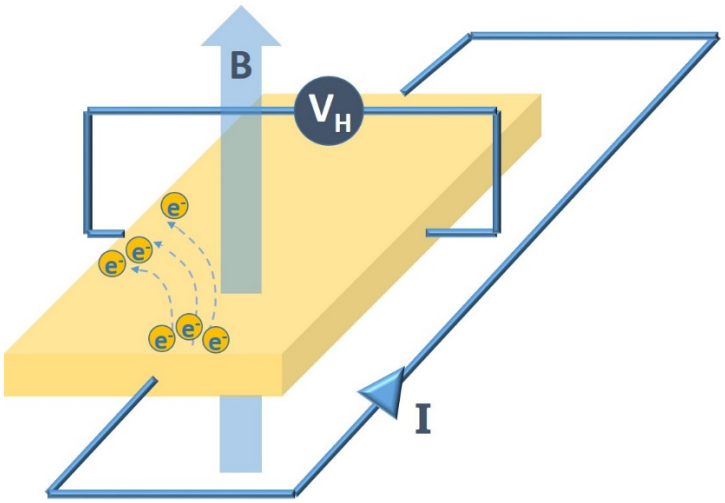


*Figure 6.10. Hall effect.*

While the Hall effect measurement can be quite reliable, it is not a simple method and it has some drawbacks with regard to perovskites in particular. Some of the main drawbacks are that ohmic contacts are required, which may be complicated mainly due to the fact that halides are known to react with common contact metals (Ag or Cu), creating an insulating layer of salt on the interface. Gold seems to be the best candidate, yet one must be cautious, as it was shown that there are shallow hole traps created on the interface of Au and MAPI, leading to the charge recombination and increased contact resistance[35]. The biggest problems in a standard Hall measurement, i.e. one with a static magnetic field, are low sensitivity and low signal-to-noise ratio, as well as a drifting background signal for samples with low mobility (≤ 1 $cm^2V^{-1}s^{-1}$) and high sheet resistance (≥10 $M\Omega sq^{-1}$) such as perovskites. A solution to these obstacles is to apply a sinusoidal magnetic field and a lock-in detection[36,37]. Nevertheless, the scattering

factor *r* must be assumed. It usually lies between 1 and 2 and it is commonly assumed that *r* = 1, which should limit the error to <30%, however it must be remembered that with doping the *r* can change.

**References**


[1] Q. Ma, S. Huang, X. Wen, M. A. Green, A. W. Y. Ho-Baillie, *Adv. Energy Mater.* **2016**, *6*, 2.

[2] S. Ulična, B. Dou, D. H. Kim, K. Zhu, J. M. Walls, J. W. Bowers, M. F. A. M. Van Hest, *ACS Appl. Energy Mater.* **2018**, *1*, 1853.

[3] Z. Li, P. Li, G. Chen, Y. Cheng, X. Pi, X. Yu, D. Yang, L. Han, Y. Zhang, Y. Song, *ACS Appl. Mater. Interfaces* **2020**, *12*, 39082.

[4] H. Ying, Y. Liu, Y. Dou, J. Zhang, Z. Wu, Q. Zhang, Y. B. Cheng, J. Zhong, *Front. Optoelectron.* **2020**, *13*, 272.

[5] A. Mei, X. Li, L. Liu, Z. Ku, T. Liu, Y. Rong, M. Xu, M. Hu, J. Chen, Y. Yang, M. Grätzel, H. Han, *Science (80-. ).* **2014**, *345*, 295.

[6] F. Fu, T. Feurer, T. Jäger, E. Avancini, B. Bissig, S. Yoon, S. Buecheler, A. N. Tiwari, *Nat. Commun.* **2015**, *6*, 1.

[7] S. A. Moyez, S. Roy, *Sol. Energy Mater. Sol. Cells* **2018**, *185*, 145.

[8] P. Zhao, B. J. Kim, X. Ren, D. G. Lee, G. J. Bang, J. B. Jeon, W. Bin Kim, H. S. Jung, *Adv. Mater.* **2018**, *30*, 1.

[9] M. Saliba, J. P. Correa-Baena, C. M. Wolff, M. Stolterfoht, N. Phung, S. Albrecht, D. Neher, A. Abate, *Chem. Mater.* **2018**, *30*, 4193.

[10] A. G. Emslie, F. T. Bonner, L. G. Peck, *J. Appl. Phys.* **1958**, *29*, 858.

[11] P. Kubelka, F. Munk, *Z. Tech. Phys* **1931**, *12*, 259.

[12] C. Albrecht, **2008**.

[13] E. H. Anaraki, A. Kermanpur, L. Steier, K. Domanski, T. Matsui, W. Tress, M. Saliba, A. Abate, M. Grätzel, A. Hagfeldt, J.-P. Correa-Baena, *Energy Environ. Sci.* **2016**, *9*, 3128.

[14] S. Gharibzadeh, B. Abdollahi Nejand, M. Jakoby, T. Abzieher, D. Hauschild, S. Moghadamzadeh, J.

A. Schwenzer, P. Brenner, R. Schmager, A. A. Haghighirad, others, *Adv. Energy Mater.* **2019**, *9*, 1803699.

[15] L. Gil-Escrig, C. Dreessen, F. Palazon, Z. Hawash, E. Moons, S. Albrecht, M. Sessolo, H. J. Bolink, *ACS Energy Lett.* **2021**, *6*, 827.

[16] G. J. A. H. Wetzelaer, M. Scheepers, A. M. Sempere, C. Momblona, J. Ávila, H. J. Bolink, *Adv. Mater.* **2015**, *27*, 1837.

[17] D. Luo, R. Su, W. Zhang, Q. Gong, R. Zhu, *Nat. Rev. Mater.* **2020**, *5*, 44.

[18] T. Hwang, B. Lee, J. Kim, S. Lee, B. Gil, A. J. Yun, B. Park, *Adv. Mater.* **2018**, *30*, 1.

[19] W. Xu, Y. Gao, W. Ming, F. He, J. Li, X. H. Zhu, F. Kang, J. Li, G. Wei, *Adv. Mater.* **2020**, *32*, 1.

[20] J. Zhang, H. Yu, *J. Mater. Chem. A* **2021**, *9*, 4138.

[21] S. J. Sque, R. Jones, P. R. Briddon, *Phys. status solidi* **2007**, *204*, 3078.

[22] W. Melitz, J. Shen, S. Lee, J. S. Lee, A. C. Kummel, R. Droopad, E. T. Yu, *J. Appl. Phys.* **2010**, *108*, 23711.

[23] H. K. Jeong, C. Yang, B. S. Kim, K. Kim, *EPL (Europhysics Lett.* **2010**, *92*, 37005.

[24] T. Glatzel, M. Rusu, S. Sadewasser, M. C. Lux-Steiner, *Nanotechnology* **2008**, *19*, 145705.

[25] W. N. Hansen, G. J. Hansen, *Surf. Sci.* **2001**, *481*, 172.

[26] A. Liscio, V. Palermo, K. Müllen, P. Samorì, *J. Phys. Chem. C* **2008**, *112*, 17368.

[27] C. Sommerhalter, T. W. Matthes, T. Glatzel, A. Jäger-Waldau, M. C. Lux-Steiner, *Appl. Phys. Lett.* **1999**, *75*, 286.

[28] C. H. Kim, C. D. Bae, K. H. Ryu, B. K. Lee, H. J. Shin, in *Solid State Phenom.*, **2007**, pp. 607–610.

[29] J. S. Kim, J. S. Choi, J. H. Lee, S. H. Kim, S. H. Jeon, I. R. Hwang, B. H. Park, T. J. Choi, S. H. Shin, J. C. Lee, others, *J. Korean Phys. Soc.* **2005**, *47*, 243.

[30] V. Palermo, M. Palma, Ž. Tomović, M. D. Watson, R. Friedlein, K. Müllen, P. Samor\`\i, *ChemPhysChem* **2005**, *6*, 2371.

[31] P. G. Schroeder, M. W. Nelson, B. A. Parkinson, R. Schlaf, *Surf. Sci.* **2000**, *459*, 349.

[32] B. Reihl, J. K. Gimzewski, J. M. Nicholls, E. Tosatti, *Phys. Rev. B* **1986**, *33*, 5770.

[33] E. H. Hall, others, *Am. J. Math.* **1879**, *2*, 287.

[34] D. K. Schroder, *Semiconductor Material and Device Characterization*, John Wiley \& Sons, **2015**.

[35] Y. F. Chen, Y. T. Tsai, L. Hirsch, D. M. Bassani, *J. Am. Chem. Soc.* **2017**, *139*, 16359.

[36] Y. F. Chen, Y. T. Tsai, D. M. Bassani, R. Clerc, D. Forgács, H. J. Bolink, M. Wussler, W. Jaegermann, G. Wantz, L. Hirsch, *J. Mater. Chem. A* **2016**, *4*, 17529.

[37] O. Gunawan, S. R. Pae, D. M. Bishop, Y. Virgus, J. H. Noh, N. J. Jeon, Y. S. Lee, X. Shao, T. Todorov, D. B. Mitzi, **2019**, *575*.